Springer Theses
Recognizing Outstanding Ph.D. Research

Mahmut Deniz Yilmaz

Orthogonal Supramolecular Interaction Motifs for Functional Monolayer Architectures

Springer

Springer Theses

Recognizing Outstanding Ph.D. Research

For further volumes:
http://www.springer.com/series/8790

Aims and Scope

The series "Springer Theses" brings together a selection of the very best Ph.D. theses from around the world and across the physical sciences. Nominated and endorsed by two recognized specialists, each published volume has been selected for its scientific excellence and the high impact of its contents for the pertinent field of research. For greater accessibility to non-specialists, the published versions include an extended introduction, as well as a foreword by the student's supervisor explaining the special relevance of the work for the field. As a whole, the series will provide a valuable resource both for newcomers to the research fields described, and for other scientists seeking detailed background information on special questions. Finally, it provides an accredited documentation of the valuable contributions made by today's younger generation of scientists.

Theses are accepted into the series by invited nomination only and must fulfill all of the following criteria

- They must be written in good English.
- The topic should fall within the confines of Chemistry, Physics, Earth Sciences and related interdisciplinary fields such as Materials, Nanoscience, Chemical Engineering, Complex Systems and Biophysics.
- The work reported in the thesis must represent a significant scientific advance.
- If the thesis includes previously published material, permission to reproduce this must be gained from the respective copyright holder.
- They must have been examined and passed during the 12 months prior to nomination.
- Each thesis should include a foreword by the supervisor outlining the significance of its content.
- The theses should have a clearly defined structure including an introduction accessible to scientists not expert in that particular field.

Mahmut Deniz Yilmaz

Orthogonal Supramolecular Interaction Motifs for Functional Monolayer Architectures

Doctoral Thesis accepted by
the University of Twente, The Netherlands

Springer

Author
Dr. Mahmut Deniz Yilmaz
Stoddart Mechanostereochemistry Group
Department of Chemistry
Northwestern University
Evanston, IL
USA

Supervisor
Prof. Dr. Jurriaan Huskens
Molecular Nanofabrication Group
MESA+ Institute for Nanotechnology
University of Twente
Enschede
The Netherlands

ISSN 2190-5053 ISSN 2190-5061 (electronic)
ISBN 978-3-642-30256-5 ISBN 978-3-642-30257-2 (eBook)
DOI 10.1007/978-3-642-30257-2
Springer Heidelberg New York Dordrecht London

Library of Congress Control Number: 2012938867

Printed on acid-free paper

Springer is part of Springer Science+Business Media (www.springer.com)

Parts of this thesis have been published in the following journal articles:

1. T. Gang, **M. Deniz Yilmaz**, D. Ataç, S. K. Bose, E. Strambini, A. H. Velders, M. P. de Jong, J. Huskens, W. G. van der Wiel, *Nature Nanotechnology*, DOI: 10.1038/NNANO.2012.1. "Tunable Molecular Spin Doping of a Metal"

2. B. Eker, **M. Deniz Yilmaz**, S. Schlautmann, J. G. E. Gardeniers, J. Huskens, *International Journal of Molecular Science* **2011**, 12 (11), 7335–7351. "A Supramolecular Sensing Platform for Phosphate Anions and an Anthrax Biomarker in a Microfluidic Device"

3. W. P. Voorthuijzen, **M. Deniz Yilmaz**, W. Naber, J. Huskens, Wilfred Van der Wiel, *Advanced Materials*, **2011**, 23 (11), 1346–1350. "Local doping of silicon using nanoimprint lithography and molecular monolayers"

4. W. P. Voorthuijzen, **M. Deniz Yilmaz**, A. Gomez-Casado, P. Jonkheijm, W. G. van der Wiel, J. Huskens, *Langmuir*, **2010**, 26 (17), 14210–14215. "Direct patterning of covalent organic monolayers on silicon using nanoimprint lithography"

5. **M. Deniz Yilmaz**, S. H. Hsu, D. N. Reinhoudt, A. H. Velders, J. Huskens, *Angewandte Chemie International Edition*, **2010**, 49, 5938–5941. "Ratiometric fluorescent detection of an anthrax biomarker at molecular printboards"

6. S. H. Hsu, **M. Deniz Yilmaz**, C. Blum, V. Subramaniam, D. N. Reinhoudt, A. H. Velders, J. Huskens, Journal of the American Chemical Society, **2009**, 131, 12567–12569. "Expression of Sensitized Eu^{3+} Luminescence at a Multivalent Interface"

To my wife, grandma, parents and all my family

Supervisor's Foreword

Multivalency is the phenomenon that describes the interaction between multivalent receptors and multivalent ligands. It is well known to play a pivotal role in biochemistry, particularly in protein–carbohydrate interactions, both in solution and at interfaces (e.g. for the infection of cells by the attachment of viruses or bacteria to cell membranes). In particular in the latter case, multivalency is often poorly understood in a quantitative sense.

Supramolecular host–guest chemistry has been well established in solution, but its use at interfaces remains limited to for example sensor development for specific guest compounds. In order to *build* assemblies at surfaces through supramolecular interactions for nanotechnological applications, other demands have to be met, such as larger thermodynamic and kinetic stabilities of the assemblies. For many supramolecular motifs, this inevitably leads to the use of *multivalent* interactions.

The main line of this thesis deals with *heterotropic* multivalency, which is the use of *multiple* interaction motifs. After a thorough introduction (Chap. 2) into orthogonal interactions to create monolayer achitectures, the first three chapters deal with the bottom-up development of a platform based on such orthogonal host–guest and metal–ligand coordination interactions (Chap. 3) and its application in a novel, sensitive and exciting anthrax sensor platform (Chap. 4) and a microfluidic sensor for biological anions (Chap. 5).

Chapters 6 and 7 deal with other forms of molecular monolayers in the development of nanoelectronic and spintronic devices. This thesis provides a colorful illustration of the current powers of nanochemistry, and in particular of monolayers in the development of functional interfaces for biosensing and nanotechnology. The results described in this thesis have provided a boost to ongoing and new projects within the group and MESA+ on nanoelectronics, surface gradients and electrochemical and fluorometric biosensing. A true piece of exciting science at the forefront of nanochemistry! Enjoy!

Jurriaan Huskens

Acknowledgments

Finally I finished my PhD thesis, and I would like to thank many people for their help and support during these four years. I am very proud that now it is time to write the most important part of the thesis. It is not easy to summarize my all acknowledgments in a few words, but just I can say that I am really grateful to all people I met during my PhD.

My first acknowledgment goes to my promoter and supervisor, Jurriaan Huskens. Actually I don't know where I will start and I will never find enough words to say. I thank you for accepting me as a PhD student and to be part of this group. I will never forget our biweekly meetings, where I have learnt so much from you. During these meetings you always gave me lot of confidence, encouragement and freedom mostly when I lost my way. You were always patient to listen to me when I brought completely different ideas while proceeding a certain project. I want to thank you for all your help, ideas, guidance, and patience throughout this whole period. Thank you very much for everything you did for me.

I would like to thank to Aldrik and Wilfred for the meetings we had in the last 3 years of my PhD and for the scientific contribution. They were very useful with a lot of nice ideas. I really enjoyed and learned so many things during our meetings.

During these four years I had the chance to collaborate with many people, the results of which are presented in this thesis. I owe my appreciation to Shu-Han Hsu for all her help. You always had time for me to help me to prepare the patterned samples and for discussions on results. We had many nice discussions which were very essential to obtain results presented in Chaps. 3 and 4. I would like to thank Dr. Bilge Eker for introducing me to the world of microchips and for her participation to Chap. 5. I really learnt a lot from you. I would like to thank Pim for his contribution to Chap. 6. You were my first master student and I couldn't support you much during your studies due to my lack of knowledge about nanoimprint lithography. At the end, when we looked through the results, we managed this project successfully. My appreciation also goes to Wouter Naber and Peter Tijssen for their help for Chap. 7. It was a long project and still continues with a new PhD student, Derya. I hope you will complete this project during your PhD. I would like

thank all of you again, it was a pleasure to work with you and without your help I could not have completed my PhD. My special thanks go to Mudassir Iqbal. Dear Mudooo, thank you very much for all your friendship and help during these years. I will never forget our discussions the topic could be whatever. I appreciate your friendship. I would like to thank Marcel and Richard for their technical support. The secretaries of MnF/SMCT/BNT, Izabel and Nicole, are also thanked for taking care of all administrative works. I thank you Melissa for going so carefully through my concept thesis. I also spent some time doing EPR measurements in Barcelona. Dear Veronica, thanks for your help and contribution on EPR experiments. I really enjoyed my short trip to Barcelona. I would like to thank Tom. Dear Tom, thank you very much for your great effort to translate my thesis summary from English to Dutch. I appreciate your kindness. I would like to thank Janet Acikgoz. Dear Janet, thanks for encouraging me in the first year of PhD. Whenever I was upset, you tried to help me recover again and again.

During my PhD, I have had opportunity to meet a lot of fantastic people, Xing Yi, Duan, Henk, Sachin, Veera, Elisabetta, Riccardo, Francesca, Ignacio, Andras, Huaping, Yiping, Srinidhi, Tian, Kim, Roberto, Albert, Arancha, Carmen, Sven, Carlo, Jordi, Lanti, Jealemy, Pieter, Alberto, Melanie, Raluca, Vijay, Chien-Ching Wu, Dae June, Oktay, Erhan, Serkan, Mine, Anna, Rajesh, Nicolai, and many more. All the people I mentioned here have contributed to make the time I spent in Enschede an unforgettable time of my life. But most importantly, I owe my deepest gratitude to my family; my parents, my two brothers for all the support they give me. Canim annem, babam, kardeslerim. Sizlerin sevgi ve anlayisiyla ben bu doktorayi bitiriyorum. Bana desteklerinizi hicbir zaman eksik etmediniz. Sizleri cok ama cok seviyorum.

Lastly, this thesis is dedicated to the owner of my heart, Burcu, I wouldn't have completed this thesis without you. You are my soul, my lover, and my best friend. My heart is filled with your love. We have overcome all bad moments, and welcome every good moments hand-in-hand in our life. We are growing and walking together to our future. I love you! Seni cok seviyorum askim herseyim.

This research has been financially supported by the Council for Chemical Sciences of the Netherlands Organization for Scientific Research (NWO-CW), (grant 700.55.029 to Jurriaan Huskens). The research was carried out within the Molecular Nanofabrication (MnF) group, MESA$^+$ Institute for Nanotechnology, University of Twente, The Netherlands.

Enschede, The Netherlands, May 2011 Mahmut Deniz Yilmaz

Contents

Summary

The research described in this thesis is focused on the combination of orthogonal supramolecular interactions for functional monolayer architectures on surfaces. The term "orthogonal supramolecular interactions" refers to non-covalent interactions that do not influence each other's assembly properties when applied in the same system. Orthogonal self-assembly allows extended control over the self-assembly process and promotes new materials properties. Individual noncovalent interactions (e.g. hydrogen bonding, metal coordination, electrostatic or host–guest interactions) have been employed in many studies. However, the combination of different supramolecular interactions in the same system can improve the properties of the materials. The research described in this thesis aims to develop hybrid, multifunctional monolayers by using orthogonal supramolecular interactions, enabling the control over the monolayer composition and functionality. Orthogonal host–guest and lanthanide–ligand coordination interaction motifs have been employed to create supramolecular luminescent monolayers in the first part of the thesis (Chaps. 3–5). The second part of the thesis (Chaps. 6 and 7) deals with the fabrication of functional monolayers on silicon and gold substrates for applications in electronics.

A general introduction has been given in Chap. 1 which addresses the importance of non-covalent interactions for the fabrication of functional surfaces.

A literature overview has been given in Chap. 2 on the use of supramolecular interactions for the generation of hybrid assemblies and materials. Supramolecular chemistry and molecular self-assembly including hydrogen bonding, metal coordination, electrostatic and host–guest interactions to direct the immobilization of functional systems on surfaces are discussed in detail. Special attention is given to the combination of different supramolecular interaction types for the generation of functional monolayer architectures.

Chapter 3 describes the assembly of a guest-functionalized naphthalene antenna and a Eu^{3+}-complexed EDTA-based ligand molecule onto a receptor surface by combining the orthogonal host–guest and metal–ligand coordination motifs. Local fluorescence emission spectra of the immobilized complex demonstrated the

occurrence of sensitized Eu^{3+} luminescence. The energy transfer efficiency between the antenna and the Eu^{3+} complex was determined by time-resolved fluorescence measurements and found to be about 35 %. The stoichiometry of complexation between antenna and Eu^{3+} complex was investigated by the very first Job plot analysis at a surface and found to be 1:1 by examining the sensitized luminescence of the surface-immobilized complex at different antenna–Eu^{3+} complex ratios.

In Chap. 4, the same lanthanide complex system was used for the ratiometric detection of dipicolinic acid (DPA), which is a unique biomarker for anthrax bacterial spores, with high sensitivity and selectivity on a supramolecular monolayer surface. The fluorescence intensity ratio of the lanthanide-based surface receptor system upon addition of different concentrations of DPA showed that the recovery of the naphthalene emission is practically complete in the presence of only 200 nM DPA. The intensity ratio of the Eu^{3+}-based sensing platform as a function of time upon addition of 200 nM DPA indicated that the sensing response is complete within 10 min. The detection limit of the system was also investigated and found to be about 25 nM of DPA. To exhibit the selectivity of the supramolecular sensing surface, fluorescence changes upon addition of different competitive aromatic ligands were investigated. The negligible changes demonstrated the excellent selectivity of the system for DPA.

Chapter 5 has introduced a supramolecular sensing platform on a microchip surface that allows the detection of biologically relevant phosphate anions and aromatic carboxylic acids in a high-throughput format. The Eu^{3+}-based supramolecular sensing system was implemented on the surface of a multichannel chip. The sensing layer on the microchip surface is an ensemble of the antenna and Eu^{3+}-complexed ligand. When an anionic guest was added to the ensemble, it displaced the antenna, and triggered a fluorescence decrease upon binding to the Eu^{3+} center. ATP and pyrophosphate among various phosphate anions, and the anthrax biomarker DPA among various aromatic carboxylic acids showed a strong response to the sensitized Eu^{3+} luminescence-based microchip surface.

Chapter 6 describes the local doping of oxide-free silicon using nanoimprint lithography (NIL) and molecular monolayers. Covalently bonded Si–C monolayer patterns with feature sizes ranging from 100 nm to 100 μm were created via a local hydrosilylation reaction on NIL-patterned resist areas. These patterns were characterized by XPS, AFM, and TOF-SIMS measurements. Monolayer patterns with 100 μm features were fabricated to enable pattern characterization by XPS. Elemental mapping spectra showed that the patterned monolayers were created by hydrosilylation. To fabricate the nanoscale features, a nickel-plated mold containing a square array of 150 nm pillars was used and the resulting structures were visualized by AFM. Results showed that clearly defined patterns were obtained. Using a phosphorus-containing organic precursor, highly-doped and patterned (μm scale) regions in nearly intrinsic silicon were successfully fabricated. These patterned regions were characterized by TOF-SIMS for imaging and depth profiling. The dopant surface dose on a doped area measured $(2.3 \pm 0.1) \times 10^{19}$ P atoms.cm^{-3} corresponding to an areal dose on a doped area of $5.6 \pm 0.1 \times 10^{13}$ P

atoms.cm^{-2}. Electrical characterizations were performed by Hall and sheet-resistance measurements. An average sheet carrier density was determined and found to be $1.9 \pm 0.1 \times 10^{13}$ cm^{-2} at 300 K and $9.4 \pm 0.1 \times 10^{12}$ cm^{-2} at 150 K in case of patterned samples. More importantly, the resistance measured on line-patterned substrates along the line direction was significantly lower than when measured perpendicular to the pattern direction.

Chapter 7 describes the fabrication of monolayers of organic molecules with unpaired spins on a thin gold film. Nitroxyl 2,2,6,6-tetramethylpiperidin-1-oxyl (TEMPO) radicals and terpyridinyl-cobalt complexes were used in this study. The existence of unpaired spins in self-assembled monolayers was investigated by XPS, and CV measurements. XPS measurements identified the cobalt ions in the monolayer. The two main peaks occurred at 781.3 and 796.3 eV, corresponding to the Co2p3/2 and Co2p1/2 states, respectively. The CVs of cobalt complexes on gold substrate showed a typical reversible electrochemical reaction, with an oxidation peak at 0.22 V corresponding to the $Co^{3+/2+}$ process. The CVs of TEMPO radicals exhibited a symmetrical reversible one electron redox process. The redox potentials were +0.72 V and +0.68 V versus Ag/AgCl, respectively. Electrical transport measurements of terpyridinyl-cobalt complexes showed an increase of the sheet resistance of gold layers covered with a SAM of magnetic and non-magnetic molecules when the temperature was decreased. Electrical transport measurements of TEMPO radicals were carried out and no significant difference in resistance between the bare gold and the gold covered with the monolayer was observed.

The results presented in this thesis illustrate the power of relatively weak supramolecular interactions to direct the immobilization of functional systems on surfaces. The work on the combination of host–guest and lanthanide–ligand coordination interaction motifs on surfaces demonstrates that hybrid, multifunctional supramolecular monolayers can be fabricated by integrating different non-covalent interactions in the same system. Hence, the combination of different supramolecular interactions opens up new avenues for the fabrication of complex hybrid organic-inorganic materials and stimuli-responsive surfaces.

Chapter 1
General Introduction

Supramolecular chemistry and self-assembly processes have evolved to be one of the most important fields in modern chemistry of the last two decades [1]. Molecular recognition and self-assembly represent the basic concept of supramolecular chemistry and involved noncovalent interactions [2]. Noncovalent interactions (e.g. hydrogen bonding, metal–ligand coordination, electrostatic, and host–guest interactions) are usually weaker than covalent bonds and they are reversible. The use of supramolecular interactions to direct the spontaneous assembly of molecules is of utmost importance due to their high specificity, controlled affinity, and reversibility [3]. These specific and highly controllable interactions can be manipulated independently and simultaneously, providing orthogonal self-assembly which describes the assembly of components with multiple (i.e. more than one) interaction motifs that do not influence each other's assembly properties, applied in the same system [4].

Today a variety of orthogonal supramolecular systems are known in solution [5]. Although these weak interactions were employed individually to build supramolecular architectures on surfaces, few attempts have been reported for the generation of hybrid, multifunctional materials based on orthogonal interactions. The research described in this thesis is focused on the combination of these interactions (orthogonal supramolecular interactions) for functional monolayer architectures on surfaces.

In Chap. 2 of this thesis, a literature overview is given regarding the use of individual supramolecular interaction motifs (hydrogen bonding, metal coordination, electrostatic, and host–guest interactions) for assembly on surfaces as well as recent studies describing the combination of these interactions.

The first part of the thesis (Chaps. 3, 4, and 5) deals with the multivalent binding of supramolecular complexes at molecular printboards which are monolayers of cyclodextrin (CD) on a surface. Chapter 3 describes the combination of orthogonal host–guest and lanthanide-ligand coordination interaction motifs. Antenna-sensitized Eu^{3+} luminescence based on host–guest interactions on the

M. D. Yilmaz, *Orthogonal Supramolecular Interaction Motifs for Functional Monolayer Architectures*, Springer Theses, DOI: 10.1007/978-3-642-30257-2_1,

molecular printboard is employed for qualitative and quantitative studies of the complexation of different building blocks.

In Chap. 4, the same lanthanide complex system is used for the ratiometric detection of dipicolinic acid (DPA), which is a unique biomarker for anthrax bacterial spores, on a receptor surface. The system constitutes the first lanthanide-based surface receptor system for the detection of DPA.

Chapter 5 continues the study described in Chaps. 3 and 4. By using the same lanthanide complex system, a supramolecular high-throughput platform based on self-assembled monolayers implemented in a microfluidic device is described resulting in a general detection method for biologically relevant phosphate anions and DPA.

The second part of the thesis (Chaps. 6 and 7) concerns the use of the functional monolayers for nanoelectronics. Chapter 6 introduces the local doping of oxide-free silicon using nanoimprint lithography (NIL) and molecular monolayers. Covalently bonded Si–C monolayer patterns with feature sizes ranging from 100 nm to 100 μm are created via a local hydrosilylation reaction on NIL-patterned resist areas. This novel patterning strategy is successfully applied for introducing dopant atoms in the underlying silicon substrate using a phosphorus-containing molecular precursor on oxide-free silicon.

Chapter 7 describes the fabrication of monolayers of organic molecules with unpaired spins on a thin gold film. The existence of unpaired spins in self-assembled monolayers is demonstrated. Electrical transport measurements are performed and an increase of the gold film sheet resistance for temperatures below ~ 20 K for some examples is observed.

References

1. G.M. Whitesides, B. Grzybowski, Science **295**, 2418–2421 (2002)
2. J.M. Lehn, *Supramolecular Chemistry, Concepts and Perspectives* (VCH, Weinheim, 1995)
3. J.M. Lehn, Rep. Prog. Phys. **67**, 249–265 (2004)
4. P.E. Laibinis, J.J. Hickman, M.S. Wrighton, G.M. Whitesides, Science **245**, 845–847 (1989)
5. H. Hofmeier, U.S. Schubert, Chem. Commun. 2423–2432 (2005)

Chapter 2
Orthogonal Supramolecular Interaction Motifs for Functional Monolayer Architectures

2.1 Introduction

Supramolecular chemistry refers to the area of the chemistry of molecular assemblies and of the intermolecular bond (chemistry beyond the molecule) and focuses on the development of self-assembly pathways toward large moleculer systems or molecular arrays [1] Molecular self-assembly has been demonstrated by supramolecular chemistry and can be defined as the spontaneous assembly of the molecules under equilibrium conditions into stable, structurally well-defined aggregates through noncovalent interactions (e.g. hydrogen bonding, metal coordination, electrostatic or host–guest interactions) which are usually weaker than covalent bonds. Moreover, supramolecular interactions are reversible, whereas covalent bonds are usually irreversible. The use of supramolecular interactions to direct the spontaneous assembly of molecules is of utmost importance owing to their high specificity, controlled affinity, and reversibility. These specific and highly controllable interactions can be manipulated independently and simultaneously, providing orthogonal self-assembly which describes the assembly of components with multiple (i.e. more than one) interaction motifs that do not influence each other's assembly properties, applied in the same system [2–6].

Self-assembled monolayers (SAMs) are ordered molecular assemblies formed by the adsorption of an adsorbate onto a solid surface. SAMs provide a convenient way to produce surfaces with specific chemical functionalities. Regarding the concept of controlled positioning of molecules on a surface, binding stoichiometry, binding strength, binding dynamics, packing density and order, and reversibility serve as crucial tuning parameters. Covalent immobilization of molecules does not offer convenient versatility and flexibility over most of these parameters. Supramolecular interactions afford a solution to the control of these criteria. Hence, the orthogonal self-assembly concept, integrated with various surface patterning methods such as soft-lithography, provides rapid and site-selective adsorption of

M. D. Yilmaz, *Orthogonal Supramolecular Interaction Motifs for Functional Monolayer Architectures*, Springer Theses, DOI: 10.1007/978-3-642-30257-2_2,

molecules and micrometer scale objects at predefined regions with high specificity and selectivity for the fabrication of complex hybride organic–inorganic materials.

Comprehensive reviews exist on orthogonal supramolecular interactions in solution [7, 8]. Objective of this chapter is to give an overview of the current understanding of orthogonal supramolecular interactions and its potential as a self-assembly tool on solid surfaces. For this reason, the focus will be on the individual supramolecular interaction motifs (hydrogen bonding, metal coordination, electrostatic and host–guest interactions) as well as recent advances for the combination of these orthogonal interactions for functional monolayer architectures on surfaces.

2.2 Hydrogen Bonding Directed Assembly on Surfaces

Self-assembly through multiple hydrogen bonding interactions has been widely used to create functional monolayers and new materials on surfaces. Multiple hydrogen bonding is of major importance in order to the enhanced stability of systems and allows assembly at near-equilibrium conditions, which facilitates control over the thermodynamic parameters of the assembly.

2.2.1 Assembly of Molecules on SAMs

Rotello and coworkers have developed a method to manipulate conductance using hydrogen bonding interactions at a self-assembled monolayer surface (Fig. 2.1) [9]. A binder molecule, diacyl 2, 6-diaminopyridine decanethiolate, was inserted into a background monolayer of decanethiolate on gold using replacement lithography. Electroactive functionalization of the monolayer was then achieved through binding of the complementary ferrocene-terminated uracil to the binder molecule. The ferrocene functionality can be replaced by dodecyl uracil for erasing the conductance. Current–voltage properties of the patterned region were monitored by using an STM tip. Noncovalent self-assembly provides a potential method to install and subsequently remove electroactive functionality.

Rotello and coworkers used three-point hydrogen bonding interactions between modified SAMs and complementary functionalized mono- and di- block copolymers to direct the adsorption process onto surfaces [10]. The thymine-diamidopyridine (Thy-DAP) hydrogen bonding motif provided a highly selective adsorption of the DAP- containing mono- and di- block copolymers onto the Thy-decorated gold surface under controlled deposition conditions (Fig. 2.2).

The group of Cooke demonstrated that phenanthrenequinone binds strongly to ureas and thioureas by forming two hydrogen bonds which can be modulated by altering the redox state of the quinone [11]. A SAM of a disulfide phenanthrenequinone binds phenyl urea-terminated PPI dendrimers by forming multiple

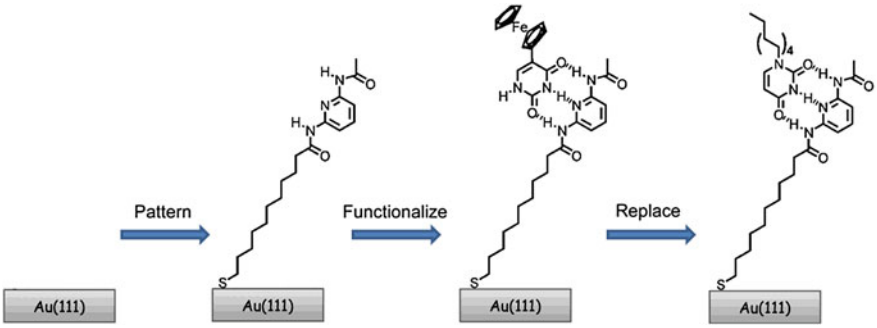

Fig. 2.1 Patterning, functionalization, and erasing at the surface of assembled monolayer. Adapted with permission from Ref. [9]. Copyright 2002 American Chemical Society

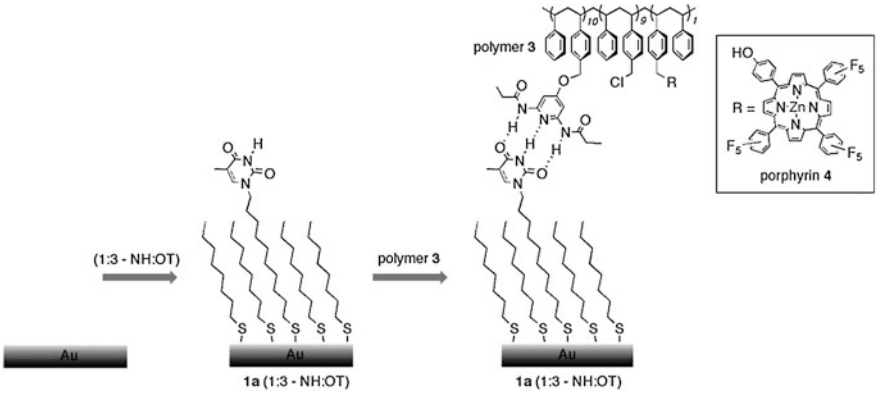

Fig. 2.2 Polymers tethered to surfaces using hydrogen bonding interactions. Adapted with permission from Ref. [10]. Copyright 2003 American Chemical Society

interactions. Upon oxidation, the dendrimers bind to the surface 2000-fold stronger while for a monovalent model compound a smaller increase of binding strength was observed. Myles and coworkers have described the immobilization of barbituric acid derivatives on mixed monolayers of alkanethiols and bis(2,6-diaminopyridine) amide of isophthalic acid-functionalized dedecanethiol on gold films [12]. The immobilization of barbiturate derivatives to the receptor-functionalized SAM involved the use of multiple hydrogen bonds to achieve a stable assembly on the surface (Fig. 2.3).

Reinhoudt et al. have reported synthetic hydrogen-bonded assemblies on gold surfaces [13]. The spontaneous assembly process was performed by incorporating the thioether-functionalized calix[4]arene dimelamines into a thiolate SAM. Subsequently, the monolayers containing one of the building blocks were immersed in a solution of the already formed assemblies, resulting in stable hydrogen-bonded assemblies at the surface (Fig. 2.4).

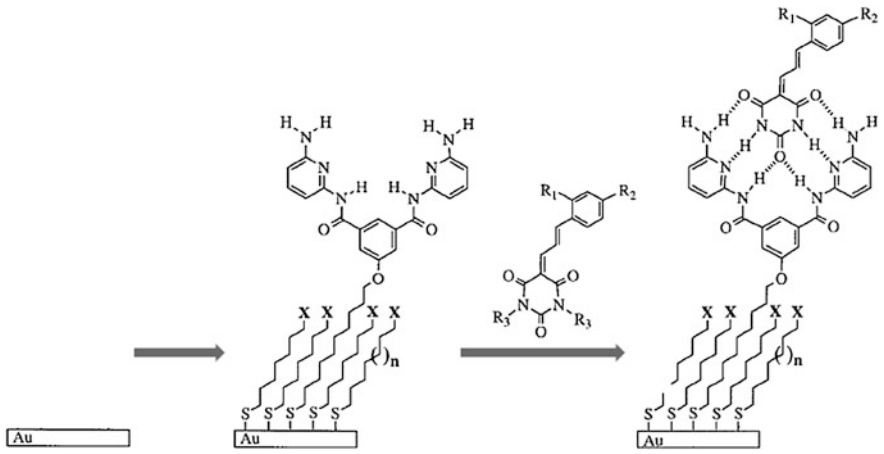

Fig. 2.3 Assembly between barbituric acid derivatives and the bis(2, 6-diaminopyridine) amide of isophthalic acid on a gold film. Adapted with permission from Ref. [12]. Copyright 1998 American Chemical Society

2.2.2 Assembly of Nanoparticles on SAMs

Binder and coworkers described an example of hydrogen bonding interaction for nanoparticle assembly on flat surfaces [14]. The approach is based on the multiple hydrogen bonding interactions of the receptor immobilized on nanoparticles. It was found that the surface coverage of nanoparticles could be adjusted by the density of receptor units in the mixed SAM (Fig. 2.5).

Rotello and coworkers developed nanoparticle assembly on flat surfaces through specific hydrogen bonding interactions [15]. They demonstrated the selective deposition of polystyrene functionalized with complementary diamidopyridine (PS-DAP)/and thymine (PSThy) gels onto prepatterned silicon substrates. These microgel arrays can be cross-linked and selectively and reversibly functionalized by nanoparticles through complementary hydrogen bonding interactions to provide polymer/nanoparticle composite microstructure patterns with fluorescent or magnetic properties.

The same group reported the use of electron-beam lithography (EBL) to pattern a functional polymer "host" template composed of diaminotriazine-functionalized polystyrene via electron-beam-induced cross-linking [16]. After development, the cross-linked polymer pattern provides templates for assembling complementary thymine-functionalized CdSe-ZnS quantum dots (QDs) via three point hydrogen bonding interactions.

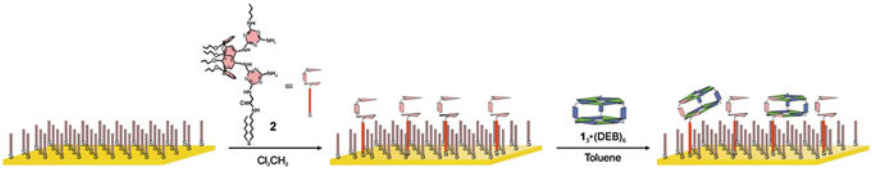

Fig. 2.4 The methodology followed for the growth of assemblies $\mathbf{1}_2.\mathbf{2}.(DEB)_6$ on gold. Reproduced with permission from Ref. [13]. Copyright 2003 The Royal Society of Chemistry

2.3 Metal Coordination Directed Assembly

Metal-directed self-assembly on surfaces has been extensively studied for the construction of supramolecular architectures. Coordination chemistry is of special interest for the assembly, because it offers stable bonding and metal–ligand specificity, also allows the reversible formation and cleavage of the complex by redox processes or the addition of competing ligands.

2.3.1 Assembly of Molecules on SAMs

Abruna et al. have reported ligand–metal assembly on gold for the preparation of redox active mono- and multimetallic systems [17]. Study shows that the surface-bound terpyridine ligand has enough coordination sites to bind other metal ions on the surface (Fig. 2.6a). A similar approach was used by Nishihara and coworkers to build polymetallic complexes on gold by repetitive deposition of an Fe(II) complex with azobenzene-linked bis(terpyridine) ligand [18]. The group of Schubert described the use of a terpyridine–metal complex to reversibly functionalize surfaces [19]. The optical surface properties could be tuned by the choice of the coordinating metal ion. The introduction of suitable coordinating transition metal ions allowed the reversible formation and disassembly of the surface bounded complexes (Fig. 2.6b). Reinhoudt and coworkers used the metal coordination to generate coordination cages directly on surfaces by using self-assembly [20]. Metal-induced coordination allowed the direct measurement of the formation of such assemblies and detection on a single molecule level. The same group also developed a new way to immobilize heterocages on surface by metal coordination [21]. Immobilized heterocages result from the insertion of the thioether-functionalized cavitand into an 11-mercapto undecanol SAM, followed by assembly of cages by complexation of a different cavitand from solution. A different approach for the metal coordination directed assembly was developed by Rubinstein and coworkers [22]. Using bishydroxamate ligands and corresponding metals such as Zr^{4+}, Ce^{4+} and Ti^{4+}, a new type of multilayer structures based on supramolecular metal–ligand interactions has been constructed in a step-by-step manner, resulting

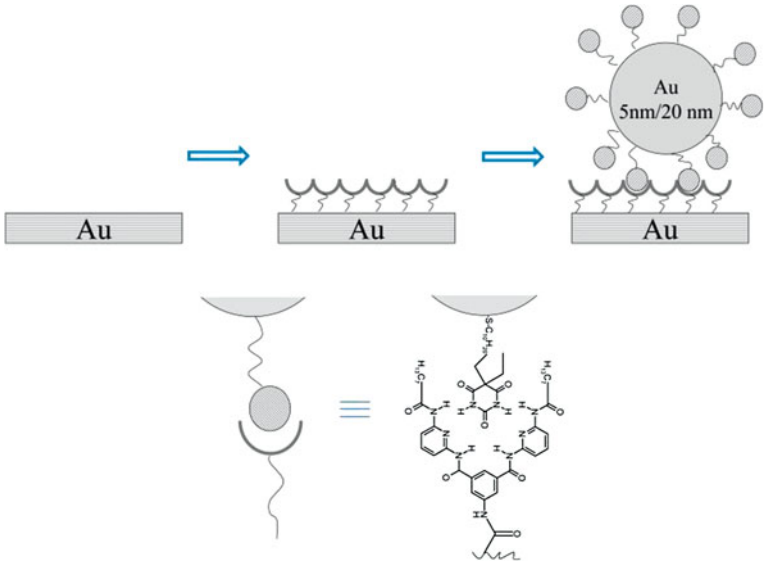

Fig. 2.5 Schematic illustration of hydrogen bonding-directed nanoparticle assembly. Adapted with permission from Ref. 14. Copyright 2005 American Chemical Society

in larger thickness, increased roughness, higher electrical resistivity,and improved stiffness of surfaces (Fig. 2.7).

Mallouk and coworkers used similar type tetravalent-(Zr^{4+}, Hf^{4+}) or divalent (Zn^{2+}, Cu^{2+}) metal ions and phosphonates as a ligand to build up multilayers in a supramolecular metal–ligand coordination manner [23]. Papadimitrakopoulos et al. demonstrated the stepwise self-assembly process of diethyl zinc and bis-quinoline on a silicon substrate resulting in films capable of electroluminescence. Assembled films also showed a high refractive index and uniformity [24]. McGimpsey and coworkers developed a non-covalent metal–ligand coordination for the assembly of supramolecular photocurrent-generating systems [25]. In their system, the light absorbing group (pyrene) was noncovalently coupled to a gold surface via metal–ligand complexation. These systems were noncovalently assembled by sequential deposition of three or more components, showing high stability and high current generation on gold surface.

2.3.2 Assembly of Nanoparticles on SAMs

Murray et al. developed a new way to fabricate monolayer or multilayer films of carboxylate-functionalized gold nanoparticles onto a mercaptoundecanoic acid monolayer [26–29]. Nanoparticles were attached via divalent metal ions (Cu^{2+}, Zn^{2+}, Pb^{2+}). Attachment of additional layers of particles was performed by

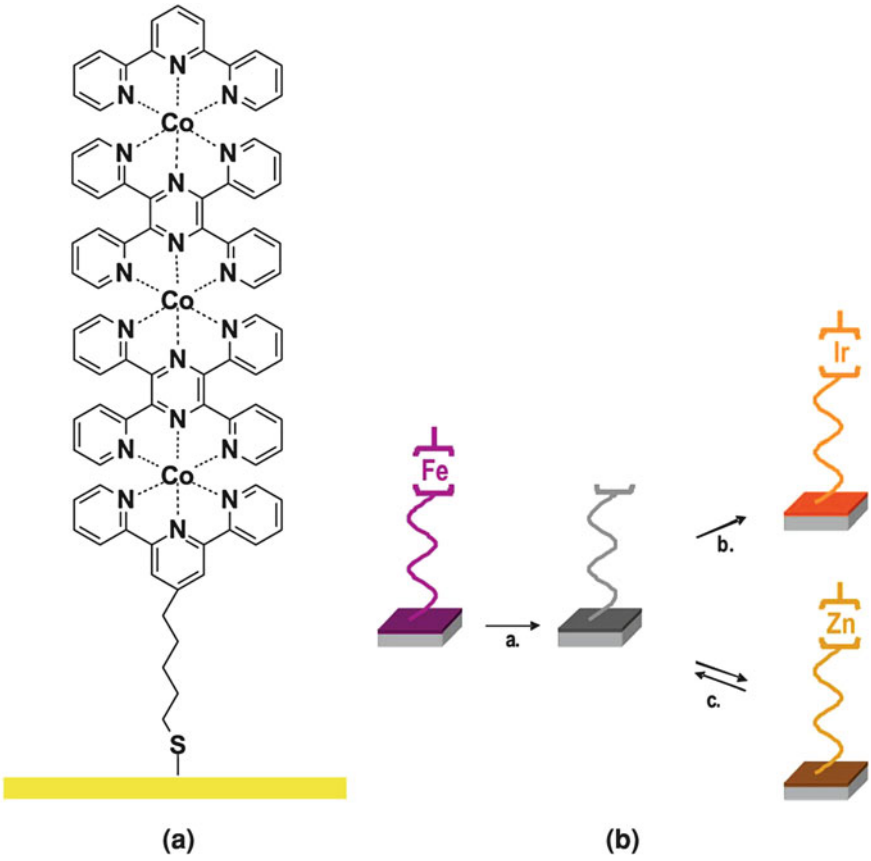

Fig. 2.6 **a** Orthogonal assembly scheme for the construction of terpyridine–metal complex layer on gold. Adapted with permission from Ref. 17. Copyright 1996 American Chemical Society. **b** The attached Fe(II) complex was uncomplexed to obtain the free terpyridine ligands on the substrates *a*. these units can be used for the subsequent complexation with an iridium precursor *b* or with Zn(II) ions; the latter system can be reversibly opened and closed *c*. Reproduced with permission from Ref. [19]. Copyright 2008 American Chemical Society

repeated dipping cycles of metal ions and particles, resulting in the formation of network nanoparticle films. The group of Rubinstein reported gold nanoparticle mono- and multilayers on gold surfaces using coordination chemistry [30]. Au nanoparticles capped with a monolayer of 6-mercaptohexanol were modified by partial substitution of bishydroxamic acid disulfide ligand molecules into their capping layer. A monolayer of the ligand-modified Au nanoparticles was assembled via coordination with Zr^{4+} ions onto a gold substrate precoated with a self-assembled monolayer of the bishydroxamate disulfide ligand. Layer-by-layer construction of nanoparticle multilayers was achieved by alternate binding of Zr^{4+} ions and ligand-modified nanoparticles onto the first nanoparticle layer (Fig. 2.8).

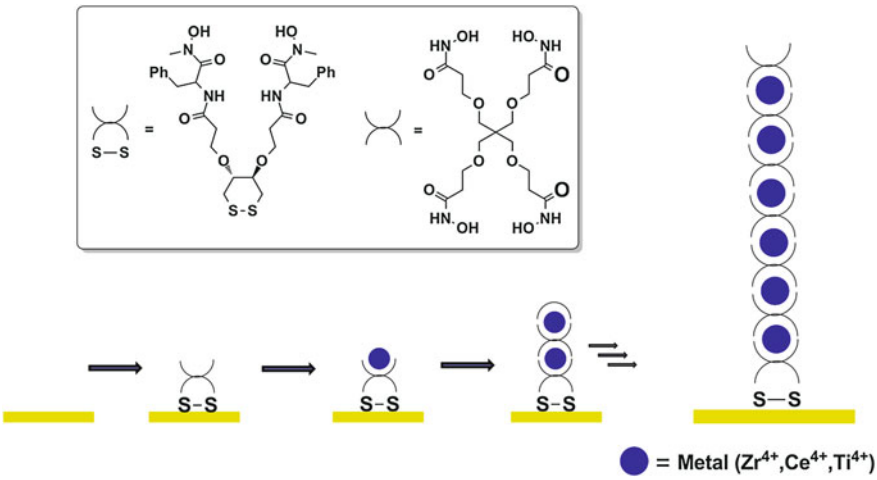

Fig. 2.7 Schematic presentation of the molecules used for multilayer construction and an idealized structure of the coordination-based multilayers. Adapted with permission from Ref. [22]. Copyright 2004 American Chemical Society

Chen and coworkers used metal–ligand coordination (divalent metal ions and pyridine moieties as a ligand) for the assembly of nanoparticles on surfaces [31]. The thickness of the nanoparticle layers was controlled by repetitive alternate dipping cycles (Fig. 2.9).

Reinhoudt et al. used oordination chemistry to grow isolated nanoparticles on surfaces [32]. Pd^{2+}-containing pincer adsorbate molecules were embedded into mercaptoundecanol and decanethiol SAMs on gold. Monolayer-protected Au nanoclusters bearing phosphine moieties at the periphery were coordinated to SAMs containing individual Pd^{2+} pincer molecules via supramolecular metal–ligand interactions.

2.3.3 Assembly by Electrostatic Interactions

One of the most simple and versatile methods for the assembly of 2D and 3D structures is electrostatic self-assembly. The driving force for the assembly is the ionic interaction between oppositely charged entities (polymers, nanoparticles, and substrates), providing the fabrication of functional mono- or multilayer architectures in a stepwise fashion. Electrostatic self-assembly has been the most widely used method for the assembly of the different materials on surfaces. Electrostatic forces are strong enough to create stable assemblies, but weak enough to respond to environmental changes such as variations of ionic strength or pH.

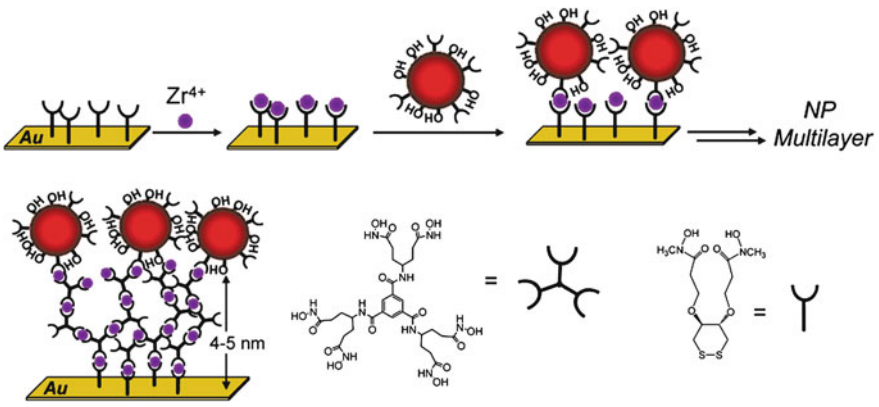

Fig. 2.8 Stepwise assembly of bishydroxamate-bearing Au nanoparticle multilayers onto bishydroxamate disulfide SAMs on a gold surface via Zr^{4+} ions (*top*). Controlled spacing of nanoparticles from the gold surface using a hexahydroxamate ligand (*bottom*). Reproduced with permission from Ref. [30]. Copyright 2005 American Chemical Society

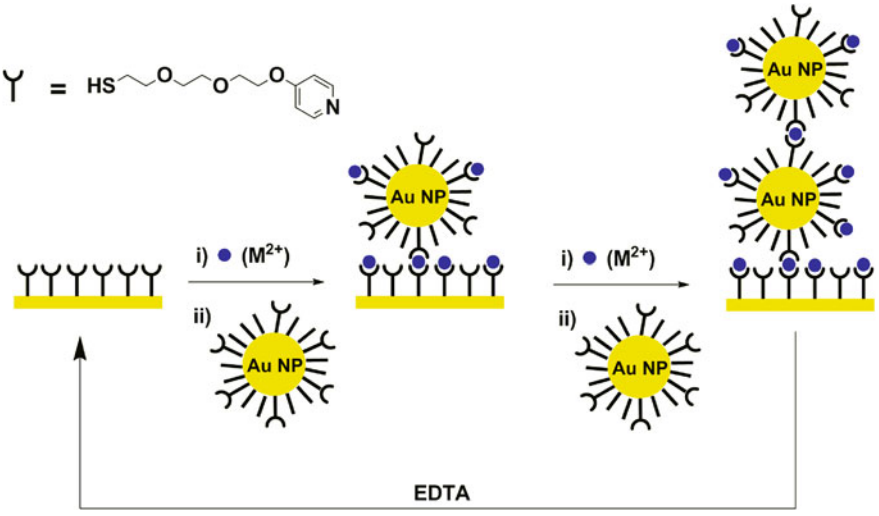

Fig. 2.9 Procedure for nanoparticle assembly by the chelating interactions between divalent (transition) metal ions and pyridine moieties. Adapted with permission from Ref. [31]. Copyright 2002 American Chemical Society

2.3.4 Assembly of Molecules on SAMs

The group of Reinhoudt used electrostatic self-interactions to prepare SAMs of organic radicals on silicon substrates [33]. For this purpose, amino groups on surface were protonated by rinsing with a 4-morpholineethanesulfonic acid

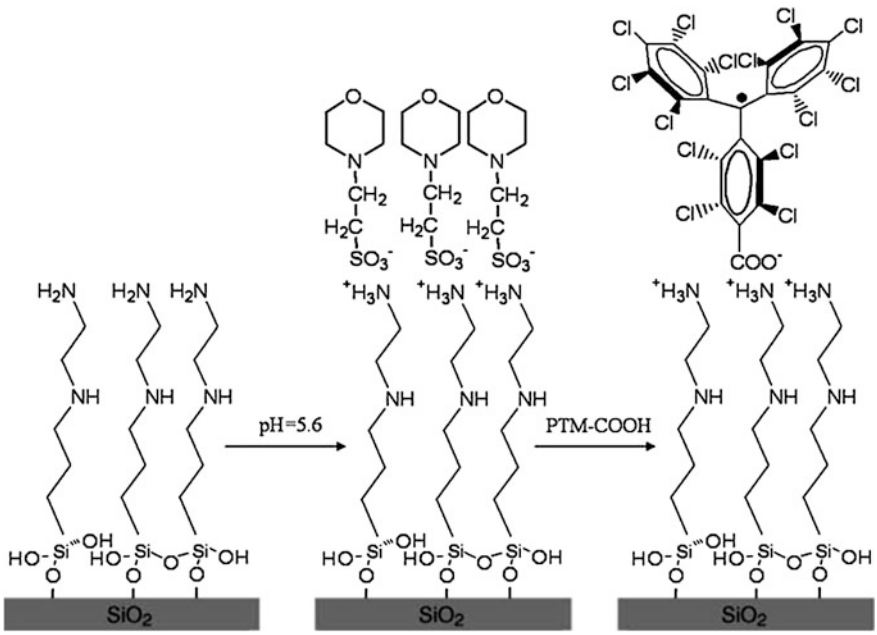

Fig. 2.10 Formation of the polychorotriphenylmethyl (PTM) radical SAMs on a SiO_2 surface by electrostatic interaction. Reproduced with permission from Ref. [33]. Copyright 2007 Wiley–VCH Verlag GmbH & Co. KGaA

monohydrate buffer (pH 5.6) to give a positively charged surface and, subsequently, the substrate was immersed in a solution of 4-carboxytetradecachlorotriphenylmethyl radical (PTMCOOH) to give a SAM of the organic radical (Fig. 2.10). Calvo and coworkers reported the assembly of some enzymes such as glucose and lactate oxidases on gold by electrostatic adsorption [34]. A polycation, poly (allylamine), was assembled onto a gold electrode modified with 3-mercaptopropane-sulfonic acid by electrostatic interaction. Enzymes were also immobilized onto the polycation layer electrostatically.

An approach for the construction of photoactive devices is highly ordered immobilization of photofunctional molecules on surfaces. For that purpose, Tamiaki et al. reported the electrostatic layer-by-layer adsorption of the light-harvesting complexes (chlorosomes) from the green sulfur photosynthetic bacterium *Chlorobium (Chl.) tepidum* onto a glass substrate using the cationic linear polymer polylysine [35]. Burgin and coworkers examined the electrostatic nature of single-walled carbon nanotubes (SWNTs) adsorption on amine surfaces via electrostatic interactions, where both the amine and the SWNTs were treated by various pH buffers prior to solution deposition of nanotubes [36]. In a similar manner, Bao et al. fabricated amine silane SAMs with varying end groups that led to adsorption of submonolayer nanotube network films with varying degrees of

alignment and density [37]. The protonation of amine-coated surfaces influences this adsorption and chirality sorting of SWNTs (Fig. 2.11).

Ionic interactions have also been used for nanoparticle assembly on surfaces. For instance, Auer and coworkers studied the assembly of gold nanoparticles on planar gold surfaces precoated with mercaptohexadecanoic acid using bisbenzamidines as a linker between negatively charged gold nanoparticles and the surface [38]. Murphy and coworkers used gold nanorods to assemble on a surface by electrostatic interaction [39]. Gold nanorods were stabilized with cetyltrimethylammonium bromide (CTAB) and assembled on a gold surface modified with 16-mercaptohexadecanoic acid. Attractive electrostatic interactions between the carboxylic acid group on the SAM and the positively charged CTAB molecules are likely responsible for the nanorod immobilization (Fig. 2.12).

A similar approach was used by Sastry and coworkers [40]. They described the formation of self-assembled monolayers (SAMs) of an aromatic bifunctional molecule, 4-aminothiophenol (4-ATP) on gold and the subsequent organization of carboxylic acid derivatized silver colloidal particles.

The controlled organization and precise positioning of nanoparticles on 2D surfaces are essential for the development of new functional materials. Some studies focused on the combination of top-down surface patterning with self-assembly of particles via electrostatic interactions. For example, patterning by photolithography [41–43], soft lithography [44, 45], nanoimprint lithography [46], and scanning probe lithography[47–55] have been widely used for the fabrication of electrostatically assembled nanoparticles on patterned surfaces.

2.3.5 Assembly by Host–Guest Interactions

Host–guest chemistry plays an important role in the construction of supramolecular architectures on surfaces. Calixarenes, cucurbiturils (CB), and cyclodextrins (CD) are interesting host molecules which form stable and specific inclusion complexes with a variety of organic guest molecules. Monolayers of these host molecules on surfaces constitute the unique platforms for the immobilization of various guest molecules in a multivalent supramolecular fashion. This section describes the supramolecular assembly onto different receptor surfaces by host–guest interactions.

2.3.6 Assembly of Molecules on SAMs

Calixarene monolayers have been synthesized and charaterized extensively by the group of Reinhoudt [56–58]. Calixarenes formed well-packed and ordered monolayers capable of interacting with different guest molecules in aqueous solution. Gupta and coworkers showed that calix[4]arene monolayers could discriminate

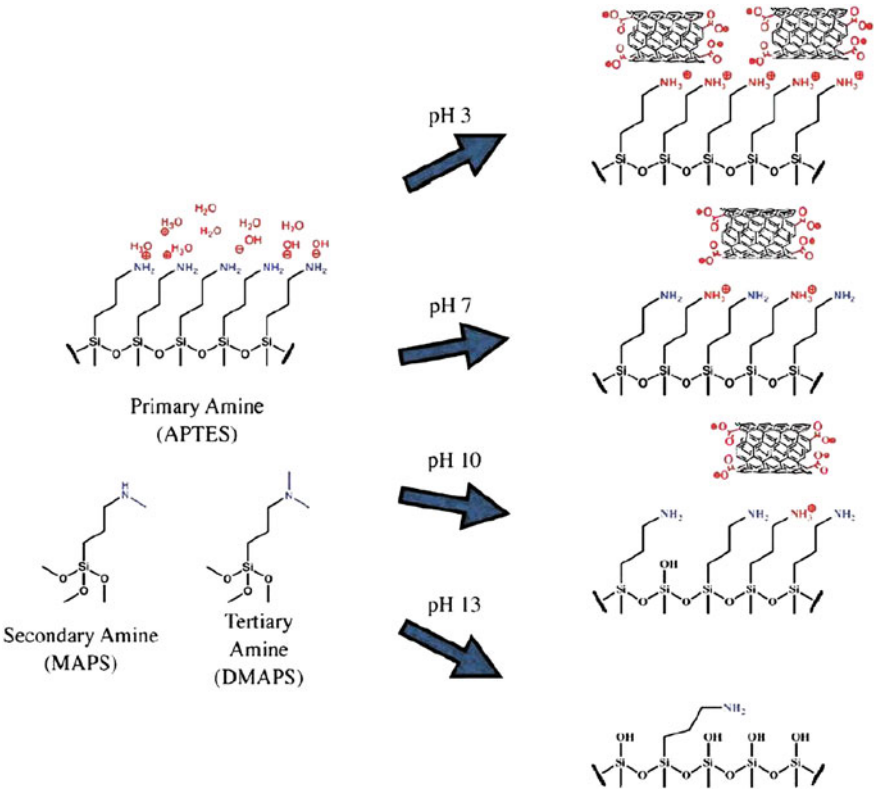

Fig. 2.11 Schematic illustration of influence of protonation on SWNTs adsorption. Reproduced with permission from ref [29]. Copyright 2010 American Chemical Society

between two structural isomers of hydroxybutyrolactone by surface immobilization of the receptor units [59].

Monolayers of cucurbit[6]uril, a macrocyclic cavitand comprising six glycoluril units, have been described by Kim and coworkers [60]. Alkene functionalized CB[6] was reacted with surface-immobilized thiols under UV light, resulting in CB[6] monolayers on a glass surface. The CB[6] modified glass recognizes small molecules such as spermine which is known to form a stable host–guest complex with CB[6] (Fig. 2.13).

Zhang et al. described a general protocol based on the spontaneous adsorption of cucurbit[n]uril (CB[n]) molecules through a strong multivalent interaction between CB[n] and gold [61]. Their method does not require any prior modification or special treatment of CB[n] molecules, and is applicable for all members of the CB[n] family, at least CB[6–8] (Fig. 2.14).

Jonkheijm and coworkers also used a CB[7] monolayer for the immobilization of the proteins through a monovalent supramolecular interaction [62]. Their technique allows printing of stable protein monolayers in well-defined formats to

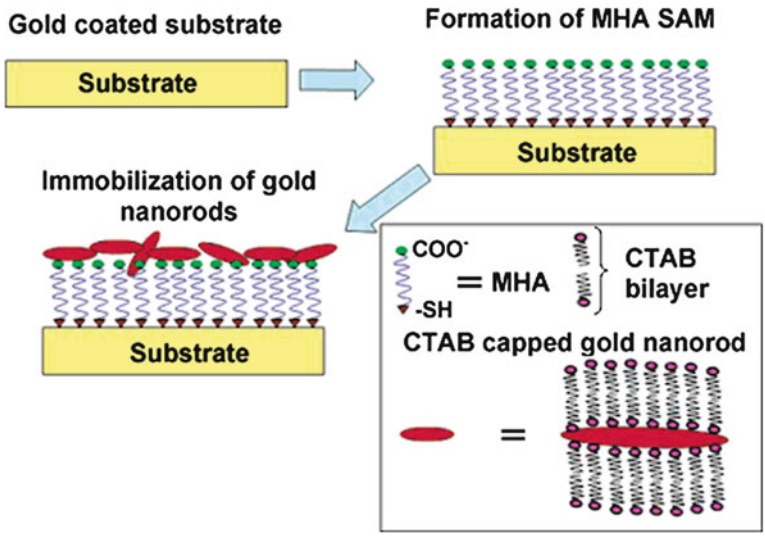

Fig. 2.12 Schematic immobilization of CTAB-Modified Gold Nanorods onto SAMs of 16-MHA. Reproduced with permission from Ref. [39]. Copyright 2004 American Chemical Society

be achieved with controlled protein orientation and with subsequent replacement of the protein monolayer by a small synthetic ligand (Fig. 2.15).

Monolayers of cyclodextrin (CD SAMs) have been studied and extensively characterized. The immobilization of a wide range of (bio)molecules functionalized with multiple guest units onto CD SAMs on gold and silicon oxide surfaces have been reported by different research groups (Fig. 2.16) [63–67]. Huskens and Reinhoudt et al. introduced the concept of "molecular printboards", for the stable positioning and assembly of guest-functionalized dendrimers [68], nanoparticles [69], proteins [70], and fluorescent small molecules[71] onto CD SAMs. Molecular patterns of (bio)molecules have also been prepared on these molecular printboards by using lithographic techniques such as microcontact printing and dip-pen nanolithography [46, 72–74].

2.4 Combination of Different Orthogonal Supramolecular Interaction Motifs

All supramolecular interactions reviewed here, i.e., hydrogen bonding, metal–ligand coordination, electrostatic, and host–guest interactions, have in common a high level of structural definition and tunable strength, which allow the design of functional materials at the molecular level. As discussed above, these weak

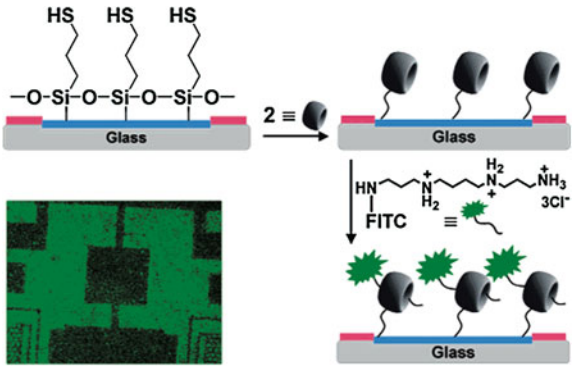

Fig. 2.13 Cartoon for anchoring a CB[6] derivative onto a patterned glass and detection of fluorescently labeled spermine by the CB[6] modified surface. Reproduced with permission from Ref. [60]. Copyright 2003 American Chemical Society

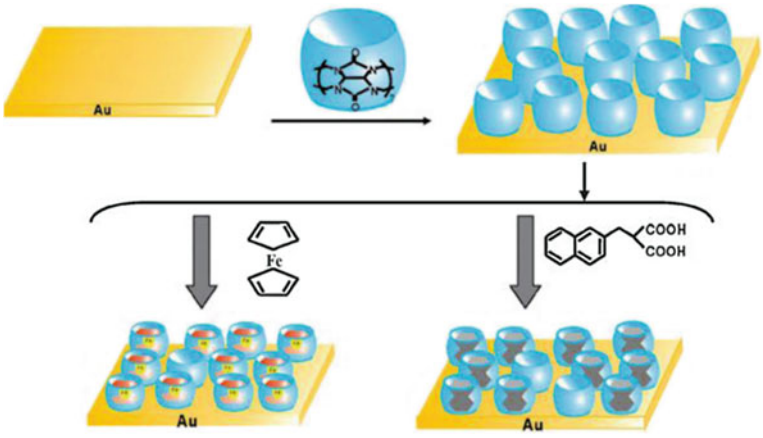

Fig. 2.14 Schematic illustration of the construction of a self-assembled CB[n] monolayer on a gold surface and the formation of inclusion complexes. Reproduced with permission from Ref. [61]. Copyright 2008 The Royal Society of Chemistry

interactions were employed individually to build functional supramolecular architectures on surfaces. The combination of different orthogonal supramolecular interaction motifs is essential for the fabrication of complex hybrid organic–inorganic materials and stimuli-responsive surfaces. This section highlights the recent developments of the combination of different orthogonal interaction motifs to yield hierarchical supramolecular assemblies on surfaces.

Huskens et al. have described the combination of different orthogonal supramolecular systems on molecular printboards. In a first study, they demonstrated the immobilization of a supramolecular capsule at the surface [75]. Two different orthogonal systems, host–guest and electrostatic interactions, were utilized to generate a capsule on a surface. To build such a supramolecular capsule, they used noncovalent attachment of one component of the molecular capsule on the CD SAM via orthogonal host–guest interaction followed by the self-assembly of the

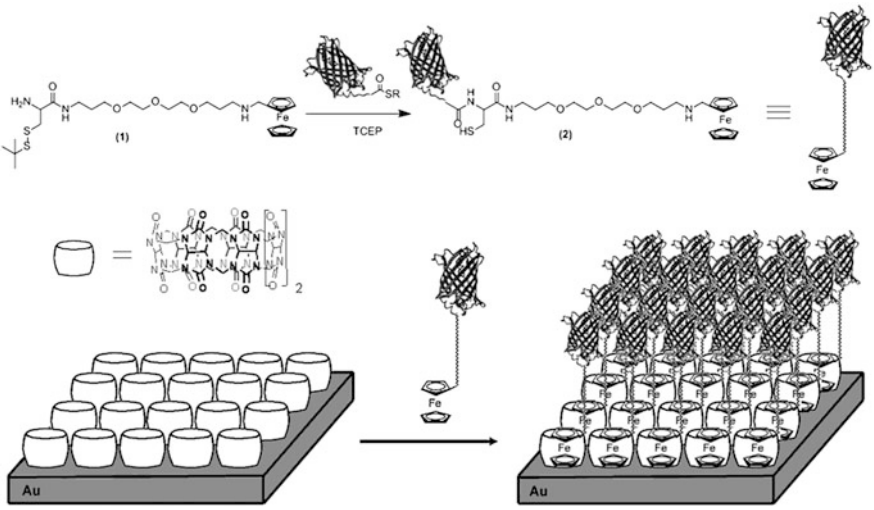

Fig. 2.15 Ligation of a ferrocene-cysteine derivative (*1*) with yellow fluorescent protein (YFP) and immobilization of the resulting ferrocene-YFP (*2*) onto a CB[7] monolayer. Reproduced with permission from Ref. [62]. Copyright 2010 Wiley–VCH Verlag GmbH & Co. KGaA

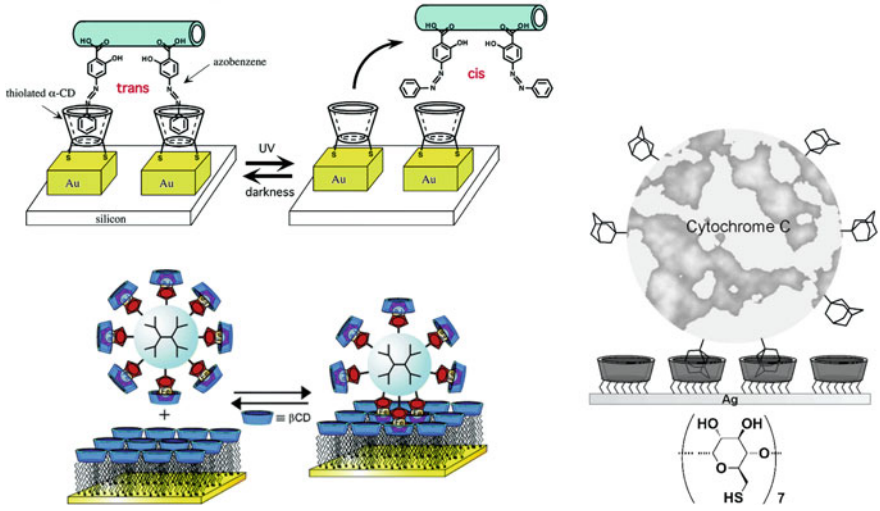

Fig. 2.16 Supramolecular interaction motifs at CD SAMs. Reproduced with permission from Ref. 64 (Copyright 2003 American Chemical Society), Ref. 66 (Copyright 2002 American Chemical Society), Ref. 67 (Copyright 2004 American Chemical Society)

second component at the interface through ionic interaction (Fig. 2.17a). Another study describes the multivalent binding of a supramolecular complex at a multivalent host surface by combining the orthogonal CD host–guest and metal ion-

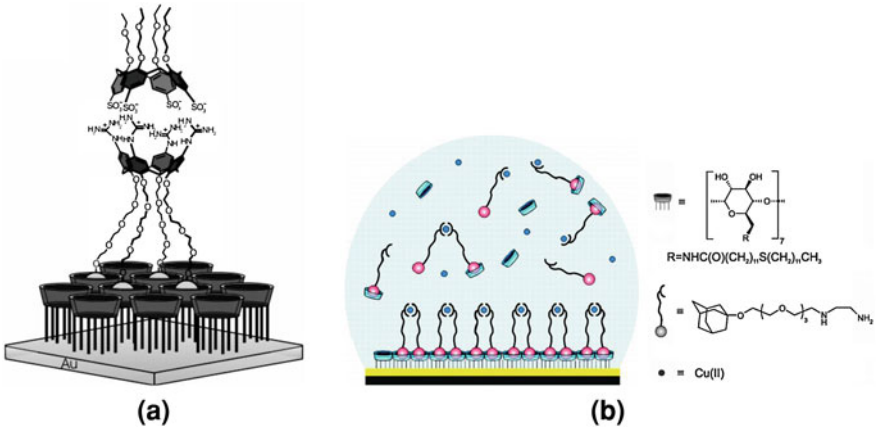

Fig. 2.17 **a** Formation of molecular capsule at CD SAMs via host–guest and electrostatic interactions. Reproduced with permission from Ref. 75. Copyright 2004 American Chemical Society. **b** Complex formation on CD SAMs by host–guest and metal–ligand coordination. Reproduced with permission from Ref. [76]. Copyright 2006 American Chemical Society

ethylenediamine coordination motifs [76]. In this orthogonal supramolecular system, a heterotropic divalent linker, with a CD-complexing adamantyl (Ad) group and an M(II)-complexing ethylenediamine ligand, is employed. This allows the linker to bind to CD in solution as well as to CD immobilized at SAMs (Fig. 2.17b). A similar study describes the preparation of vesicles bearing host units (cyclodextrin) and their interactions with guest (adamantyl) functionalized ligands via orthogonal multivalent host–guest and metal–ligand complexation [77]. Vesicles of amphiphilic cyclodextrin recognized metal coordination complexes with adamantyl ligands via inclusion in the host cavities at the vesicle surface. In the case of divalent Cu(II) complexes, the interaction was predominantly intravesicular. In the case of Ni(II), the interaction was effectively intervesicular, and addition of the guest–metal complex resulted in aggregation of the vesicles into dense, multilamellar clusters. The valency of molecular recognition at the surface of vesicles and the balance between intravesicular and intervesicular interaction could be tuned by metal coordination of guest molecules. Another study, they presented the attachment of streptavidin (SAv) to CD SAM via orthogonal host–guest and SAv–biotin interactions [78]. The orthogonal linkers consist of a biotin functionality for binding to SAv and adamantyl functionalities for host–guest interactions at CD SAM. The approach was used for build up and patterning of protein nanostructures at interfaces using a sequence of host–guest and SAv-biotin interaction.

The encapsulation of anionic dyes in immobilized dendrimers has been described to occur via orthogonal multivalent host–guest and electrostatic interactions [79]. Fifth-generation poly(propylene imine) dendrimers, modified with 64 apolar adamantyl groups, have been immobilized on cyclodextrin host monolayers

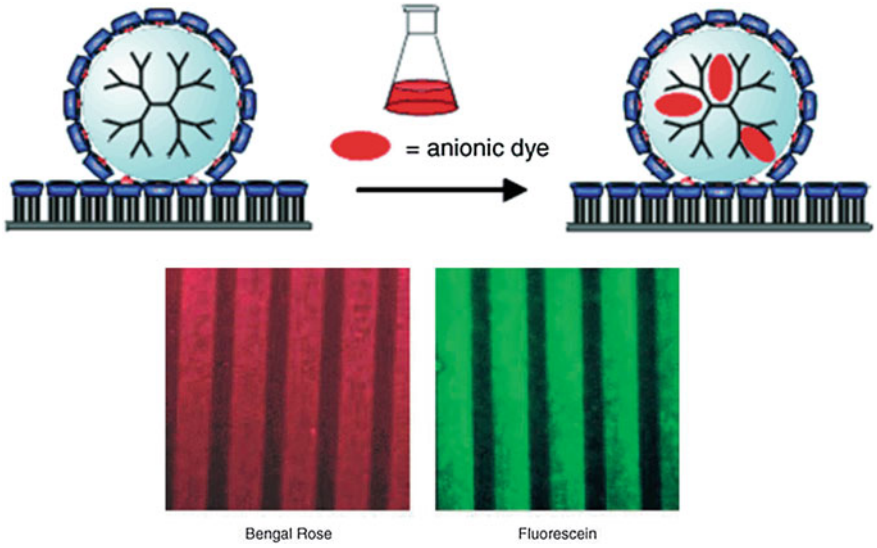

Fig. 2.18 Schematic representation of the filling of immobilized dendrimer patterns with anionic dyes (*upper*). Confocal microscopy images after microcontact printing of dendrimer on a molecular printboard, followed by filling of the immobilized dendrimers with Bengal Rose and fluorescein dyes (*lower*). Reproduced with permission from Ref. [79]. Copyright 2005 Wiley–VCH Verlag GmbH & Co. KGaA

on glass by supramolecular microcontact printing. The immobilized dendrimers retained their guest binding properties and functioned as "molecular boxes" that can be filled with fluorescent dye molecules from solution (Fig. 2.18).

The versatility and advantages of the molecular printboard for attaching proteins, for example, controllable binding constants and the suppression of non-specific interactions, were combined with His-tagged proteins via host–guest and metal–ligand interactions [80, 81]. His_6-tagged proteins have been attached to a molecular print board in a selective manner by using the supramolecular blocking agent **3** and Ni·**4** as depicted in Fig. 2.19.

Another contribution describes the patterning of silica substrates with thymine as hydrogen bonding unit and positively charged *N*-methylpyridinium-containing polymers using photolithography, and the subsequent orthogonal supramolecular modification of these surfaces using diaminopyridine-functionalized polystyrene and carboxylate-derivatized CdSe/ZnS core–shell nanoparticles through the combination of diaminopyridine–thymine hydrogen bonding and pyridinium-carboxylate electrostatic interactions (Fig. 2.20) [82].

The group of Haga developed DNA nanowires via orthogonal self-assembly by assistance of a SAM on the surface [83]. Orthogonal self-assembly was applied to the surface for the selective modification of the DNA capture molecules on the Au electrode. Two anchor groups of thiol and phosphonic acid were used to discriminate between Au and SiO_2, since a thiol group selectively attaches to the Au

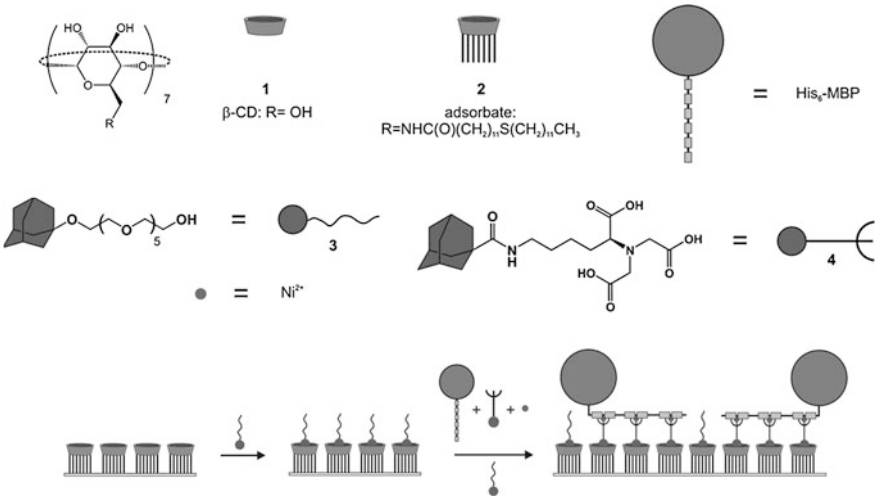

Fig. 2.19 Structures of compounds: β-cyclodextrin **1**, adsorbate for SAMs on gold **2**, adamantyl linkers **3** and **4**, nickel, His_6-MBP and cartoon for the binding of His_6-MBP through Ni·**4** to CD SAMs, in competition with monovalent blocking agent **3**. Reproduced with permission from Refs. [80, 81]. Copyright 2008 Wiley–VCH Verlag GmbH & Co. KGaA

surface and a phosphonate group attaches to the SiO_2 surface. Once the DNA trapping molecule is selectively attached to gold patterns on silicon substrate, DNA is captured from solution and used as a nanowire between two gold patterns (Fig. 2.21).

An example of the combination of electrostatic interaction with π-π stacking on a surface has been reported by Shinkai and coworkers [84]. They used a hexacationic homooxacalix[3]arene–[60]fullerene 2:1 complex to make a monolayer or a monolayer-like ultra-thin film on an anion-coated gold surface. They also studied the photoelectrochemical response of the monolayers under UV-irradiation (Fig. 2.22).

Tait et al. developed the concept of stabilizing and ordering 1D coordination structures at a surface [85]. Hydrogen bonding interactions with the second molecular species improved the stability and ordering of the copper-pyridyl 1D coordination chains. This combination of the selective orthogonal interactions allowed the fine-tuning of the supramolecular system by choice of the building blocks. In the group of Dalcalane, hierarchical assembly on silicon using host–guest and hydrogen bonding interactions was developed [86]. The multistep growth of supramolecular structures on the surface resulted from the combined use of orthogonal host–guest and hydrogen bonding interactions. Using this strategy, hybrid and multifunctional materials could be constructed. Fasel et al. reported the two-dimensional mono- and bicomponent self-assembly of three closely related diaminotriazine-based molecular building blocks and a complementary perylene-tetracarboxylic diimide with the interplay of hydrogen bonding, dipolar interactions,

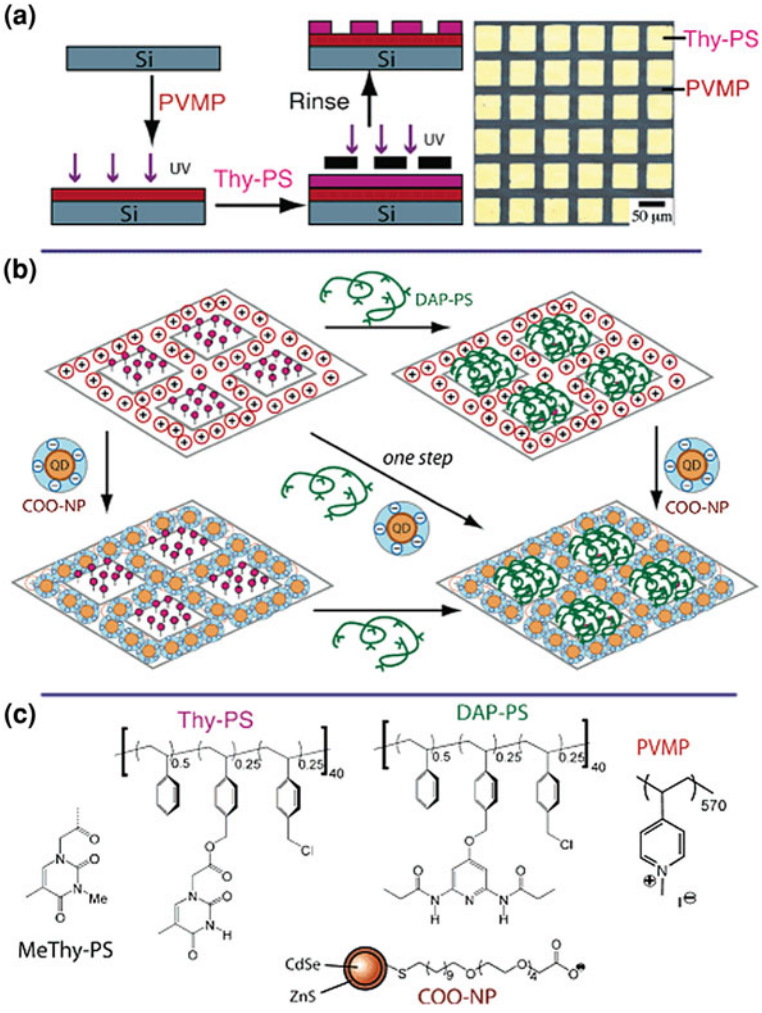

Fig. 2.20 Schematic illustration of the fabrication process. **a** Formation of the patterned PVMP/Thy-PS surface and optical micrograph of the resulting pattern. **b** One-step and sequential orthogonal functionalization by DAP-PS and COO-NP through PS-Thy:PS-DAP recognition and PVMP:COO-NP electrostatic interactions. **c** Chemical structures of the materials, including control polymer MeThy-PS. Reproduced with permission from Ref. [82]. Copyright 2006 American Chemical Society

and metal coordination [87]. They showed that the simplest molecular species, bis-diaminotriazine-benzene, only interacts via hydrogen bonds and forms a unique supramolecular pattern on a gold surface. For the two related molecular species, which exhibit in addition to hydrogen bonding also dipolar interactions and metal coordination, the number of distinct supramolecular structures increases

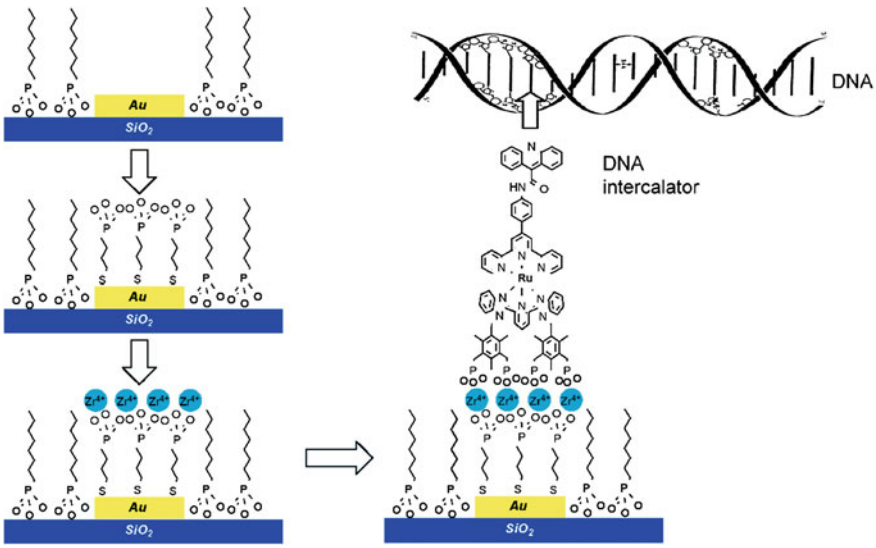

Fig. 2.21 Schematic illustration of surface modification for DNA capture by metal coordination-directed orthogonal assembly on gold-patterned silicon. Reproduced with permission from Ref. [83]. Copyright 2008 American Chemical Society

dramatically with the number of possible hierarchical assemblies with orthogonal interactions.

2.5 Conclusions

The use of supramolecular chemistry and molecular self-assembly including hydrogen bonding, metal coordination, electrostatic and host–guest interactions to direct the immobilization of functional systems on surfaces have attracted considerable attention in modern research due to their special characteristic features such as high specificity, controlled affinity, and reversibility. In this chapter some examples of orthogonal supramolecular interactions for the construction of functional materials with tunable properties on flat surfaces have been reviewed. Although these noncovalent interactions were used in many studies individually to build supramolecular architectures on surfaces, there are only limited numbers of examples that address the combination of different supramolecular interactions for the generation of functional monolayers. Hence, the development of hierarchical assemblies by using the combination of different noncovalent interactions still requires more efforts to allow the fabrication of functional surfaces. In this thesis, the concept of orthogonal supramolecular assembly is employed to form functional monolayers that are promising in sensor applications.

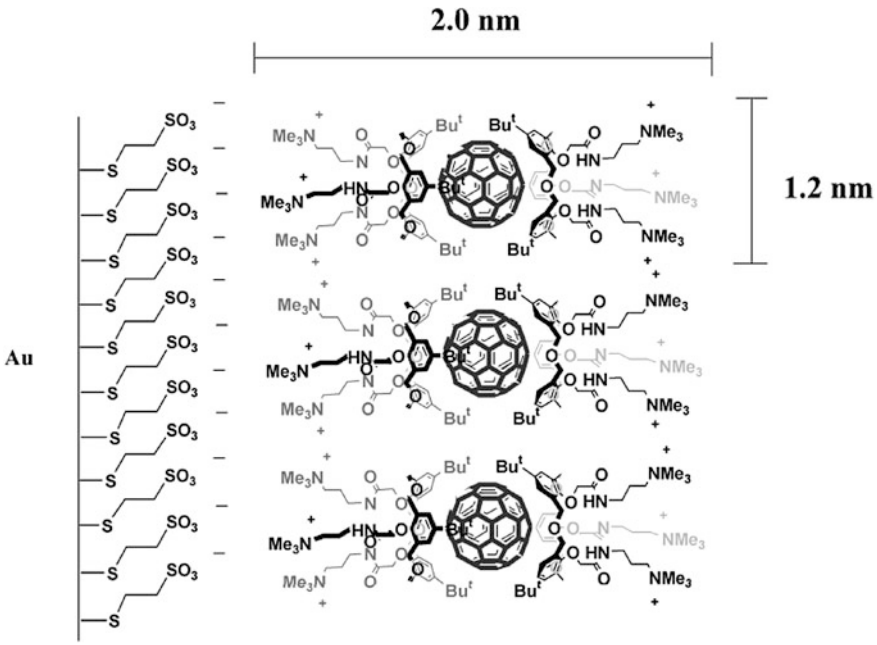

Fig. 2.22 Adsorption of sodium 2-mercaptoethanesulfonate (*first layer*) and 1–[60]fullerene (*second layer*) on a gold surface. Reproduced with permission from Ref. 84. Copyright 2000 The Royal Society of Chemistry

References

1. J.-M. Lehn, *Supramolecular Chemistry Concepts and Perspectives* (VCH, Germany, 1995)
2. T.J. Gardner, C.D. Frisbie, M.S. Wrighton, J. Am. Chem. Soc. **117**, 6927–6933 (1995)
3. J.J. Hickman, P.E. Laibinis, D.I. Auerbach, C.F. Zou, T.J. Gardner, G.M. Whitesides, M.S. Wrighton, Langmuir **8**, 357–359 (1992)
4. P.E. Laibinis, J.J. Hickman, M.S. Wrighton, G.M. Whitesides, Science **245**, 845–847 (1989)
5. J.M. Pollino, M. Weck, Chem. Soc. Rev. **34**, 193–207 (2005)
6. J. Tien, A. Terfort, G.M. Whitesides, Langmuir **13**, 5349–5355 (1997)
7. J.A.A.W. Elemans, A.E. Rowan, R.J.M. Nolte, J. Mater. Chem. **13**, 2661–2670 (2003)
8. H. Hofmeier, U.S. Schubert, Chem Commun. 2423–2432 (2005)
9. G.M. Credo, A.K. Boal, K. Das, T.H. Galow, V.M. Rotello, D.L. Feldheim, C.B. Gorman, J. Am. Chem. Soc. **124**, 9036–9037 (2002)
10. T.B. Norsten, E. Jeoung, R.J. Thibault, V.M. Rotello, Langmuir **19**, 7089–7093 (2003)
11. G. Cooke, J. Couet, J.F. Garety, C.Q. Ma, S. Mabruk, G. Rabani, V.M. Rotello, V. Sindelar, P. Woisel, Tetrahedron Lett. **47**, 3763–3766 (2006)
12. K. Motesharei, D.C. Myles, J. Am. Chem. Soc. **120**, 7328–7336 (1998)
13. J.J. Garcia-Lopez, S. Zapotoczny, P. Timmerman, F.C.J.M. van Veggel, G.J. Vancso, M. Crego-Calama, D.N. Reinhoudt, Chem. Commun. 352–353 (2003)
14. R. Zirbs, F. Kienberger, P. Hinterdorfer, W.H. Binder, Langmuir **21**, 8414–8421 (2005)
15. X. Yu, B. Samanta, H. Xu, P. Arumugam, Y. Ofir, B.J. Jordan, V.M. Rotello, Small **5**, 86–89 (2009)

16. C. Subramani, S. Dickert, Y.C. Yeh, M.T. Tuominen, V.M. Rotello, Langmuir **27**, 1543–1545 (2011)
17. M. Maskus, H.D. Abruna, Langmuir **12**, 4455–4462 (1996)
18. K. Kanaizuka, M. Murata, Y. Nishimori, I. Mori, K. Nishio, H. Masuda, H. Nishihara, Chem. Lett. **34**, 534–535 (2005)
19. C. Haensch, M. Chiper, C. Ulbricht, A. Winter, S. Hoeppener, U.S. Schubert, Langmuir **24**, 12981–12985 (2008)
20. S.A. Levi, P. Guatteri, F.C.J.M. van Veggel, G.J. Vancso, E. Dalcanale, D.N. Reinhoudt, Angew. Chem. Int. Ed. **40**, 1892–1896 (2001)
21. E. Menozzi, R. Pinalli, E.A. Speets, B.J. Ravoo, E. Dalcanale, D.N. Reinhoudt, Chem. Eur. J. **10**, 2199–2206 (2004)
22. I. Doron-Mor, H. Cohen, S.R. Cohen, R. Popovitz-Biro, A. Shanzer, A. Vaskevich, I. Rubinstein, Langmuir **20**, 10727–10733 (2004)
23. H.C. Yang, K. Aoki, H.G. Hong, D.D. Sackett, M.F. Arendt, S.L. Yau, C.M. Bell, T.E. Mallouk, J. Am. Chem. Soc. **115**, 11855–11862 (1993)
24. D.L. Thomsen, T. Phely-Bobin, F. Papadimitrakopoulos, J. Am. Chem. Soc. **120**, 6177–6178 (1998)
25. E. Soto, J.C. MacDonald, C.G.F. Cooper, W.G. McGimpsey, J. Am. Chem. Soc. **125**, 2838–2839 (2003)
26. C. Templeton, F.P. Zamborini, W.P. Wuelfing, R.W. Murray, Langmuir **16**, 6682–6688 (2000)
27. W.P. Wuelfing, F.P. Zamborini, A.C. Templeton, X.G. Wen, H. Yoon, R.W. Murray, Chem. Mater. **13**, 87–95 (2001)
28. F.P. Zamborini, J.F. Hicks, R.W. Murray, J. Am. Chem. Soc. **122**, 4514–4515 (2000)
29. F.P. Zamborini, M.C. Leopold, J.F. Hicks, P.J. Kulesza, M.A. Malik, R.W. Murray, J. Am. Chem. Soc. **124**, 8958–8964 (2002)
30. M. Wanunu, R. Popovitz-Biro, H. Cohen, A. Vaskevich, I. Rubinstein, J. Am. Chem. Soc. **127**, 9207–9215 (2005)
31. S.W. Chen, R.J. Pei, T.F. Zhao, D.J. Dyer, J. Phys. Chem. B **106**, 1903–1908 (2002)
32. H.J. van Friggeri, T. Manen, X.M. Auletta, S. Li, H. Zapotoczny, G.J. Schonherr, J. Vancso, F.C.J.M. van Huskens, D.N. Veggel, J. Reinhoudt, J. Am. Chem. Soc. **123**, 6388–6395 (2001)
33. N. Crivillers, M. Mas-Torrent, S. Perruchas, N. Roques, J. Vidal-Gancedo, J. Veciana, C. Rovira, L. Basabe-Desmonts, B.J. Ravoo, M. Crego-Calama, D.N. Reinhoudt, Angew. Chem. Int. Ed. **46**, 2215–2219 (2007)
34. E.J. Calvo, F. Battaglini, C. Danilowicz, A. Wolosiuk, M. Otero, Faraday Discuss. 47–65 (2000)
35. Y. Saga, T.Y. Kim, T. Hisai, H. Tamiaki, Thin Solid Films **500**, 278–282 (2006)
36. T.P. Burgin, J.C. Lewenstein, D. Werho, Langmuir **21**, 6596–6602 (2005)
37. J.P. Opatkiewicz, M.C. LeMieux, Z.N. Bao, ACS Nano **4**, 1167–1177 (2010)
38. F. Auer, M. Scotti, A. Ulman, R. Jordan, B. Sellergren, J. Garno, G.Y. Liu, Langmuir **16**, 7554–7557 (2000)
39. A. Gole, C.J. Orendorff, C.J. Murphy, Langmuir **20**, 7117–7122 (2004)
40. A. Gole, S.R. Sainkar, S.R. Sastry, Chem. Mater. **12**, 1234–1239 (2000)
41. K. Akamatsu, A. Kimura, H. Matsubara, S. Ikeda, H. Nawafune, Langmuir **21**, 8099–8102 (2005)
42. C.A. Fustin, G. Glasser, H.W. Spiess, U. Jonas, Langmuir **20**, 9114–9123 (2004)
43. H. Tanaka, M. Mitsuishi, T. Miyashita, Langmuir **19**, 3103–3105 (2003)
44. J.W. Zheng, Z.H. Zhu, H.F. Chen, Z.F. Liu, Langmuir **16**, 4409–4412 (2000)
45. D.J. Zhou, A. Bruckbauer, C. Abell, D. Klenerman, D.J. Kang, Adv. Mater. **17**, 1243–1248 (2005)
46. P. Maury, M. Peter, V. Mahalingam, D.N. Reinhoudt, J. Huskens, Adv. Funct. Mater. **15**, 451–457 (2005)
47. L.M. Demers, C.A. Mirkin, Angew. Chem. Int. Ed. **40**, 3069–3071 (2001)

48. J.C. Garno, Y.Y. Yang, N.A. Amro, S. Cruchon-Dupeyrat, S.W. Chen, G.Y. Liu, Nano Lett. **3**, 389–395 (2003)
49. S. Hoeppener, R. Maoz, S.R. Cohen, L.F. Chi, H. Fuchs, J. Sagiv, Adv. Mater. **14**, 1036–1041 (2002)
50. S. Hoeppener, U.S. Schubert, Small **1**, 628–632 (2005)
51. S.T. Liu, R. Maoz, J. Sagiv, Nano Lett. **4**, 845–851 (2004)
52. S.T. Liu, R. Maoz, G. Schmid, J. Sagiv, Nano Lett. **2**, 1055–1060 (2002)
53. R. Maoz, S.R. Cohen, J. Sagiv, Adv. Mater. **11**, 55–61 (1999)
54. R. Maoz, E. Frydman, S.R. Cohen, J. Sagiv, Adv. Mater. **12**, 725–731 (2000)
55. D. Wouters, U.S. Schubert, Mater. Chem. **15**, 2353–2355 (2005)
56. A. Friggeri, F.C.J.M. van Veggel, D.N. Reinhoudt, Chem. Eur. J. **5**, 3595–3602 (1999)
57. A. Friggeri, F.C.J.M. van Veggel, D.N. Reinhoudt, R.P.H. Kooyman, Langmuir **14**, 5457–5463 (1998)
58. B.H. Huisman, R.P.H. Kooyman, F.C.J.M. van Veggel, D.N. Reinhoudt, Adv. Mater. **8**, 561–564 (1996)
59. J.D. Faull, V.K. Gupta, Langmuir **17**, 1470–1476 (2001)
60. S.Y. Jon, N. Selvapalam, D.H. Oh, J.K. Kang, S.Y. Kim, Y.J. Jeon, J.W. Lee, K. Kim, J. Am. Chem. Soc. **125**, 10186–10187 (2003)
61. Q. An, G.T. Li, C.G. Tao, Y. Li, Y.G. Wu, W.X. Zhang, Chem. Commun. 1989–1991 (2008)
62. J.F. Young, H.D. Nguyen, L.T. Yang, J. Huskens, P. Jonkheijm, L. Brunsveld, ChemBioChem **11**, 180–183 (2010)
63. T. Auletta, B. Dordi, A. Mulder, A. Sartori, S. Onclin, C.M. Bruinink, M. Peter, C.A. Nijhuis, H. Beijleveld, H. Schonherr, G.J. Vancso, A. Casnati, R. Ungaro, B.J. Ravoo, J. Huskens, D.N. Reinhoudt, Angew. Chem. Int. Ed. **43**, 369–373 (2004)
64. I.A. Banerjee, L.T. Yu, H. Matsui, J. Am. Chem. Soc. **125**, 9542–9543 (2003)
65. M.R. de Jong, J. Huskens, D.N. Reinhoudt, Chem. Eur. J. **7**, 4164–4170 (2001)
66. A. Fragoso, J. Caballero, E. Almirall, R. Villalonga, R. Cao, Langmuir **18**, 5051–5054 (2002)
67. C.A. Nijhuis, J. Huskens, D.N. Reinhoudt, J. Am. Chem. Soc. **126**, 12266–12267 (2004)
68. C.A. Nijhuis, K.A. Dolatowska, B.J. Ravoo, J. Huskens, D.N. Reinhoudt, Chem. Eur. J. **13**, 69–80 (2007)
69. X.Y. Ling, D.N. Reinhoudt, J. Huskens, Chem. Mater. **20**, 3574–3578 (2008)
70. M.J.W. Ludden, X. Li, J. Greve, A. van Amerongen, M. Escalante, V. Subramaniam, D.N. Reinhoudt, J. Huskens, J. Am. Chem. Soc. **130**, 6964–6973 (2008)
71. A. Mulder, S. Onclin, M. Peter, J.P. Hoogenboom, H. Beijleveld, J. ter Maat, M.F. Garcia-Parajo, B.J. Ravoo, J. Huskens, N.F. van Hulst, D.N. Reinhoudt, Small **1**, 242–253 (2005)
72. O. Crespo-Biel, B. Dordi, P. Maury, M. Peter, D.N. Reinhoudt, J. Huskens, Chem. Mater. **18**, 2545–2551 (2006)
73. P. Maury, M. Escalante, M. Peter, D.N. Reinhoudt, V. Subramaniam, J. Huskens, Small **3**, 1584–1592 (2007)
74. P. Maury, M. Peter, O. Crespo-Biel, X.Y. Ling, D.N. Reinhoudt, J. Huskens, Nanotechnology **18**, 044007
75. A. Mulder, T. Auletta, A. Sartori, S. Del Ciotto, A. Casnati, R. Ungaro, J. Huskens, D.N. Reinhoudt, Am. Chem. Soc. **126**, 6627–6636 (2004)
76. O. Crespo-Biel, C.W. Lim, B.J. Ravoo, D.N. Reinhoudt, J. Huskens, J. Am. Chem. Soc. **128**, 17024–17032 (2006)
77. C.W. Lim, O. Crespo-Biel, M.C.A. Stuart, D.N. Reinhoudt, J. Huskens, B.J. Ravoo, Proc. Natl. Acad. Sci. USA **104**, 6986–6991 (2007)
78. M.J.W. Ludden, M. Peter, D.N. Reinhoudt, J. Huskens, Small **2**, 1192–1202 (2006)
79. S. Onclin, J. Huskens, B.J. Ravoo, D.N. Reinhoudt, Small **1**, 852–857 (2005)
80. M.J.W. Ludden, A. Mulder, R. Tampe, D.N. Reinhoudt, J. Huskens, Angew. Chem. Int. Ed. **46**, 4104–4107 (2007)
81. M.L.W. Ludden, A. Mulder, K. Schulze, V. Subramaniam, R. Tampe, J. Huskens, Chem. Eur. J. **14**, 2044–2051 (2008)
82. H. Xu, R. Hong, T.X. Lu, O. Uzun, V.M. Rotello, J. Am. Chem. Soc. **128**, 3162–3163 (2006)

83. K. Kobayashi, N. Tonegawa, S. Fujii, J. Hikida, H. Nozoye, K. Tsutsui, Y. Wada, M. Chikira, M. Haga, Langmuir **24**, 13203–13211 (2008)
84. T. Hatano, A. Ikeda, T. Akiyama, S. Yamada, M. Sano, Y. Kanekiyo, S. Shinkai, J. Chem. Soc., Perkin Trans. 2 **5**, 909–912 (2000)
85. A. Langner, S.L. Tait, N. Lin, R. Chandrasekar, M. Ruben, K. Kern, Angew. Chem. Int. Ed. **47**, 8835–8838 (2008)
86. F. Tancini, D. Genovese, M. Montalti, L. Cristofolini, L. Nas, L. Prodi, E. Dalcanale, J. Am. Chem. Soc. **132**, 4781–4789 (2010)
87. M.E. Canas-Ventura, K. Ait-Mansour, P. Ruffieux, R. Rieger, K. Mullen, H. Brune, R. Fasel, ACS Nano **5**, 457–469 (2011)

Chapter 3
Expression of Sensitized Eu^{3+} Luminescence at a Multivalent Interface

3.1 Introduction

Self-assembly provides a unique paradigm to obtain complex and functional molecular architectures in a spontaneous process from small building blocks [2–9]. Self-assembly at surfaces is particularly rewarding, since the inherent immobilization allows characterization by single molecule techniques [10] and potential embedding in a device structure. It has only been recently recognized that surfaces, in particular those functionalized with molecular recognition units, the so-called molecular printboards, offer additional benefits regarding control over molecular orientation, footprint, stability of binding, and suppression of nonspecific interactions [11, 12]. These properties are given by the fact that molecules and complexes can be bound to such surfaces via multivalent interactions, which are governed by the principle of effective molarity [12]. When complexity is increased [13], here when going from one to more interaction motifs, new emerging properties can be expected. It has been shown before that the use of building blocks with orthogonal interaction motifs that self-assemble on molecular printboards can lead to the selective formation of one type of complex (from a large number of potential complexes) consisting of more than two different building blocks [14, 15], and control over supramolecular aggregation of receptor-functionalized vesicles [16]. Here we show, for the first time, the spontaneous formation of such a complex that signals its own correct assembly, by expressing sensitized lanthanide luminescence. The focus is on addressing the exact stoichiometry of the complex and its signaling properties.

The trivalent cations of several lanthanides and their complexes with organic ligands are known to exhibit characteristic emission line shapes, relatively long luminescence lifetimes, and a strong sensitivity towards quenching by high

Part of this chapter has been published in Ref. [1].

M. D. Yilmaz, *Orthogonal Supramolecular Interaction Motifs for Functional Monolayer Architectures*, Springer Theses, DOI: 10.1007/978-3-642-30257-2_3,

frequency, e.g. O–H, oscillators [17]. Because of their sharp, narrow absorption peaks, and low absorption coefficients, lanthanide ions are usually excited via energy transfer from an excited organic chromophore (the antenna or sensitizer), that has a much higher absorption coefficient [18]. The energy transfer process is strongly distance dependent and limits the practical lanthanide–antenna distance to <5 Å. [19].[1] Photophysical properties of lanthanide complexes in solution have been extensively studied. In a supramolecular example, an EDTA-based ligand with β-cyclodextrin (β-CD) binding sites showed sensitized Eu^{3+} emission by noncovalent capture of an organic sensitizer [20]. The immobilization and photophysical properties of lanthanide complexes on surfaces has not been investigated, except for some recent examples in which a Eu^{3+} complex was bound to a particle surface [21, 22], especially for sensor applications [23–25].

Here, we employ antenna–sensitized Eu^{3+} luminescence based on host–guest interactions on the molecular printboard, which allows qualitative and quantitative studies of the complexation of four different building blocks (Fig. 3.1a): an EDTA-based ligand for binding a Eu^{3+} ion and the receptor surface, a naphthalene-based antenna molecule with receptor-binding moieties and with a carboxylate group for coordination to the Eu^{3+} ion, the Eu^{3+} ion, and a β-CD monolayer which functions as the receptor surface. The EDTA ligand and the antenna molecule are equipped with adamantyl groups (Ad) for noncovalent anchoring to the β-CD monolayer. The β-CD monolayer is used to immobilize both the sensitizer and the Eu^{3+} complex, thus enforcing close proximity of the molecules and facilitating sensitized lanthanide luminescence owing to efficient energy transfer (Fig. 3.1b).

3.2 Results and Discussion

3.2.1 Synthesis

An EDTA–based ligand **1** for binding a Eu^{3+} ion and the receptor surface was synthesized as outlined in Scheme 3.1, and as follows. Amino ethyl triethylene glycol adamantyl ether was reacted with ethylenediaminetetraacetic dianhydride at room temperature in dry DMF using triethylamine as a base to give the bis (adamantyl tetraethylene glycol)—functionalized ethylenediaminetetraacetic acid **1**. The Eu(III) complex of compound **1** was prepared by adding a solution of $EuCl_3.6H_2O$ in water to a solution of **1**, adjusting the pH to 7 with overnight stirring at room temperature. A slight excess of **1** relative to Eu(III) (1.03:1) was used, ensuring quantitative complexation of the lanthanide ion. Compound **3** was

[1] The surface was consecutively imaged by fluorescence microscopy using two different filter sets: one set **B** allows UV excitation (300 nm $\leq \lambda_{ex} \leq$ 400 nm) and blue emission (410 nm $\leq \lambda_{em} \leq$ 510 nm) and another set **R** allows UV excitation and red emission (narrow band pass at 615 nm).

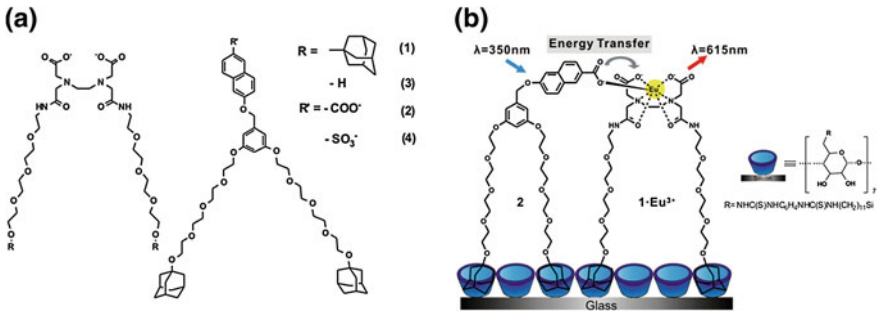

Fig. 3.1 **a** EDTA-based ligands with (**1**) and without (**3**) adamantyl (Ad) moieties, and carboxylate- (**2**) or sulfonate- (**4**) modified naphthalene derivatives with Ad groups. **b** Molecular structure of the target complex on a β-CD SAM schematically showing sensitized Eu^{3+} luminescence

designed and synthesized for a control experiment by adding ligand **1** into TFA/CH_2Cl_2 mixture, and the Eu(III) complex of compound **3** was prepared in a similar manner as **1.Eu**(III). A naphthalene-based antenna molecule **2** with receptor–binding moieties and with a carboxylate group for coordination to the Eu^{3+} ion was synthesized in three steps. In the first step, bromoethyl triethylene glycol adamantyl ether was reacted with 3, 5-dihydroxybenzyl alcohol under reflux in acetone using K_2CO_3 as a base to give compound **5**. The conversion of the hydroxyl group to the reactive bromide using PBr_3 in dry toluene gave compound **6**. In the last step, reaction between compound **6** and methyl-6-hydroxy-2-naphthoate using K_2CO_3 as a base gave the methyl ester of compound **2**. The cleavage of methyl ester to free carboxylic acid by NaOMe produced compound **2**. Compound **4** was synthesized as a reference compound by the reaction between compound **6** and 6-hydroxy-2-naphthalene sulfonic acid sodium salt using NaOMe as a base.

3.2.2 Complex Formation in Solution

Fluorescence spectroscopy measurements were performed to study the sensitized luminescence of the lanthanide complex **1.Eu**$^{3+}$ in solution in the absence and presence of antenna **2** (Fig. 3.2). The fluorescence spectrum of a 10 μM solution of **1.Eu**$^{3+}$ in H_2O did not show the characteristic Eu^{3+} emission at 615 nm, not even upon addition of an equimolar amount of **2,** excited at 350 nm while recording the luminescence spectrum between 350 and 650 nm. The broad band from 350 to 500 nm was attributed to the emission of **2**.

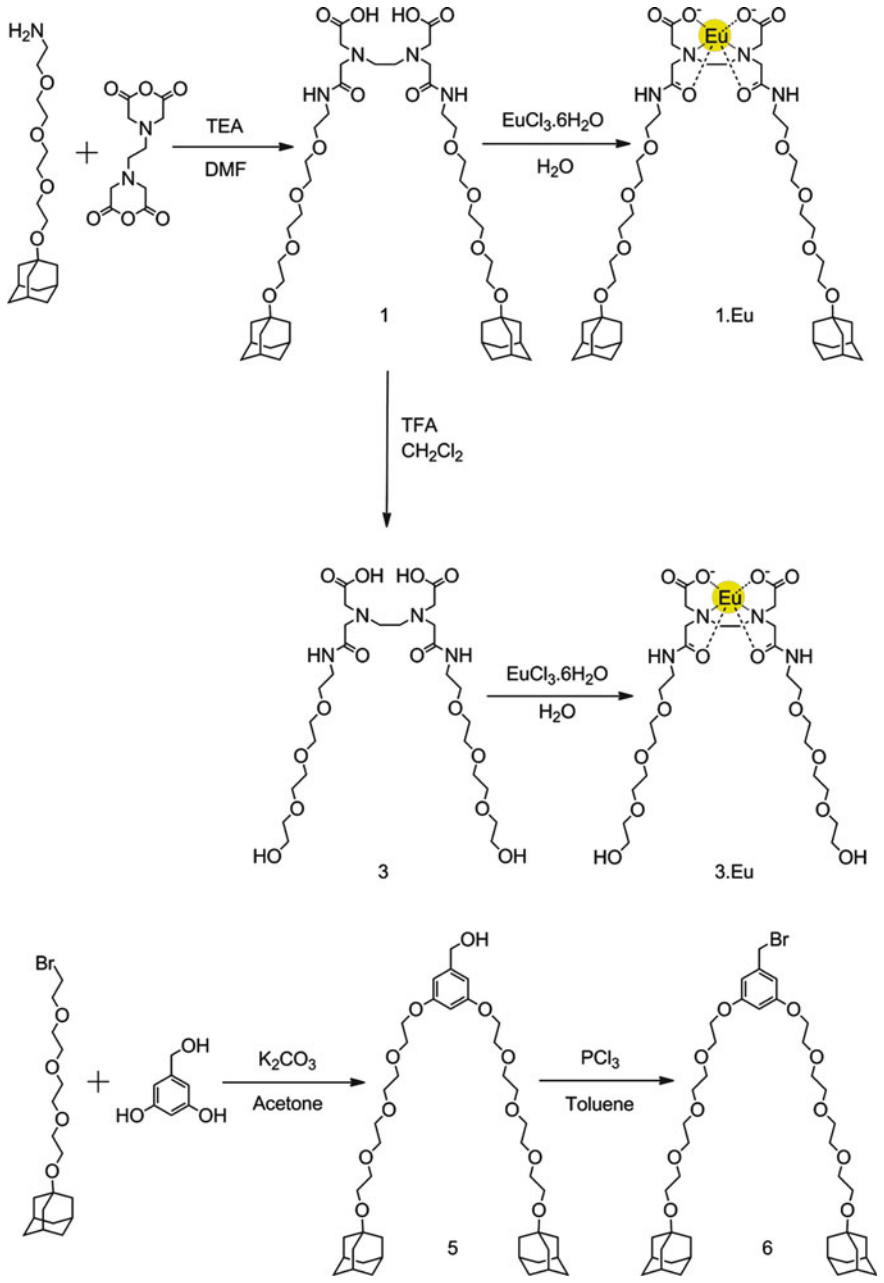

Scheme 3.1 Synthesis routes towards the building blocks used in this study

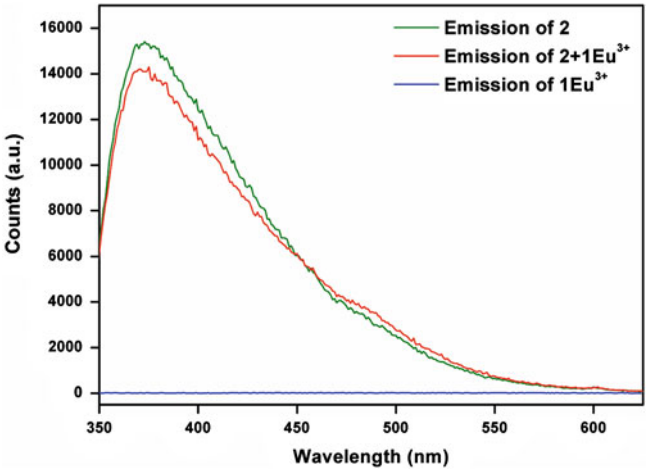

Fig. 3.2 Luminescence emission spectra of 10 μM solutions of **2**, **2** + **1.Eu**$^{3+}$ and **1.Eu**$^{3+}$ in H_2O excited at 350 nm

3.2.3 Complex Formation at the Molecular Printboard

Microcontact printing (μCP) onto β-CD monolayers, resulting in host–guest complex formation, was used to generate surface patterns of the complex on the receptor surface. Two methods were applied to immobilize the complex onto the surface (Scheme 3.2): (i) the surfaces were patterned by printing an equimolar ratio of **1.Eu**$^{3+}$ and **2** onto the β-CD SAM (**i**$_a$), followed by backfilling the non-printed area with **1.Eu**$^{3+}$, which was used as an internal reference (**i**$_b$); (ii) the surfaces were patterned by printing different ratios of **1** and **2** (**ii**$_a$), followed by solution immersion in aqueous $EuCl_3$ (**ii**$_b$). The solution immersion steps (**i**$_b$ and **ii**$_b$) were performed in the absence of β-CD in solution in order to prevent exchange of **2** by **1.Eu**$^{3+}$ (**i**$_b$) and desorption of **1** and **2** (**ii**$_b$) [19].

As an initial indication for energy transfer at the molecular printboard patterned using method **i**, red emission measured using filter **R** only appeared in the areas where both **1.Eu**$^{3+}$ and **2** are present (Fig. 3.3a), which demonstrates qualitatively the occurrence of sensitized Eu^{3+} luminescence. Local emission spectra were recorded to further characterize the patterned surface of **1.Eu**$^{3+}$ and **2** (Fig. 3.3b). The emission spectra were selectively collected from both the patterned and nonpatterned areas upon excitation in the UV (step **i**$_b$). From the nonpatterned areas, the observed Eu^{3+} emission is faint and can be attributed to inefficient direct UV excitation of **1.Eu**$^{3+}$ alone. However, a significantly higher intensity of Eu^{3+} emission is observed in the **1.Eu**$^{3+}$**/2** patterned area. Clearly the emission of Eu^{3+} is amplified in the area where energy transfer occurred between the naphthalene antenna and the lanthanide complex. Considering also the fact that twice as much **1.Eu**$^{3+}$ is expected to be present in the nonpatterned area with respect to the

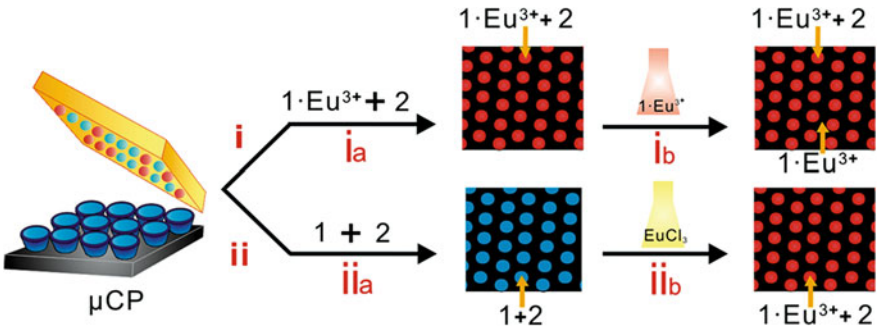

Scheme 3.2 Schematic representation of two immobilization procedures (**i** and **ii**) of the Ad ligands **1** and **2** without ($\mathbf{i}_a$, $\mathbf{ii}_a$) or with ($\mathbf{i}_b$, $\mathbf{ii}_b$) a solution step for backfilling with **1.Eu**$^{3+}$ in the nonprinted area ($\mathbf{i}_b$) or complexation of **1** with Eu^{3+} ($\mathbf{ii}_b$)

printed areas, comparing the intensities at 614 nm, an amplification of a factor of 54 is found between the patterned and nonpatterned areas.

In contrast, when using reference compound **4**, a naphthalene moiety bearing a sulfonate group instead of the carboxylate in **2,** no sensitized Eu^{3+} luminescence was observed (Fig. 3.4a, b). Since the sulfonate group is not basic enough to bind a lanthanide ion, this shows that direct coordination of the carboxylate of **2** to the Eu^{3+} center is involved to obtain efficient energy transfer. A similar observation was made in solution [20]. Moreover, when an EDTA-based complex without the adamantyl functionalities was used, **3.Eu**$^{3+}$, no sensitization of the Eu^{3+} luminescence was observed (Fig. 3.4c, d). This control experiment shows that direct coordination of the carboxylate is too weak to occur on its own, and has to be assisted by anchoring of both ligands on the receptor surface in order to have the high effective concentration [10, 11] promote the direct coordination, leading to efficient energy transfer.

To quantify the energy transfer efficiency between naphthalene and the lanthanide complexes, the naphthalene emission lifetimes were determined in the absence and presence of Eu^{3+}. To obtain sufficient signal, a stack of 6 glass slides coated on both sides with a monolayer of **2** or an equimolar mixture of **2** and **1**·Eu^{3+} was sampled at a time. The excitation source was a LED emitting at 282 nm at 1 MHz repetition rate. Emitted photons were detected in a narrow wavelength range around the naphthalene emission maximum at 370 nm (slit 10 nm). The emission lifetime from the naphthalene compound on the surface in the absence of the Eu^{3+} could be fitted with a double exponential with one strongly dominating component of $\tau_1 = 2.3$ ns (89 % relative amplitude) and a minor component of 7.0 ns (11 % relative amplitude) (Fig. 3.5). In the presence of **1.Eu**$^{3+}$, the lifetime of both components significantly dropped to 1.5 and 5.3 ns, respectively, while the relative amplitudes were preserved (91 and 9 %). From these lifetimes, we determined the dominant energy transfer efficiency to be 35 % for the major and 25 % for the minor component. To exclude any effect from

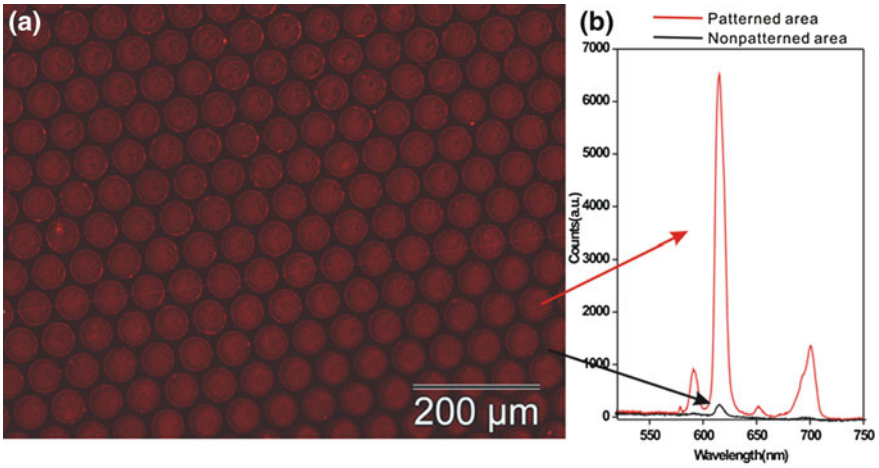

Fig. 3.3 **a** Fluorescence microscopy image (*left*, using filter **R**) of 50 μm dots on a *β*-CD monolayer obtained by μCP of an equimolar ratio of **1.Eu**$^{3+}$ and **2** for 30 min (step $\mathbf{i_a}$) and subsequent incubation in a solution with **1.Eu**$^{3+}$ for 30 min (step $\mathbf{i_b}$), **b** and local emission spectra from the patterned and nonpatterned areas (*right*), both illustrating the enhanced Eu^{3+} emission in the patterned areas

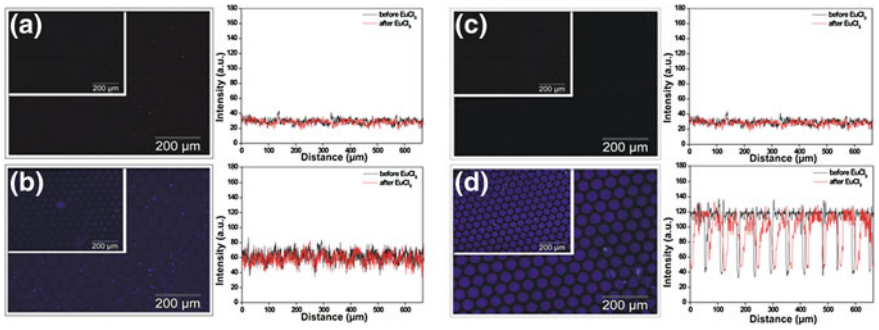

Fig. 3.4 Fluorescence microscopy images (884 × 666 μm) of 50 μm dots at a *β*-CD SAM made by μCP of a mixture of **1** and **4** for 30 min before (insets) and after (main images) immersion in a solution of $EuCl_3$ for 30 min, monitoring Eu^{3+} (**a**) and antenna (**b**) emission; a solution of **2** for 30 min, before (insets) and after (main images) immersion in a solution of **3.Eu**$^{3+}$ for 30 min, monitoring Eu^{3+} (**c**) and antenna (**d**) emission

possible energy transfer acceptor saturation due to the very long Eu^{3+} emission lifetime on the recorded decay characteristics, the experiment was repeated using a reduced excitation frequency of 100 kHz. The obtained results were identical to the ones obtained with 1 MHz excitation.

In order to study the stoichiometry of complexation between **2** and **1.Eu**$^{3+}$, a stepwise procedure (Scheme 3.2, method **ii**) was applied: *μ*CP of solution mixtures

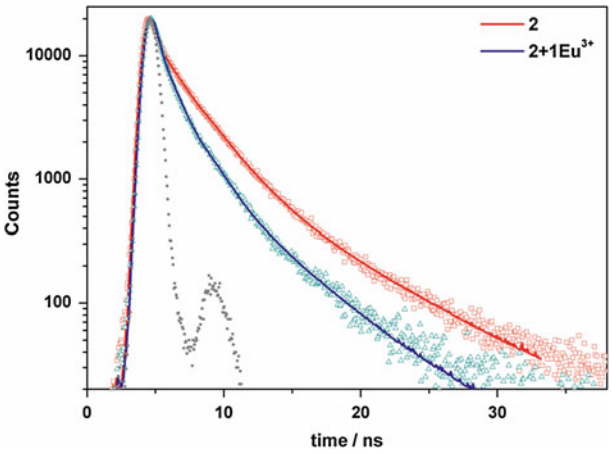

Fig. 3.5 Time-resolved fluorescence measurements of **2** alone and of **2** and **1.Eu**$^{3+}$ on a β -CD SAM excited at 282 nm with a 1 MHz LED. The 2.3 and 7.0 ns lifetime components were derived from fitting the decay curves of **2**

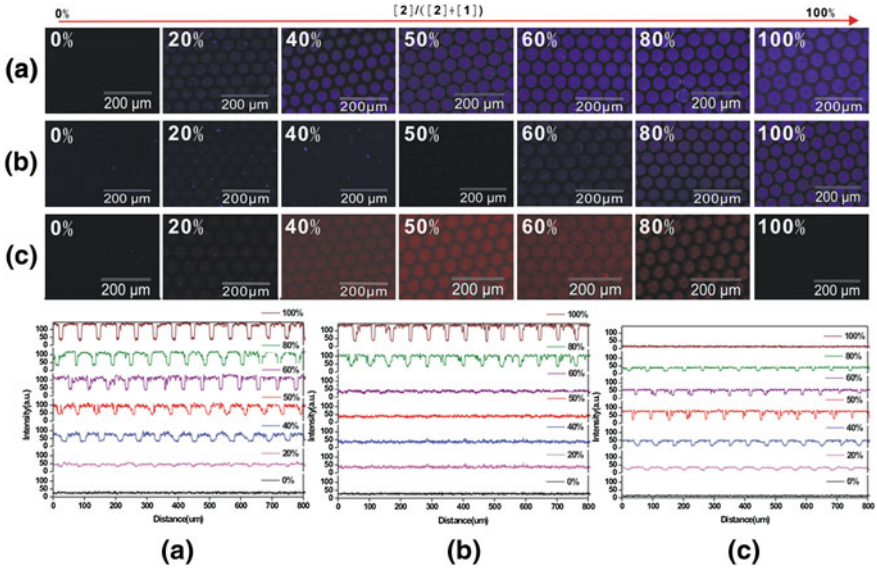

Fig. 3.6 Fluorescence microscopy images of 50 μm dots prepared on β-CD monolayers by μCP (30 min) of solution mixtures of different ratios of **1** and **2** (the concentration of **2** varying from 0, 20, 40, 50, 60, 80 and 100%) (**ii**$_a$), followed by rinsing with MilliQ water (**a**), and subsequently immersed in a solution of $EuCl_3$ for 30 min (**ii**$_b$) (**b**, **c**), monitoring antenna (**a**, **b**; **B** filter) and Eu^{3+} emission (**c**; **R** filter). The percentages of antenna **2** in the mixture of **1** and **2** are given in the images. The intensity profiles (*bottom*) are also shown before (**a**) and after (**b**, **c**) $EuCl_3$ immersion

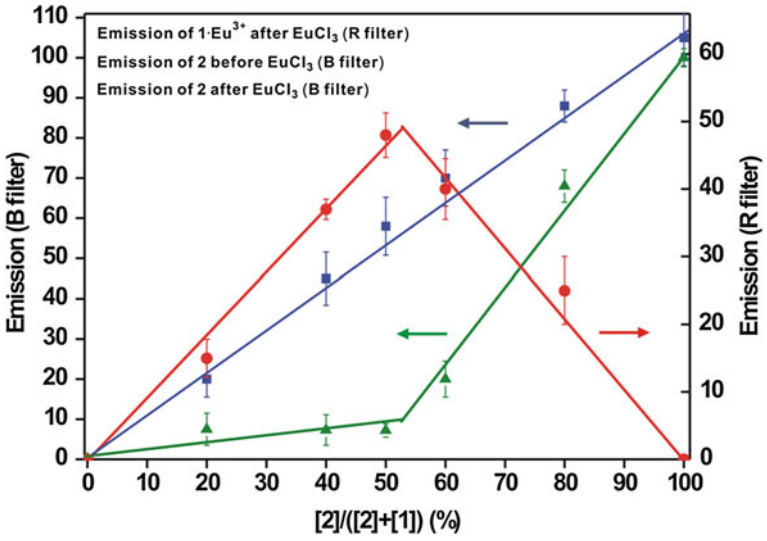

Fig. 3.7 Fluorescence intensity of **2** before (*blue*, *squares*) and after (*green*, *triangles*) immersion in a $EuCl_3$ solution, and of Eu^{3+} emission (*red*, *circles*) after the solution step, for patterns printed from solutions with varying ratios of **2** and **1**. *Lines* are presented for fits of the data points from 0–100 % (*blue line*) and from 0–50 % and 50–100 % separately (*green* and *red lines*). The error bars represent a single standard deviation

of different molar ratios of **1** and **2** was used to generate patterns on the β-CD monolayer. Directly after printing (step $\mathbf{ii_a}$), the surface was imaged with fluorescence microscopy, followed by immersion in a $EuCl_3$ solution for 30 min (step $\mathbf{ii_b}$) and re-imaging (Fig. 3.6). The fluorescence intensities of the surface antenna and Eu^{3+} emission were plotted as a function of the molar fraction of antenna **2** (Fig. 3.7). Since the printboard ensures that the total immobilized ligand concentration (**1** + **2**) remains constant, this plot fulfills the requirements for a Job plot.

3.3 Conclusions

This work clearly demonstrates that **1.Eu**$^{3+}$ and the antenna **2** form a 1:1 coordination pair on the β-CD SAM. The formation of the target complex is directly indicated by the occurrence of sensitized luminescence. This surface assisted luminescence amplification has potential for developing optical devices or as a sensing platform for biologically relevant anions [26]. The system as a whole represents an example of functional expression, emerging from the combined system of all necessary components [27]. The high specificity of the complex formation is in part attributed to the multivalency of the receptor surface which is here translated in a higher level multivalent interface of Eu complexes with vacant

coordination sites and antenna molecules with the complementary carboxylate groups. Another crucial factor in steering the system into the direction of the target complex is to encode the necessary information into all individual building blocks. As can be seen here, this information can be limited while still complex molecular architectures can be achieved.

3.4 Experimental Section

3.4.1 General Procedures

All reactions involving air- or moisture-sensitive reagents or intermediates were performed under an inert atmosphere of argon in glassware. Unless otherwise noted, solvents and reagents were commercially available, reagent grade and used without further purification. β-CD heptamine, amino ethyl triethylene glycol adamantyl ether, and bromo triethylene glycol ethyl adamantyl ether were synthesized as described before [12, 28]. Thin layer chromatography was performed on aluminum sheets precoated with silica gel 60 F254 (Merck). Column chromatography was performed using silica gel (SiO_2, Merck, 0.040–0.063 mm, 230–240 mesh). NMR spectra were recorded on Varian AC300 spectrometer in the indicated solvent. Chemical shifts are reported in parts per million (ppm) downfield from $(CH_3)_4Si$ (TMS) as internal standard. Coupling constants are reported in hertz (Hz). Spectral splitting patterns are designated as follows: s, singlet; d, doublet; t, triplet; q, quartet; m, multiplet. ESP–MS spectra were recorded with a WATERS–LCT spectrometer.

3.4.2 EDTA-Based Tetraethylene Glycol Adamantyl Ether Dimer 1

A solution of amino ethyl triethylene glycol adamantyl ether (511.2 mg, 1.56 mmol) and Et_3N (3 ml) was added dropwise to a solution of ethylenediaminetetraacetic dianhydride (200 mg, 0.78 mmol) in DMF at 0 °C. The reaction mixture was stirred for 2 days at room temperature. After evaporation of the solvent, the residue was dissolved in water and the pH was adjusted to 7. Water was removed under reduced pressure and methanol was added to separate insoluble salts. The solvent was removed by rotary evaporator after filtration, and the residue was washed several times with diethyl ether. The product was obtained as a colorless oil, yield 80 %.

^{1}H NMR (300 MHz, CD_3OD) δ 3.70–3.55 (m, 28H), 3.35–3.29 (m, 8H), 3.19–3.13 (m, 4H), 2.71–2.67 (m, 4H), 2.20–2.15 (m, 6H), 1.80–1.79 (m, 12H), 1.75–1.63 (m, 12H). ^{13}C NMR (75 MHz, CD_3OD) δ 174.9, 170.3, 71.0, 69.5, 68.7, 57.6, 56.6, 51.2, 39.8, 34.8, 29.3. MS (ESP) calculated for $C_{46}H_{78}N_4O_{14}$ (M + H) 912.1; found 912.0.

3.4.3 Eu^{3+} Complex of 1

The Eu(III) complex of compound **1** was prepared by adding a solution of $EuCl_3.6H_2O$ in water to a solution of **1**, adjusting the pH to 7 with overnight stirring at room temperature. A slight excess of **1** relative to Eu(III) (1.03:1) was used, ensuring quantitative complexation of the lanthanide ion.

MS (ESP) calculated for $C_{46}H_{76}EuN_4O_{14}$ (M) 1061.0; found 1061.2.

3.4.4 1-Naphthoic Acid-6-(3, 5-Di(Tetraethylene Glycol Adamantyl Ether) Benzyl Ether 2

A suspension of **6** (340 mg, 0.413 mmol), methyl-6-hydroxy-2-naphthoate (83.44 mg, 0.413 mmol), dried potassium carbonate (57.04 mg, 0.5 mmol), and 18-crown-6 (10.5 mg, 0.04 mmol) in acetone (50 mL) was refluxed overnight. The solvent was evaporated and the residue was partitioned between water (50 mL) and diethyl ether (50 mL). The aqueous layer was extracted with diethyl ether (3×25 mL) and the combined extracts were dried over $MgSO_4$. The solvent was evaporated and the residue was purified by column chromatography (EtOAc, eluent) to give the methyl ester of **2** as a colorless oil (273.2 mg, 70 %).

^{1}H NMR (300 MHz, $CDCl_3$) δ 8.49 (s, 1H), 7.98 (d, $J = 9$ Hz, 1H), 7.81 (d, $J = 9$ Hz, 1H), 7.70 (d, $J = 9$ Hz, 1H), 7.23 (d, $J = 9$ Hz, 1H), 7.17 (s, 1H), 6.62 (s, 2H), 6.44 (s, 1H), 5.09 (s, 2H), 4.09 (t, $J = 4.8$ Hz, 4H), 3.93 (s, 3H), 3.81 (t, $J = 4.8$ Hz, 4H), 3.72–3.51 (m, 24H), 2.09–2.06 (m, 6H), 1.75–1.70 (m, 12H), 1.65–1.52 (m, 12H). ^{13}C NMR (75 MHz, $CDCl_3$) δ 167.5, 160.4, 158.7, 138.9, 137.2, 131.1, 130.9, 128.2, 127.1, 126.1, 125.5, 120.0, 107.3, 106.2, 101.3, 72.3, 71.4, 71.3, 71.0, 70.8, 70.2, 69.8, 67.7, 60.5, 59.3, 52.3, 47.7, 36.6, 30.7. MS (ESP) calculated for $C_{55}H_{76}O_{13}$ (M) 945.1; found 945.4.

A solution of the methyl ester of **2** in THF (20 ml) was slowly added to a solution of excess NaOMe (freshly prepared) in MeOH (20 ml). The mixture was refluxed overnight, the solvent was removed, and the residue was acidified with HCl (aq) and extracted with EtOAc. The evaporation of solvent gave compound **2** (quantitative yield)

^{1}H NMR (300 MHz, $CDCl_3$) δ 8.54 (s, 1H), 8.00 (d, $J = 9$ Hz, 1H), 7.80 (d, $J = 9$ Hz, 1H), 7.68 (d, $J = 9$ Hz, 1H), 7.21 (d, $J = 9$ Hz, 1H), 7.14 (s, 1H), 6.59 (s, 2H), 6.43 (s, 1H), 5.04 (s, 2H), 4.07 (t, $J = 4.8$ Hz, 4H), 3.80 (t, $J = 4.8$ Hz, 4H), 3.70–3.52 (m, 24H), 2.13–2.04 (m, 6H), 1.74–1.69 (m, 12H), 1.65–1.50 (m, 12H). ^{13}C NMR (75 MHz, $CDCl_3$) δ 170.9, 160.3, 158.9, 138.9, 137.5, 131.7, 131.2, 128.1, 127.1, 126.3, 125.0, 120.0, 107.3, 106.2, 101.3, 72.5, 71.4, 71.2, 70.9, 70.8, 70.1, 69.8, 67.7, 60.5, 59.3, 41.6, 36.6, 30.7. MS (ESP) calculated for $C_{54}H_{74}O_{13}$ (M) 931.1; found 931.4.

3.4.5 EDTA-Based Tetraethylene Glycol Dimer 3

A solution of compound **1** (0.10 g, 0.14 mmol) in 50 % trifluoroacetic acid-CH_2Cl_2 (10 mL) was stirred overnight at room temperature. Solvents were removed under reduced pressure followed by the addition and then evaporation of CH_2Cl_2 (3×10 mL) and finally diethyl ether (10 mL). The residue was taken up in H_2O, filtered, and lyophilized to give **3** (quantitative yield).

^{1}H NMR (300 MHz, $CDCl_3$) δ 3.81–3.40 (m, 32H), 3.32–3.27 (m, 4H), 3.12–3.08 (m, 8H). MS (ESP) calculated for $C_{43}H_{68}O_{11}$ (M + H) 761.5; found 761.4.

3.4.6 Eu^{3+} Complex of 3

The Eu(III) complex of **3** was synthesized similar to **1.Eu**$^{3+}$.

MS (ESP) calculated for $C_{26}H_{48}EuN_4O_{14}$ (M + H) 793.64; found 793.2.

3.4.7 1-Naphthalene sulfonic acid-6-(3, 5-di(tetraethylene glycol adamantyl ether) benzyl ether 4

Na (46.6 mg, 2.02 mmol) was dissolved in MeOH, previously cooled in an ice-bath. 6-Hydroxy-2-naphthalene sulfonic acid sodium salt (0.498 g, 2.02 mmol) was added and the mixture was stirred and heated to 60 °C to dissolve any precipitated material. Compound **6** was added with small portions over a period of 15 min. The mixture was refluxed overnight, cooled to room temperature, and the solvent was evaporated. The residue was dissolved in chloroform and filtered. The solvent was evaporated and washed several times with diethylether. The product was obtained as a white solid (0.6 g, 30 %).

^{1}H NMR (300 MHz, $CDCl_3$) δ 8.29 (s, 1H), 7.81 (d, J = 9 Hz, 1H), 7.51 (d, J = 9 Hz, 1H), 7.31 (d, J = 9 Hz, 1H), 7.01 (d, J = 9 Hz, 1H), 6.91 (s, 1H), 6.57 (s, 2H), 6.43 (s, 1H), 4.94 (s, 2H), 4.07 (m, 4H), 3.76 (m, 4H), 3.70–3.52 (m, 24H), 2.12–2.01 (m, 6H), 1.72–1.64 (m, 12H), 1.61–1.46 (m, 12H). MS (ESP) calculated for $C_{53}H_{73}NaO_{14}S$ (M + H–Na) 967.19; found 967.5.

3.4.8 3, 5-Bis(Tetraethylene Glycol Adamantyl Ether) Benzyl Alcohol 5

A suspension of bromoethyl triethylene glycol adamantyl ether (1.5 g, 3.83 mmol), 3, 5-dihydroxy benzyl alcohol (268.5 mg, 1.916 mmol), dried potassium carbonate (529.76 mg, 3.83 mmol), and 18-crown-6 (0.11 g,

0.42 mmol) in acetone (50 mL) was refluxed for 72 h. The solvent was evaporated and the residue was partitioned between water (50 mL) and diethyl ether (50 mL). The aqueous layer was extracted with diethyl ether (3×25 mL) and the combined extracts were dried over $MgSO_4$. The solvent was evaporated and the residue was purified by column chromatography (EtOAc, eluent) to give **5** as a colorless oil (874.8 mg, 60 %).

^{1}H NMR (300 MHz, $CDCl_3$) δ 6.50 (s, 2H), 6.35 (s, 1H), 4.55 (s, 2H), 4.06 (t, $J = 4.8$ Hz, 4H), 3.79 (t, $J = 4.8$ Hz, 4H), 3.69–3.53 (m, 24H), 2.12–2.08 (m, 6H), 1.72–1.68 (m, 12H), 1.64–1.50 (m, 12H). ^{13}C NMR (75 MHz, $CDCl_3$) δ 160.2, 143.7, 105.7, 101.4, 72.4, 71.4, 71.3, 71.0, 70.9, 69.9, 67.7, 65.3, 60.5, 59.3, 41.6, 36.6, 30.6. MS (ESP) calculated for $C_{43}H_{68}O_{11}$ (M + H) 761.5; found 761.4.

3.4.9 3, 5-Bis(Tetraethylene Glycol Adamantyl Ether) Benzyl Bromide 6

A solution of phosphorus tribromide (78.65 mg, 0.29 mmol) in toluene (5 mL) was added dropwise to a cooled (0 °C) solution of **5** (562.0 mg, 0.73 mmol) in toluene (50 mL). The mixture was stirred for 1 h at room temperature. The solvent was removed under reduced pressure and the residue was partitioned between dichloromethane (100 mL) and water (100 mL). The organic layer was washed with water (3×50 mL) and brine (1×50 mL) and dried over $MgSO_4$. The solvent was removed under reduced pressure and the residue was purified by column chromatography (EtOAc, eluent) to give **6** as a colorless oil (456 mg, 75%).

^{1}H NMR (300 MHz, $CDCl_3$) δ 6.52 (s, 2H), 6.40 (s, 1H), 4.36 (s, 2H), 4.07 (t, $J = 4.8$ Hz, 4H), 3.81 (t, $J = 4.8$ Hz, 4H), 3.73–3.50 (m, 24H), 2.15–2.10 (m, 6H), 1.76–1.71 (m, 12H), 1.67–1.53 (m, 12H). ^{13}C NMR (75 MHz, $CDCl_3$) δ 160.2, 139.8, 128.4, 108.1, 101.9, 72.4, 71.6, 71.5, 71.4, 71.3, 71.0, 70.8, 69.8, 67.7, 59.4, 41.6, 36.6, 30.7. MS (ESP) calculated for $C_{43}H_{67}BrO_{10}$ (M) 823.8; found 823.2.

3.4.10 Substrate and Monolayer Preparation

Microscope glass slides were used for β–cyclodextrin (β-CD) monolayer preparation. The substrates were cleaned with piranha solution for 15 min (concentrated H_2SO_4 and 33 % aqueous H_2O_2 in a 3:1 ratio; Caution: piranha should be handled carefully) and rinsed with MilliQ. After drying in a nitrogen stream, the substrates were used immediately for silanized monolayer formation. The substrates were enclosed in a low-vacuum desiccator with 0.1 ml TPEDA, continually pumping for 5 min to create a vapor phase of TPEDA. After overnight incubation, the slides were rinsed with ethanol and dichloromethane to remove any excess of silanes and

subsequently dried in a nitrogen stream. The attachment of 1, 4-phenylene diisothiocyanate was made in a 20 mM solution in toluene at 60 °C during 2 h. Samples were thoroughly rinsed with toluene and dried in a nitrogen flow. The β-CD layer attachment was made during 2 h in an aqueous 0.1 mM β-cyclodextrin-heptaamine solution (pH $\sim$ 7) at 60 °C. Samples were thoroughly rinsed with water and dried in a nitrogen flow.

3.4.11 Microcontact Printing

Patterned silicon substrates were made by photolithography followed by reactive ion etching (RIE) or e-beam lithography. They consisted of gratings of 50 μm dots at 70 μm period with the height of 1 μm. PDMS stamps were prepared by casting a 10:1 (v/v) mixture of poly(dimethylsiloxane) (PDMS) prepolymer and curing agent (Sylgard 184, Dow Corning) against a silicon master. After overnight curing at 60 °C, the stamps were oxidized by oxygen plasma for 1 min and subsequently inked by dropping aqueous adsorbate solution onto the stamp. Before printing, the stamps were blown dried in a stream of nitrogen. The stamps were brought into conformal contact with the substrate for 30 min. The stamps were changed for each new print and the same inking procedure was used. After stamp removal, the printed substrates were rinsed with copious amounts of water, blown dry with nitrogen, and imaged with fluorescence microscopy.

3.4.12 Printing of 1 and 2 (or 4), Followed by $EuCl_3$ Immersion

The β-CD SAM substrate was printed for 30 min with a stamp inked with an equimolar ratio of 1 and 2 (or 4) (2 mM each) in saturated β-CD in a 3:1 mixture of EtOH/water, followed by rinsing with water and drying in a stream of nitrogen. The printed substrate was immersed in a 4 mM aqueous solution of $EuCl_3$ for 30 min, followed by rinsing, and drying in a stream of nitrogen.

3.4.13 Printing of 2, Followed by 1.Eu^{3+} (or 3.Eu^{3+}) Immersion

The β-CD SAM substrate was printed for 30 min with a stamp inked with a solution of 2 in saturated β-CD in a 3:1 mixture of EtOH/water, followed by rinsing with water and drying in a stream of nitrogen. The printed substrate was immersed in a 2 mM aqueous solution of **1.Eu**$^{3+}$ (or **3.Eu**$^{3+}$) for 30 min, followed by rinsing, and drying in a stream of nitrogen.

3.4.14 Printing of Different Ratios of 1 and 2, Followed by $EuCl_3$ Immersion

The β-CD SAM substrate was printed for 30 min with a stamp inked with different molar ratio of 2 and 1 varying from 0:100, 20:80, 40:60, 50:50, 60:40, 80:20, and 100:0% in saturated β-CD in a 3:1 mixture of EtOH/water, followed by rinsing with water and drying in a stream of nitrogen. The printed substrate was immersed in a 4 mM aqueous solution of $EuCl_3$ for 30 min, followed by rinsing, and drying in a stream of nitrogen.

3.4.15 Time-Resolved Fluorescence Measurements

Two sets of samples were prepared with or without **1.Eu**$^{3+}$ present. The first sample was printed with a flat stamp inked with 2 mM of 2 for 30 min onto a β-CD SAM with saturated β-CD in 3:1 EtOH/water. The same procedure was used to prepare substrates with an equimolar ratio of 2 and **1.Eu**$^{3+}$ (2 mM each). In order to enhance the total emission intensity, multiple slides were used in a cuvette during the measurement in air (6 double side printed slides in total). The samples were positioned at 45° orientation relative to the excitation light and the detector. The decay curves at 370 nm for the donor alone (2) and in the presence of the acceptor (**1.Eu**$^{3+}$) were measured upon excitation at 282 nm.

3.4.16 Fluorescence Microscopy

Fluorescence microscope images were taken using an Olympus inverted research microscope IX71 equipped with a mercury burner U-RFL-T as light source and a digital Olympus DR70 camera for image acquisition. UV excitation ($300\ \text{nm} \leq \lambda_{ex} \leq 400\ \text{nm}$) and blue emission ($410\ \text{nm} \leq \lambda_{em} \leq 510\ \text{nm}$) was filtered using a Dapi Olympus filter cube. UV excitation ($300\ \text{nm} \leq \lambda_{ex} \leq 400\ \text{nm}$) and red emission (narrow band pass at 615 nm) was filtered using a Olympus filter cube. All fluorescence microscopy images were acquired in air.

3.4.17 Fluorescence Spectral Microscopy

To record local emission spectra, a custom built microscopy setup capable of spectral imaging was used. The sample was illuminated using a mercury lamp and a standard filter cube for UV excitation (excitation 300 to 400 nm, detection

>400 nm) via a 100X objective (1.3 NA, Olympus). The local emission was collected by the same objective. The emitted light was imaged via a pinhole and a prism spectrometer onto a cooled CCD camera (Newton EMCCD, Andor). Wavelength calibration was achieved using a calibrated light source (Cal-2000 Mercury Argon Calibration source, Ocean Optics, USA).

3.4.18 Fluorescence Lifetime Spectrophotometry

Fluorescence lifetimes were determined using a spectrophotometer (FluoroMax4, Horiba Jobin–Yvon), equipped with a TCSPC extension and a pulsed 282 nm NanoLED for excitation (all Horiba Jobin–Yvon). The recorded data was analyzed using the DAS6 software package of Horiba Jobin–Yvon.

Acknowledgment The major part of the work presented in this chapter was performed in collaboration with Shu-Han Hsu. Christian Blum is acknowledged for performing the local fluorescence emission spectra and lifetime measurements.

References

1. S.-H. Hsu, M.D. Yilmaz, C. Blum, V. Subramaniam, D.N. Reinhoudt, A.H. Velders, J. Huskens, J. Am. Chem. Soc. **131**, 12567–12569 (2009)
2. D.N. Reinhoudt, M. Crego-Calama, Science **295**, 2403–2407 (2002)
3. V.E. Campbell, J.R. Nitschke, Synlett **2008**, 3077–3090 (2008)
4. C.A.M. Bradley, J. Holliday, Angew. Chem. Int. Ed. **40**, 2022–2043 (2001)
5. J.-M. Lehn, Chem. Soc. Rev. **36**, 151–160 (2007)
6. J.-M. Lehn, Proc. Natl. Acad. Sci. USA **99**, 4763–4768 (2002)
7. G.M. Whitesides, R.F. Ismagilov, Science **284**, 89–92 (1999)
8. R.F. Ludlow, S. Otto, Chem. Soc. Rev. **37**, 101–108 (2008)
9. B.C. Gibb, Nat. Chem. **1**, 17–18 (2009)
10. A. Langner, S.L. Tait, N. Lin, C. Rajadurai, M. Ruben, K. Kern, Proc. Natl. Acad. Sci. USA, 104, 17927–17930 (2007)
11. A. Mulder, J. Huskens, D.N. Reinhoudt, Org. Biomol. Chem. **2**, 3409–3424 (2004)
12. M.J.W. Ludden, D.N. Reinhoudt, J. Huskens, Chem. Soc. Rev. **35**, 1122–1134 (2006)
13. M. Eigen, *The Hypercycle: A Principle of Natural Self Organization* (Springer-Verlag, Berlin, 1979)
14. M.L.W. Ludden, A. Mulder, K. Schulze, V. Subramaniam, R. Tampe, J. Huskens, Chem. Eur. J. **14**, 2044–2051 (2008)
15. O. Crespo-Biel, C.W. Lim, B.J. Ravoo, D.N. Reinhoudt, J. Huskens, J. Am. Chem. Soc. **128**, 17024–17032 (2006)
16. C.W. Lim, O. Crespo-Biel, M.C.A. Stuart, D.N. Reinhoudt, J. Huskens, B.J. Ravoo, Proc. Natl. Acad. Sci. USA **104**, 6986–6991 (2007)
17. M.F. Hazenkamp, G. Blasse, N. Sabbatini, J. Phys. Chem. **95**, 783–787 (1991)
18. G.E. Buonocore, H. Li, B. Marciniak, Coord. Chem. Rev. **99**, 55–87 (1990)
19. L. Dexter, J. Chem. Phys. **21**, 836–850 (1953)
20. J.J. Michels, J. Huskens, D.N. Reinhoudt, J. Am. Chem. Soc. **124**, 2056–2064 (2002)

21. E. Delgado-Pinar, J.C. Frias, L.J. Jimenez-Borreguero, M.T. Albelda, J. Alarcon, E. Garcia-Espana, Chem. Commun. **28**(32), 3392–3394 (2007)
22. D.J. Lewis, T.M. Day, J.V. MacPherson, Z. Pikramenou, Chem. Commun. **13**, 1433–1435 (2006)
23. J. Massue, S.J. Quinn, T. Gunnlaugsson, J. Am. Chem. Soc. **130**, 6900–6901 (2008)
24. K.L. Ai, B.H. Zhang, L.H. Lu, Angew. Chem. Int. Ed. **48**, 304–308 (2009)
25. B.I. Ipe, K. Yoosaf, K.G. Thomas, J. Am. Chem. Soc. **128**, 1907–1913 (2006)
26. J.P. Leonard, C.M.G. dos Santos, S.E. Plush, T. McCabe, T. Gunnlaugsson, Chem. Commun. **2**(2), 129–131 (2007)
27. P. Luisi, Fundam. Chem. **4**, 1572–8463 (2002)
28. T. Auletta, B. Dordi, A. Mulder, A. Sartori, S. Onclin, C.M. Bruinink, M. Peter, C.A. Nijhuis, H. Beijleveld, H. Schonherr, G.J. Vancso, A. Casnati, R. Ungaro, B.J. Ravoo, J. Huskens, D.N. Reinhoudt, Angew. Chem. Int. Ed. **43**, 369–373 (2004)

Chapter 4
Ratiometric Fluorescent Detection of an Anthrax Biomarker at Molecular Printboards

A novel surface-assisted fluorescent sensing system has been developed for the ratiometric detection of an anthrax biomarker (dipicolinic acid, DPA) on a molecular printboard. The system affords a nanomolar sensitivity and high selectivity toward DPA.

4.1 Introduction

Anthrax is an acute disease, concurrently a potential biological warfare agent caused by *Bacillus Anthracis.* The accurate, rapid, sensitive, and selective detection of *Bacillus* spores plays a vital role in order to prevent a biological attack or outbreak of disease [2–10]. Bacterial spores contain a main core cell which is enclosed by protective layers. As a major component of these protective layers, bacterial spores contain up to 1 M dipicolinic acid (DPA), accounting for 5–15 % of the dry mass of the bacterial spore [11–16]. Hence, DPA is a convenient biomarker for these spores.

In recent years a number of biological and chemical detection methods for *Bacillus Anthracis* spores have been investigated. Biological methods are based on polymerase chain reactions [17, 18] and immunoassays [19, 20]. Important chemical methods employ vibrational spectroscopy (FT-IR, Raman and SERS)[21–23] and photoluminescence [24]. Among them, lanthanide (Ln^{3+})-based luminescent detection of DPA has been most promising owing to the unique photophysical properties of Ln^{3+}-DPA chelates including their bright luminescence upon sensitization by DPA, the long luminescence lifetimes compared to free Ln^{3+}, and the concomitantly high luminescence enhancement ratio upon coordination of DPA to the Ln^{3+} center [25–31]. Besides the use of DPA itself as a

Part of this chapter has been published in Deniz Yilmaz et al. [1].

M. D. Yilmaz, *Orthogonal Supramolecular Interaction Motifs for Functional Monolayer Architectures*, Springer Theses, DOI: 10.1007/978-3-642-30257-2_4,

sensitizer, ratiometric fluorescent detection of anthrax spores can be achieved through the displacement of a different sensitizer by DPA.

Molecular recognition processes at monolayers on surfaces offer advantages compared to solution-based sensing, such as a fast response time, minimization of analyte sorption time to the receptor, and real-time and real-space measurements [32, 33]. Glass is an appropriate substrate for fluorescence detection of chemical species owing to its transparency, inertness to light, and easy modification with a monolayer of organic adsorbates [34, 35]. Microarrays on glass allow for rapid, simultaneous, and multiple analyte sensing on glass slides. Previous studies have indicated that fluorescent monolayers on glass can be employed in the fabrication of microarrays via soft lithography such as microcontact printing (μCP) which is an efficient and low-cost lithographic technique to create patterned surfaces. Using μCP on glass as a substrate enables the use of fluorescence microscopy for direct visualization of the created fluorescent patterns [36].

Ratiometric detection of chemical species, i.e. the recording of the relative fluorescence intensities at two different wavelengths, has attracted interest owing to an increased accuracy and reproducibility of analyte detection compared to measurements performed at a single wavelength [37, 38]. Strong ratiometric fluorescence responses have been achieved in solid films and fluorescent monolayers as well as in solution [39].

4.2 Results and Discussion

In the current study we present a novel platform for the ratiometric detection of the *Bacillus Anthracis* biomarker DPA with high sensitivity and selectivity on a supramolecular monolayer surface. We employ so-called molecular printboards [40]. which are monolayers of *β*-cyclodextrin (*β*-CD) on a surface to which building blocks are attached in a noncovalent fashion that allow ratiometric DPA sensing. To the best of our knowledge, this system constitutes the first lanthanide-based surface receptor system for the detection of DPA, as well as the first example of ratiometric DPA detection at a surface.

In Chap. 3 we have demonstrated the surface-assisted sensitized luminescence of Eu^{3+} on a molecular printboard [41]. Here, we fabricated these luminescent patterns for the ratiometric detection of DPA on a receptor surface, as outlined in Scheme 4.1. Two building blocks have been used in this study: an EDTA-based ligand (**1**) for binding Eu^{3+}, and a naphthalene-based antenna (**2**) for coordination to Eu^{3+} via the carboxylate moiety. Both building blocks have adamantyl groups for immobilization onto the *β*-CD monolayer. To fabricate patterned sensing surfaces, a stepwise procedure was followed. Briefly, in the first step, an equimolar mixture of **1** and **2** was printed onto the *β*-CD monolayer by μCP to generate surface patterns of the ligand pairs. After thorough rinsing with water and drying, the patterned surface was imaged by fluorescence microscopy using filter **B** ($300 < \lambda_{exc} < 400$ nm, $410 < \lambda_{em} < 510$) and **R** ($300 < \lambda_{exc} < 400$ nm,

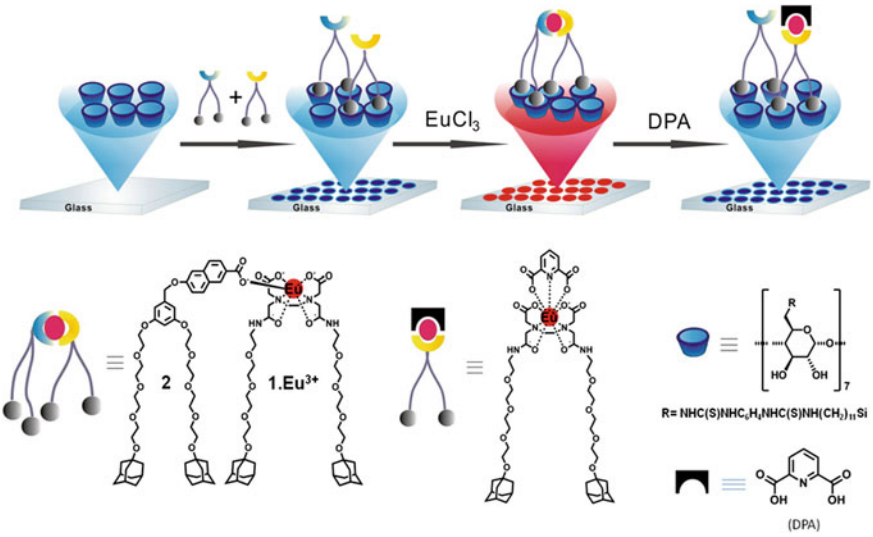

Scheme 4.1 Schematic illustration of the build-up of the supramolecular sensing surface system and the detection of the anthrax biomarker DPA (*top*), and compounds used in this study (*bottom*)

$\lambda_{em} = 615$ nm). As such, filter **B** collects the naphthalene emission of **2**, while filter **R** only collects the Eu^{3+} emission of **1.Eu**$^{3+}$, both with excellent selectivity. Subsequently, the glass slides were immersed in a $EuCl_3$ solution for 30 min to convert **1** into the **1.Eu**$^{3+}$ complex, followed by fluorescence imaging. Subsequently, substrates were incubated into aqueous solutions of DPA with different concentrations (pH = 6.5) for 10 min with continuous stirring. After rinsing and drying, the substrates were again imaged. It is important to note that direct DPA excitation at 270 nm is inhibited by the narrow band excitation filter at 350 nm.

Fluorescence images for all steps are shown in Fig. 4.1. In the first step, only the blue naphthalene emission was observed using filter B and no Eu^{3+} emission was seen by filter R. After incubation in the $EuCl_3$ solution, the red emission of Eu^{3+} appeared (filter R) and the blue emission of naphthalene decreased (filter B) due to energy transfer from the Eu-coordinated naphthalene moiety of **2** to the Eu^{3+} center of **1**.Eu^{3+}, as studied before [41]. In the last step, owing to the displacement of the naphthalene moiety by DPA, the blue emission was recovered and the red emission disappeared.

The fluorescence images clearly indicate that the recovery of the naphthalene emission is practically complete in the presence of only 200 nm DPA. This concentration, corresponding to 7×10^5 spores per mL, is about 3 orders of magnitude lower than the infectious dose of the spores [30, 42]. To determine the ratiometric sensing behavior of the DPA binding, values of blue over red emission intensities (I_B/I_R) were plotted for the different samples (Fig. 4.1b).

As a proof of DPA coordination to Eu^{3+} on the surface, a UV–Vis spectrum of DPA- **1.Eu**$^{3+}$ on quartz was compared to a solution spectrum of 0.5 mM aqueous

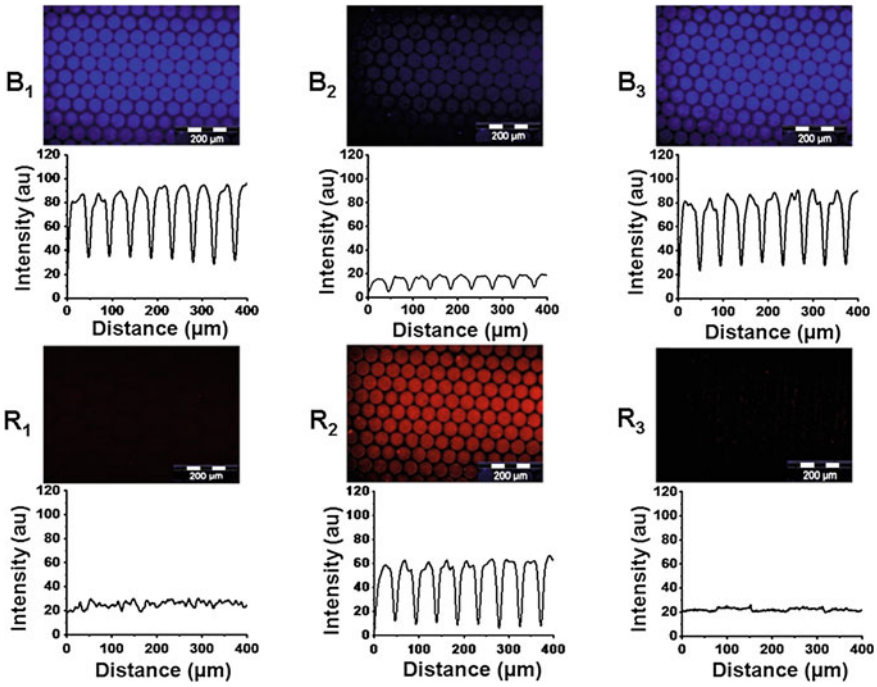

Fig. 4.1 Fluorescence microscopy images and corresponding intensity profiles of 50 μm dots on *β*-CD monolayers of an equimolar ratio of **1** and **2** (B_1, R_1), subsequently incubated in a solution of $EuCl_3$ for 30 min (B_2, R_2), followed by rinsing with MilliQ water and immersion into a 200 nM solution of DPA (B_3, R_3)

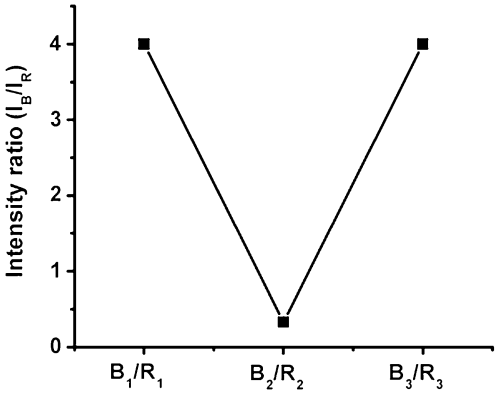

Fig. 4.2 Plot of the ratios of the maximum intensities of *blue* and *red* images in Fig. 4.1 upon Eu^{3+} and DPA binding

DPA-**1**.Eu^{3+}. To avoid the overlap of the naphthalene and DPA absorbances, only **1.Eu**$^{3+}$ was printed on a *β*-CD monolayer on quartz, followed by incubation into 1 mM DPA (pH 6.5). The UV–Vis spectrum (Fig. 4.2) showed the characteristic

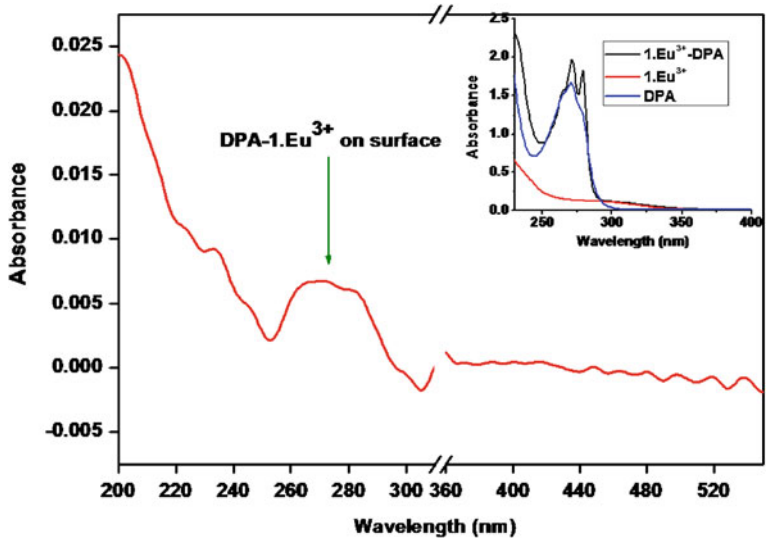

Fig. 4.3 UV−Vis spectrum of **1**.Eu^{3+}-DPA complex on a β-CD monolayer on quartz. Inset shows UV–vis spectra of 0.5 mM solutions of DPA, **1**.Eu^{3+} and DPA-**1**.Eu^{3+} in water (pH 6.5)

broad absorption bands between 260–280 nm as also observed in solution. This confirms that DPA forms a complex with **1**.Eu^{3+} on the surface, but also that the large excess of DPA does not remove the Eu^{3+} from ligand **1**, even at high (mM) concentrations. This is attributed to the fact that the stability constant of the EDTA-Eu^{3+} complex is nearly 8 orders of magnitude larger than that of the DPA-Eu^{3+} complex in water [25, 43] (Fig. 4.3).

The fluorescence intensity ratio of the Eu^{3+}-based sensing platform as a function of time upon addition of 200 nM DPA and corresponding fluorescence images are depicted in Fig. 4.4. It clearly indicates that the sensing response is complete within 10 min.

To determine the detection limit of DPA, intensity ratios of the detection substrates were plotted against the concentration of DPA (Fig. 4.5). Treatment of the surface with relatively high concentrations of DPA resulted in the expected maximal increase of the blue to red ratio, and reached saturation around 200 nM of DPA. However, at lower concentrations of DPA, the ratio was lower, and a detection limit of approx. 25 nm of DPA was obtained.

To show the selectivity of our system as a sensing platform for DPA, ratiometric fluorescence changes of patterns upon addition of different aromatic ligands such as the *o/m/p*-phthalic acids, nicotinic acid and its two isomers (picolinic and isonicotinic acid), and nicotinamide adenine dinucleotide (NAD) were investigated in 200 nM aqueous solutions at pH 6.5 (Fig. 4.6). The small or negligible fluorescence changes, combined with their lower occurrence in the spores [29], demonstrates the excellent selectivity.

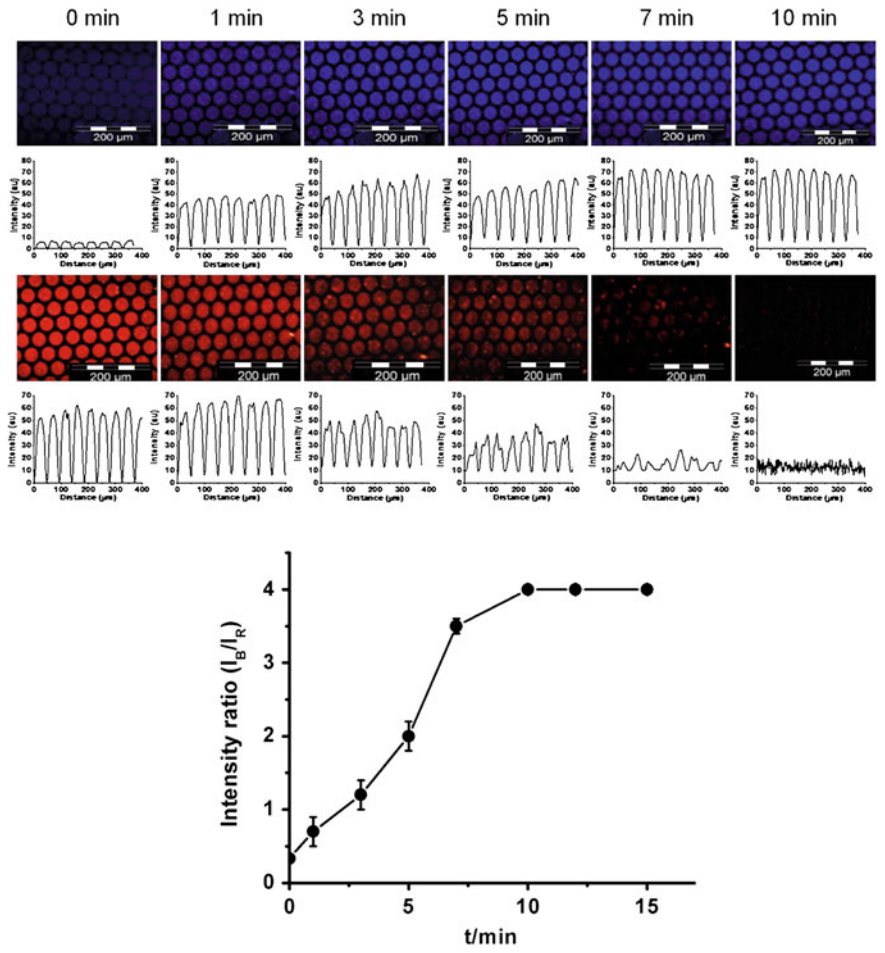

Fig. 4.4 Fluorescence microscopy images (*top*) of 50 μm dots prepared on *β*-CD monolayers by μCP (30 min) of an equimolar ratio of **1** and **2**, subsequently incubated in a solution of $EuCl_3$ for 30 min, followed by rinsing with MilliQ water and immersed into a 200 nM solution of DPA in H_2O (pH 6.5) with different incubation times and plot (*bottom*) of the fluorescence intensity ratios in time

4.3 Conclusions

In conclusion, we have demonstrated that the supramolecular europium-based luminescent sensing platform developed here can be employed for the ratiometric fluorescent detection of the anthrax biomarker DPA on glass substrates. The results show the excellent nanomolar sensitivity of the system toward DPA.

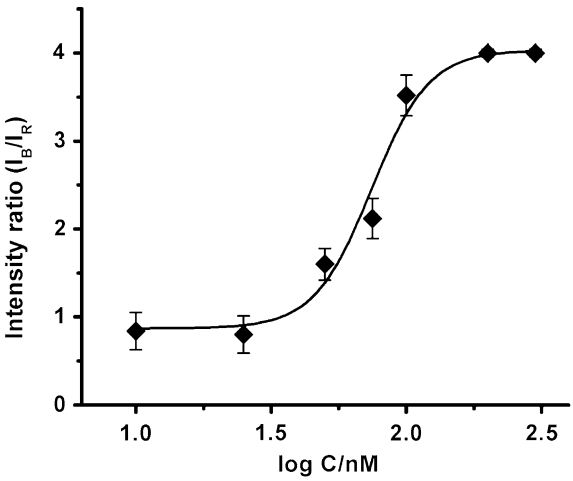

Fig. 4.5 Ratiometric fluorescence change of the supramolecular sensing surface as a function of DPA concentration

Moreover, the system has a remarkable selectivity over other potentially competitive aromatic ligands in water. This surface-assisted sensing system opens new avenues to build solid-state devices for the detection of biologically relevant ions and bacterial spores. From this point of view, real-time monitoring and imaging of analytes on a surface can be extended with supramolecular systems to yield new classes of sensing platforms on surfaces or in microfluidic devices. For creating a practical sensor device, more attention needs to be paid to investigating other antenna systems to eliminate the need for UV excitation, shorter fabrication routes, and other possible cross-sensitivities. Overall, the system exemplifies the power of noncovalent strategies to create sensing platforms since different small building blocks can be easily designed and synthesized and subsequently assembled onto such a platform to create a functional system.

4.4 Experimental Section

4.4.1 Materials

N-[3-(trimethoxysilyl)propyl]-ethylenediamine (TPEDA), 1,4-phenylene diisothiocyanate, dipicolinic acid, isophthalic acid, phthalic acid, terephthalic acid, picolinic acid, nicotinic acid, isonicotinic acid, and nicotinamide adenine dinucleotide were used as such. β-CD heptamine was synthesized as described before [40]. Compounds **1**, **1.Eu**$^{3+}$ and **2** used in this study were prepared and used as described previously (see Chap. 3) [41].

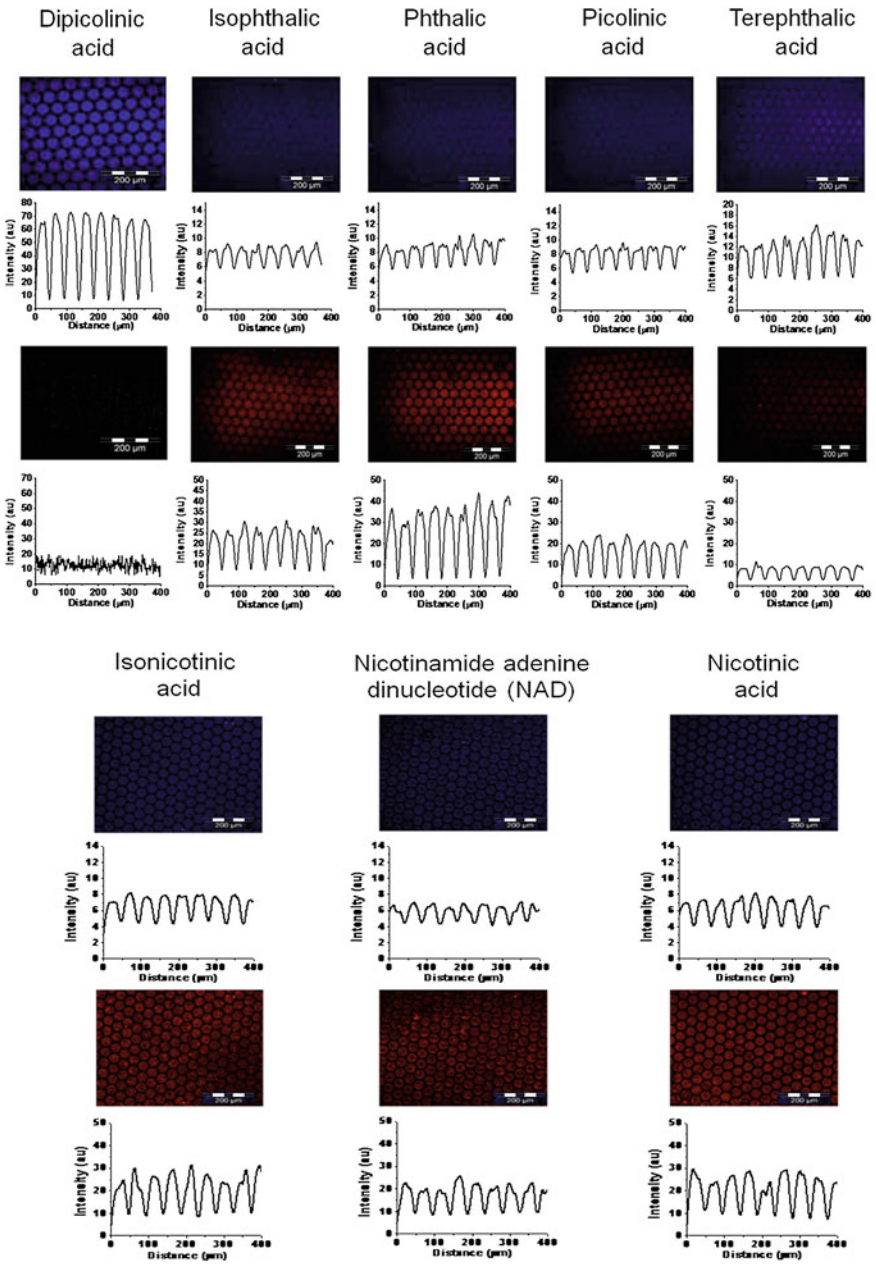

Fig. 4.6 Fluorescence images and corresponding bar graph of the supramolecular sensing surface to different competitive aromatic ligands (200 nM for each ligand)

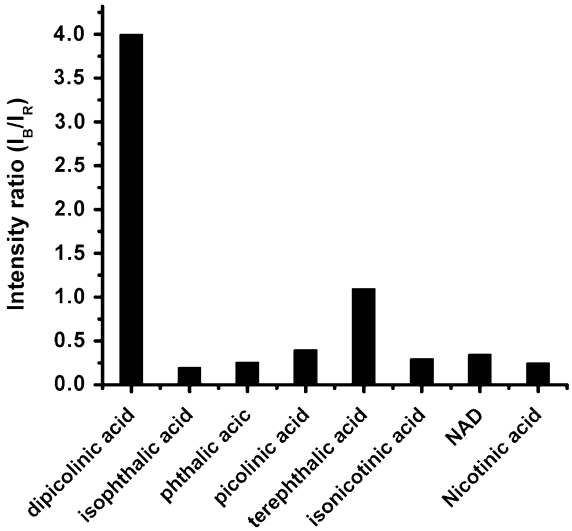

Fig. 4.6 (Continued)

4.4.2 Substrate and Monolayer Preparation

Microscope glass slides were used for β-cyclodextrin (β-CD) monolayer preparation [41]. The substrates were cleaned with piranha solution for 15 min (concentrated H_2SO_4 and 33 % aqueous H_2O_2 in a 3:1 ratio; Caution: piranha should be handled carefully) and rinsed with MilliQ. After drying in a nitrogen stream, the substrates were used immediately for silanized monolayer formation. The substrates were enclosed in a low-vacuum desiccator with 0.1 ml TPEDA, continually pumping for 5 min to create a vapor phase of TPEDA. After overnight incubation, the slides were rinsed with ethanol and dichloromethane to remove any excess of silanes, and subsequently dried in a nitrogen stream. The attachment of 1,4-phenylene diisothiocyanate was made in a 20 mM solution in toluene at 60 °C during 2 h. Samples were thoroughly rinsed with toluene and dried in a nitrogen flow. The β-CD layer attachment was made during 2 h in an aqueous 0.1 mM β-cyclodextrin-heptaamine solution (pH $\sim$ 7) at 60 °C. Samples were thoroughly rinsed with water and dried in a nitrogen flow.

4.4.3 Microcontact Printing

Patterned silicon substrates were made by photolithography followed by reactive ion etching (RIE) or e-beam lithography. They consisted of gratings of 50 μm dots at 70 μm period with the height of 1 μm. PDMS stamps were prepared by casting a

10:1 (v/v) mixture of poly(dimethylsiloxane) (PDMS) prepolymer and curing agent (Sylgard 184, Dow Corning) against a silicon master. After overnight curing at 60 °C, the stamps were oxidized by oxygen plasma for 1 min and subsequently inked by dropping aqueous adsorbate solution onto the stamp. Before printing, the stamps were blown dried in a stream of nitrogen. The stamps were brought into conformal contact with the substrate for 30 min. The stamps were changed for each new print and the same inking procedure was used. After stamp removal, the printed substrates were rinsed with copious amounts of water, blown dry with nitrogen and imaged with fluorescence microscopy.

4.4.4 Fabrication of the Sensing Platform and DPA Detection

The substrate was printed with an equimolar mixture of **1** and **2** (2 mM each) for 30 min onto a β-CD substrate with saturated native β-CD present in the EtOH/MilliQ mixture (3:1). This was followed by rinsing with MilliQ water and drying in a stream of nitrogen. The printed substrates were immersed in a 4 mM solution of $EuCl_3$ in MilliQ water for 30 min, followed by rinsing and drying. Afterwards, for concentration-dependent measurements, glass slides were incubated into the solutions of DPA with different concentrations in H_2O (pH = 6.5) for 10 min with continuous stirring, followed by rinsing with water, and drying with nitrogen flow. For time-dependent measurements, glass slides were incubated into a 200 nM solution of DPA in H_2O (pH = 6.5) with different incubation times with continuous stirring, followed by rinsing with water, and drying with nitrogen flow. For selectivity measurements, glass slides were incubated into 200 nM solutions of different competitor aromatic ligands for 10 min with continuous stirring, followed by rinsing with water, and drying with nitrogen flow.

4.4.5 Fluorescence Microscopy

Fluorescence microscope images were taken using an Olympus inverted research microscope IX71 equipped with a mercury burner U-RFL-T as light source and a digital Olympus DR70 camera for image acquisition. UV excitation (300 nm $\leq \lambda_{ex} \leq$ 400 nm) and blue emission (410 nm $\leq \lambda_{em} \leq$ 510 nm) was filtered using a Dapi Olympus filter cube. UV excitation (300 nm $\leq \lambda_{ex} \leq$ 400 nm) and red emission (narrow band pass at 615 nm) was filtered using a Olympus filter cube. All fluorescence microscopy images were acquired in air.

Acknowledgments Shu-Han Hsu is acknowledged for making fruithful discussions.

References

1. M. Deniz Yilmaz, S.-H. Hsu, D.N. Reinhoudt, A.H. Velders, J. Huskens, Angew. Chem. Int. Ed. *49*, 5938−5941 (2010)
2. D.A. Henderson, Science **283**, 1279–1282 (1999)
3. M. Enserink, Science **294**, 1266–1267 (2001)
4. M. Enserink, Science **294**, 490–491 (2001)
5. P.T. Yung, E.D. Lester, G. Bearman, A. Ponce, Biotechnol. Bioeng. **98**, 864–871 (2007)
6. W.T. Sanderson, R.R. Stoddard, A.S. Echt, C.A. Piacitelli, D. Kim, J. Horan, M.M. Davies, R.E. McCleery, P. Muller, T.M. Schnorr, E.M. Ward, T.R. Hales, J. Appl. Microbiol. **96**, 1048–1056 (2004)
7. R.J. Sharp, A.G. Roberts, J. Chem. Technol. Biotechnol. **81**, 1612–1625 (2006)
8. M. Zourob, S. Elwary, A. Turner, *Principles of Bacterial Detection: Biosensors, Recognition Receptors, and Microsystems* (Springer, New York, 2008)
9. G. Coimbatore, S. M. Presley, J. Boyd, E. J. Marsland, G. P. Cobb in *Advances in Biological and Chemical Terrorism Countermeasures*, ed. by R.J. Kendall, S.M. Presley, G.P. Austin, P.N. Smith (CRC Press, Boca Raton, 2008) pp. 159–175
10. P.A. Lieberzeit, F.L. Dickert, Anal. Bioanal. Chem. **391**, 1629–1639 (2008)
11. G.F. Bailey, S. Karp, L.E. Sacks, J. Bacteriol. **89**, 984 (1965)
12. R. Goodacre, B. Shann, R.J. Gilbert, E.M. Timmins, A.C. McGovern, B.K. Alsberg, D.B. Kell, N.A. Logan, Anal. Chem. **72**, 119–127 (2000)
13. D.R. Walt, Anal. Chem. **72**, 738a–746a (2000)
14. G.W. Gould, A.J. Sale, W.A. Hamilton, J. Gen. Microbiol. **57**, R28 (1969)
15. L.J. Rode, J.W. Foster, Nature **188**, 1132–1134 (1960)
16. H.S. Levinson, M.T. Hyatt, J. Bacteriol. **70**, 368–374 (1955)
17. W. Hurtle, E. Bode, D.A. Kulesh, R.S. Kaplan, J. Garrison, D. Bridge, M. House, M.S. Frye, B. Loveless, D. Norwood, J. Clin. Microbiol. **42**, 179–185 (2004)
18. A. Fasanella, S. Losito, R. Adone, F. Ciuchini, T. Trotta, S.A. Altamura, D. Chiocco, G. Ippolito, J. Clin. Microbiol. **41**, 896–899 (2003)
19. R.H. Yolken, S.B. Wee, J. Clin. Microbiol. **19**, 356–360 (1984)
20. D. King, V. Luna, A. Cannons, J. Cattani, P. Amuso, J. Clin. Microbiol. **41**, 3454–3455 (2003)
21. G. Thompson, C. Forster, Water Res. **37**, 2636–2644 (2003)
22. R.M. Jarvis, R. Goodacre, Anal. Chem. **76**, 40–47 (2004)
23. X.Y. Zhang, M.A. Young, O. Lyandres, R.P. Van Duyne, J. Am. Chem. Soc. **127**, 4484–4489 (2005)
24. P.M. Pellegrino, N.F. Fell, J.B. Gillespie, Anal. Chim. Acta **455**, 167–177 (2002)
25. J.P. Kirby, M.L. Cable, D.J. Levine, H.B. Gray, A. Ponce, Anal. Chem. **80**, 5750–5754 (2008)
26. M.L. Cable, J.P. Kirby, K. Sorasaenee, H.B. Gray, A. Ponce, J. Am. Chem. Soc. **129**, 1474–1475 (2007)
27. E.D. Lester, A. Ponce, IEEE Eng. Med. Biol. **21**, 38–42 (2002)
28. E.D. Lester, G. Bearman, A. Ponce, IEEE Eng. Med. Biol. **23**, 130–135 (2004)
29. Q.Y. Li, P.K. Dasgupta, H.K. Temkin, Environ. Sci. Technol. **42**, 2799–2804 (2008)
30. K.L. Ai, B.H. Zhang, L.H. Lu, Angew. Chem. Int. Ed. **48**, 304–308 (2009)
31. M.L. Cable, J.P. Kirby, D.J. Levine, M.J. Manary, H.B. Gray, A. Ponce, J. Am. Chem. Soc. **131**, 9562–9570 (2009)
32. R. Zimmerman, L. Basabe-Desmonts, F. van der Baan, D.N. Reinhoudt, M. Crego-Calama, J. Mater. Chem. **15**, 2772–2777 (2005)
33. Y.R. Kim, H.J. Kim, J.S. Kim, H. Kim, Adv. Mat. **20**, 4428–4432 (2008)
34. M. Crego-Calama, D.N. Reinhoudt, Adv. Mater. **13**, 1171–1174 (2001)
35. H.J. Kim, S.J. Lee, S.Y. Park, J.H. Jung, J.S. Kim, Adv. Mater. **20**, 3229–3234 (2008)

36. L. Basabe-Desmonts, J. Beld, R.S. Zimmerman, J. Hernando, P. Mela, M.F.G. Parajo, N.F. van Hulst, A. van den Berg, D.N. Reinhoudt, M. Crego-Calama, J. Am. Chem. Soc. **126**, 7293–7299 (2004)
37. M.S. Tremblay, M. Halim, D. Sames, J. Am. Chem. Soc. **129**, 7570–7577 (2007)
38. H. Takakusa, K. Kikuchi, Y. Urano, H. Kojima, T. Nagano, Chem. Eur. J. **9**, 1479–1485 (2003)
39. J.R. Acharya, H. Zhang, X. Li, E.E. Nesterov, J. Am. Chem. Soc. **131**, 880–881 (2009)
40. M.J.W. Ludden, D.N. Reinhoudt, J. Huskens, Chem. Soc. Rev. **35**, 1122 (2006)
41. S.H. Hsu, M.D. Yilmaz, C. Blum, V. Subramaniam, D.N. Reinhoudt, A.H. Velders, J. Huskens, J. Am. Chem. Soc. **131**, 12567–12569 (2009)
42. H.S. Shafaat, A. Ponce, Appl. Environ. Microbiol. **72**, 6808–6814 (2006)
43. S.L. Wu, W.D. Horrocks Jr, Anal. Chem. **68**, 394–401 (1996)

Chapter 5
A Supramolecular Sensing Platform in a Microfluidic Chip

A supramolecular platform based on self-assembled monolayers (SAMs) has been implemented in a microfluidic device. The system has been applied for the sensing of two different analyte types: biologically relevant phosphate anions and aromatic carboxylic acids which are important for anthrax detection. An Eu(III)-EDTA complex was bound to β-cyclodextrin monolayers via orthogonal supramolecular host–guest interactions. The self-assembly of the Eu(III)-EDTA conjugate and naphthalene β-diketone as an antenna resulted in the formation of a highly luminescent lanthanide complex on the microchannel surface. Detection of different phosphate anions and aromatic carboxylic acids was demonstrated by monitoring the decrease in red emission following displacement of the antenna by the analyte. Parallel fabrication of five sensing SAMs in a single multichannel chip was performed, as a first demonstration of phosphate and carboxylic acid screening in a high-throughput format that allows a general detection platform for both analyte systems in a single test run.

5.1 Introduction

It is of utmost importance to detect low concentrations of small molecules and solutes in mixtures of complex milieu for toxicology [2–4], drug discovery [5–7], diagnostics [8–10], and anti-bioterrorism [11, 12]. Among many chemical, electrochemical, biological, and photoluminescence-based small molecule detection, fluorescence turn-on/off sensing has attracted significant attention, offering high sensitivity [13–16] and reversibility [17, 18]. Lanthanide (Ln^{3+})-based luminescent detection of small molecules such as nerve agents [2–4], antagonists [11, 12], phosphate anions [19, 20], and the anthrax biomarker dipicolinic acid (DPA)

Part of this chapter has been published in Ref. [1].

M. D. Yilmaz, *Orthogonal Supramolecular Interaction Motifs for Functional Monolayer Architectures*, Springer Theses, DOI: 10.1007/978-3-642-30257-2_5,

[21–23] has been most promising among the many turn-on/off sensing methods owing to the unique photophysical properties of Ln^{3+}—antenna chelates with their bright luminescence upon sensitization by an antenna, long luminescence lifetimes compared to free Ln^{3+}, and sharp line-like emission bands at long wavelengths [24–26], overcoming autofluorescence and light scattering, and resulting in a high color purity of the emitted light [27].

Surface-confined sensing using SAMs offers advantages compared to sensing in solution such as ease and reproducibility of SAMs [28, 29], fast response times owing to the faster analyte–receptor interaction, and real-time and real-space measurements [30, 31]. Previous studies have shown that SAMs can function as optical sensors when functionalized with fluorescent groups on flat surfaces [32–34] and in microfluidic systems [35, 36].

Phosphate anions play an important role in various physiological events and they take part in almost all metabolic processes. Among various phosphates, pyrophosphate and ATP are crucial anions for the transfer of genetic information, and metabolic and bioenergetic reactions [37]. Fluorescence-based detection of biologically relevant phosphate anions still remains a challenge due to the difficulty of designing binding motifs for anions[38] and achieving an effective fluorescent signal change upon anion binding[16, 39]. Recently, an Ln^{3+}-based displacement assay was employed for phosphate anions on gold nanoparticles in solution [19] and on a gold surface [18].

Concurrently, some aromatic carboxylic acids have crucial importance in bioterrorism, especially in anthrax detection [40]. Anthrax is an acute disease and a potential biological warfare agent caused by Bacillus anthracis. The detection of Bacillus spores with rapid response, high selectivity, and sensitivity is very important in order to prevent a bioterroristic attack or outbreak of disease [41–43]. Bacillus spores contain up to 1 M DPA, corresponding to 5–15 % of the dry mass of the bacterial spore [44–46], offering a convenient biomarker for anthrax detection. Ln^{3+}-based luminescent detection of DPA has been very promising by using DPA as an antenna itself [21, 22, 47] or as Ln^{3+}-DPA chelates, [23] allowing fast, highly selective, and sensitive detection of bacterial spores. Recently, ratiometric detection of DPA was employed by fabricating microarrays via patterning of a monolayer surface [23].

In this study, we present a novel high-throughput platform for a general detection method of biologically relevant phosphate anions and the Bacillus anthracis biomarker DPA on a supramolecular monolayer surface by using a microfluidic approach. The microfluidic approach has attracted significant attention in the last decades for chemical and biological assays because of faster detection time, low consumption of analyte and reagents, and the possibility of integrated continuous monitoring of analyte solutions[36, 48–51] Here, β-cyclodextrin monolayers known as molecular printboards [52] were employed on a glass-silicon microchip surface and building blocks were attached to the monolayers in a noncovalent fashion that allow phosphate anion and DPA sensing. To the best of our knowledge, this microchip-based sensing platform constitutes the first lanthanide-based surface receptor system that provides a general detection

platform for two different analyte systems, as well as the first example of integration of sensing the phosphate anions and DPA in a microfluidic device.

5.2 Results and Discussion

5.2.1 Fabrication of the Sensing Platform and Anion Detection

Surface-assisted sensitized luminescence of Eu^{3+} on a molecular printboard was demonstrated in a previous study for the sensing of biological molecules such as the Bacillus anthracis biomarker DPA (see Chap. 4) [23] In this study, luminescent SAMs on a microchip surface were fabricated to develop a general detection platform of small molecules such as the biologically relevant phosphate anions and aromatic carboxylic acids in a high-throughput format. The sensing platform was developed in a microfluidic device by using the controlled attachment of the building blocks in a supramolecular manner, through multivalent orthogonal linkers. Such a supramolecular surface platform was chosen for this study, since supramolecular interactions combined with multivalency offer high flexibility such as controlled positioning of molecules, fine-tuning of assemblies and their interaction properties, binding strength, binding stoichiometry, binding dynamics, and reversibility [53]. Cyclodextrin (βCD)-based host–guest chemistry at the microchip interface was applied to orient the attachment of building blocks of interest to the microchip surface. Microchannels are miniaturized platforms that can be individually accessible and addressable, allowing production of sensing arrays for multianalyte systems within a single device. Thereby, the supramolecular sensing system was implemented on the surface of a multichannel chip as a demonstration of a high-throughput sensing device.

A multichannel chip (15 mm × 25 mm) with five parallel channels was designed for generation of the sensing array via the formation of βCD SAMs and subsequent attachment of building blocks of interest on each channel surface (Fig. 5.1a). Each channel has a width of 50 μm and equal depth, and the channels are separated by 50 μm. The channels have independent inlets and they share a common outlet. The chip was fabricated in silicon with a glass cover slip.

Parallel synthesis of five sensing SAMs in the multichannel chip was performed by the formation of βCD SAMs on the channel surface in three subsequent steps [53]. The microchip surface was cleaned and activated with piranha, and a amino-terminated TPEDA (N-[3-(trimethoxysilyl)propyl]ethylenediamine) SAM was formed. After DITC (1,4-phenylene-diisothiocyanate) was attached to the TPEDA SAMs, βCD heptamine was bound onto the surface in the last step, leading to an array of five βCD SAMs confined to a single chip, and providing a functional layer for further surface modification in the multichannel.

Two building blocks were used to fabricate the sensor surface in the microchip: an ethylenediamine tetraacetic acid (EDTA)-based ligand (1) for binding Eu^{3+} and the receptor surface, and a naphthalene-based antenna (2) for coordination to Eu^{3+}

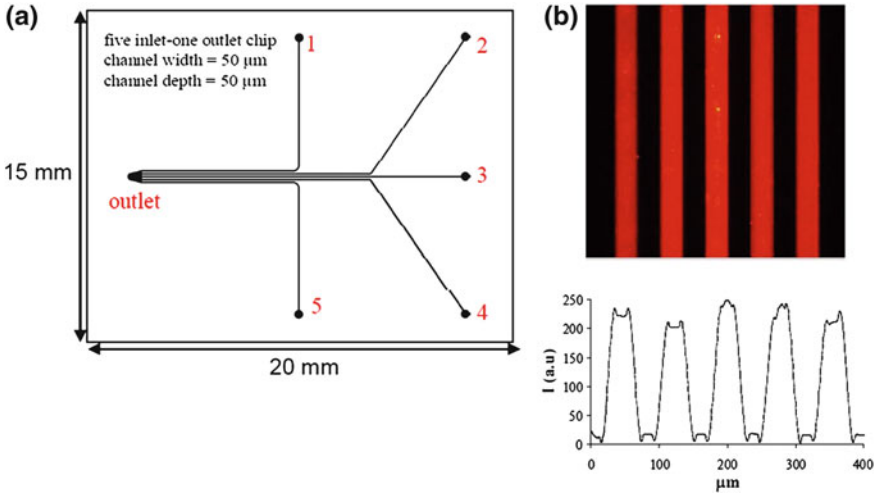

Fig. 5.1 Design of the five inlet-one outlet multichannel chip surface (**a**), and a fluorescence microscopy image and concomitant intensity profile of the red luminescent multichannel device (**b**)

via the diketonate moiety (Scheme 5.1). Building block **1** has adamantyl groups for immobilization onto the *β*CD SAMs. To fabricate sensing surfaces on the microchip surface, a stepwise procedure was followed. Briefly, in the first step, 1 mM of **1.Eu**$^{3+}$ was attached on the *β*CD monolayer after 30 min incubation in the microchip. After cleaning the microchip surface with water for 10 min, 100 μM of **2** was incorporated onto *β*CD SAMs via coordination of **2** with **1.Eu**$^{3+}$ as seen in Scheme 5.1. After a second cleaning step of the microchip surface with water for 10 min, the multichannel surface was imaged by fluorescence microscope using filter R ($300 < \lambda_{exc} < 400$ nm, $\lambda_{em} = 615$ nm). Five luminescent SAM-modified microchannels were visualized simultaneously (Fig. 5.1b) by fluorescence microscopy, which showed energy transfer from the Eu-coordinated napthalene moiety of **2** to the Eu^{3+} center of **1.Eu**$^{3+}$, and the emission of red light at 615 nm as studied before [22, 44]. Thereby, a highly luminescent surface platform was achieved in the multichannel device for the detection of phosphates and aromatic carboxylic acids.

The mechanism of anion detection is based on the displacement of **2** from **2-1.Eu**$^{3+}$ by a guest anion as shown in Scheme 5.1. Displacement assays have been studied before and the mechanism of displacement is well established, [18, 54, 55] and the same mechanism is assumed in this study. Briefly, the sensing layer on the microchip surface is an ensemble of **1.Eu**$^{3+}$ and the antenna **2**, and when an anionic guest is added to the ensemble, it displaces **2**, and triggers a fluorescence change upon binding to **1.Eu**$^{3+}$, leading to a decrease in red fluorescence at 615 nm. Thus, the detection of phosphates and aromatic carboxylic acids is based on the recognition of the guest anion by the Eu^{3+}- based receptor and the displacement of **2**. Thus, the resulting decrease in the fluorescence intensity was monitored and quantified by fluorescence microscopy.

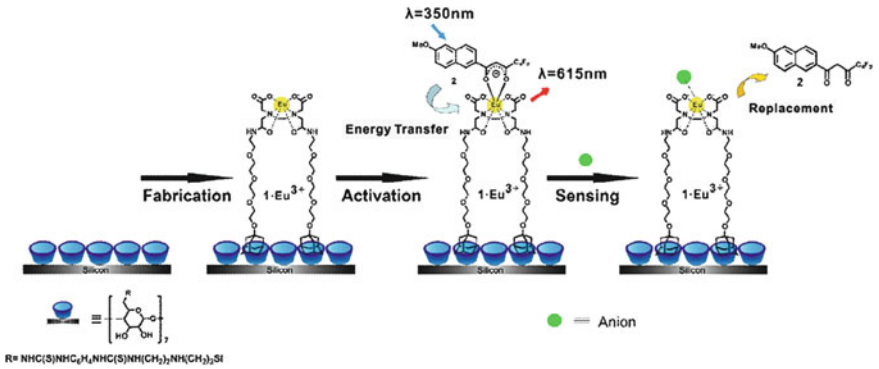

Scheme 5.1 The construction of supramolecular sensing system in a microchip and the detection of an anion of interest

5.2.2 *Sensing of Biologically Relevant Phosphates*

The luminescent multichannel platform was used for the detection of biologically relevant phosphate anions. Five different phosphates (1 mM each), ATP, AMP, ADP, hydrogen phosphate (Pi), and pyrophosphate (PPi) were injected continuously from each inlet (at 1 μl/min by a peristaltic pump) and their sensing was evaluated within 1 h. Among those five phosphate anions, only ATP and PPi caused a strong response at the **2-1.Eu^{3+}** complex (Fig. 5.2). The sensing of these five anions along with NADP and triphosphate (PPPi) was also studied as a function of time, and around 40 and 35 % decrease in fluorescence intensity was observed for both ATP and PPPi, while 22 and 15 % quenching of red emission was observed for PPi and NADP, respectively, in 10 min (ATP > PPPi > PPi > NADP at t = 10 min) as seen in Fig. 5.3. Around 60 % decrease in fluorescence intensity was obtained for ATP after 1 h, whereas PPPi and PPi showed around 45 % decrease in red emission, and the effect of NADP on displacement of the antenna was around 20 % after 1 h (ATP > PPPi ≈ PPi > NADP at t = 60 min). The response half-time of ATP was determined based on the exponential decay curve in Fig. 5.3, and was found to be about 10 min.

The reasons behind the different sensing properties of the anions on the microchannel surface are presumably due to differences in binding affinitiy of the anions to Eu^{3+} which is correlated with the number of phosphate oxygens that coordinate to Eu^{3+} after the displacement of the antenna [56]. As seen in Fig. 5.3, PPPi displaced **2** almost as effectively as ATP indicating the importance of the number of phosphate oxygens on the strong coordination with Eu^{3+} [57, 58] resulting in displacement of **2** from **2-1.Eu^{3+}**. PPi as a diphosphate also caused a fairly strong response of the **2-1.Eu^{3+}** complex owing to its high binding affinity to Eu^{3+} [56]. On the other hand, among the diphosphates PPi, ADP, and NADP different responses were seen, especially the sensing of PPi was much stronger than

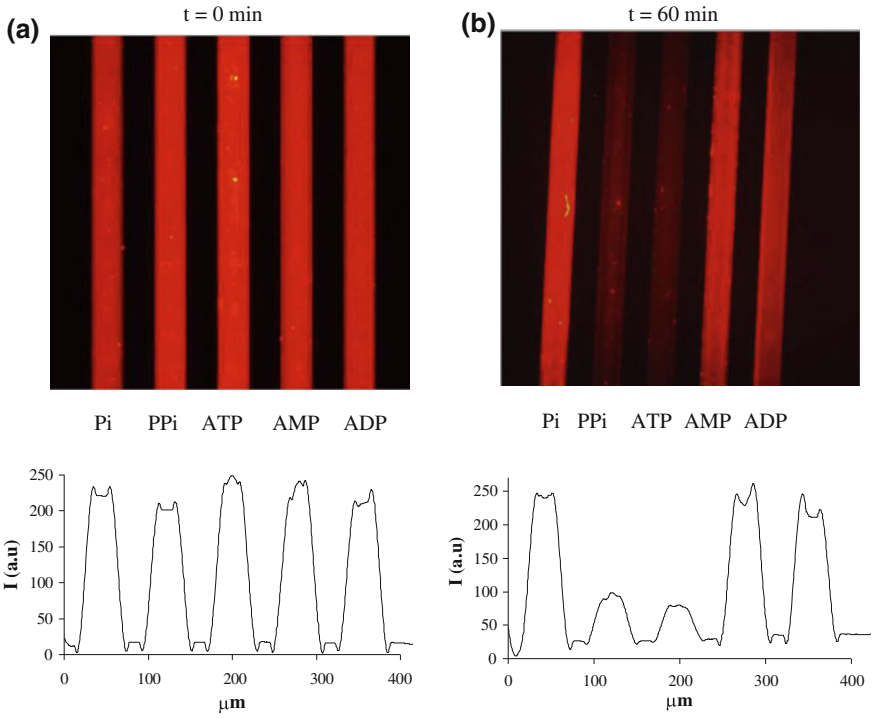

Fig. 5.2 The effect of phosphate anions at 1 mM concentration each (from left to right; hydrogen phosphate (Pi), pyrophosphate (PPi), ATP, AMP, ADP) on the displacement of the antenna from **2-1.Eu**$^{+3}$ on the multichannel surface after 0 min (**a**) or 60 min (**b**), using a flow rate of 1 μl/min

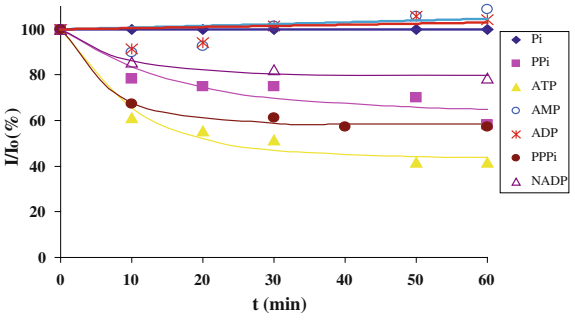

Fig. 5.3 Fluorescence intensity versus time profiles of 1 mM phosphates (Pi, PPi, ATP, AMP, ADP, PPPi, NADP) for selectivity and response time determination on a microchannel surface

the other diphosphates indicating that the side groups of ADP and NADP might decrease the binding affinity of the phosphate groups to Eu^{3+}, thus leading to less effective displacement of **2** from **2-1.Eu**$^{3+}$ compared to PPi. Thus, these results show that the phosphates possess different sensitivities to the **2-1.Eu**$^{3+}$ complex, especially ATP, PPi, and PPPi exhibit stronger response to the Eu^{3+}-based assembly

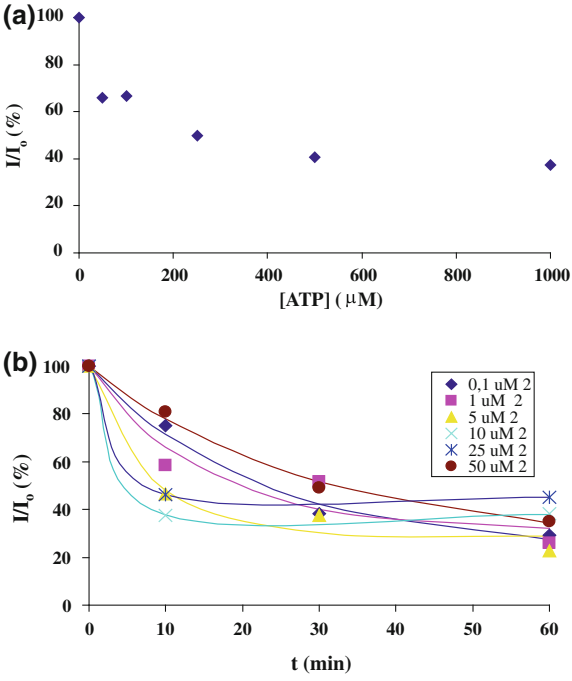

Fig. 5.4 The detection sensitivity profile of ATP at 60 min as a function of different ATP concentrations **a** Fluorescence intensity versus time profiles of 1 mM ATP in the presence of different concentrations of **2**

compared to the other phosphates. More importantly, this multichannel surface platform allows high-throughput detection of phosphates providing different information for each anion at a single test run.

To determine the detection limit of ATP sensing on the microchip platform, ATP detection was performed as a function of concentration. Five different concentrations ranging from 1 mM down to 50 μM ATP were injected continuously from each inlet by a peristaltic pump and their sensing was evaluated within 1 h. Figure 5.4a shows the normalized intensity (I/I_0) profile of five different concentrations at t = 60 min. Similar responses were observed with ATP concentrations from 1 mM down to 250 μM (around 50–60 %), and around 35 % decrease in red emission was obtained for 50 μM ATP (Fig. 5.4b). Thus, ATP sensing by the Eu^{3+}-based complex was achieved in the μM range. This is consistent with earlier reported data, which showed ATP detection in the μM [37, 59, 60] or mM concentration range [61].

The experiments described above were all performed in the absence of **2** in solution, therefore, displacement of **2** led to removal of **2** from the system and thus to kinetically determined fluorescence readings. Subsequently, ATP sensing was performed in the presence of different concentrations of **2** in order to investigate ATP detection while attempting to reach thermodynamic equilibrium of the displacement reaction of **2** from **2-1.Eu^{3+}** by ATP. Mixtures of 1 mM ATP with five different concentrations of **2**, ranging from 0.1 to 50 μM, were injected continuously from each inlet and their sensing of **2-1.Eu^{3+}** was evaluated within 1 h.

Figure 5.4b shows that the decrease in red fluorescence was similar for all conditions. No clear trend was obtained for different concentrations of **2**, nor in response time. These results show that the binding strength of ATP to Eu^{3+} is much higher than that of the antenna **2**.

5.2.3 *Screening of an Anthrax Biomarker and Potentially Interfering Anions*

The same supramolecular lanthanide-based microfluidic platform was also used for the detection of the anthrax biomarker DPA, among other potentially competitive aromatic ligands as a demonstration of a surface-based sensing device that offers a general high-throughput detection platform both for phosphates and aromatic carboxylates. In order to investigate aromatic carboxylic acid detection, five different aromatic carboxylic acids (1 mM each), *o/m/p*-phthalic acids, picolinic acid, and DPA, were injected from each inlet continuously and their sensing was evaluated within 1 h. Among those five aromatic ligands (Fig. 5.5a), only DPA was sensed by **2**-**1.Eu**$^{3+}$ and selectively displaced the antenna, thus quenched around 80 % of the red luminescence in 10 min, whereas the effect of the other aromatic acids on the displacement of **2** was negligible (up to 25 % quenching of red emission with terephthalic acid) (Figs. 5.5c, 5.6). Excellent selectivity was achieved with DPA over other potentially interfering aromatic acids after 1 h (Fig. 5.5d, 5.6), while other interferants showed weak response on the sensor surface (up to 35 % quenching of red emission with picolinic and isophthalic acid). The response half-time of DPA was determined based on the exponential decay curve in Fig. 5.6, and DPA showed a response half-time of around 5 min.

The high selectivity of DPA sensing on **2**-**1.Eu**$^{3+}$ is attributed to a higher binding affinity of DPA to Eu^{3+} [62, 63] due to its stronger coordination to Eu^{3+} via two carboxylic acid groups and the basic nitrogen atom on its aromatic ring, whereas the other aromatic ligands coordinate to Eu^{3+} via fewer groups. In addition, the carboxylic acid screening in solution was also performed and only DPA selectively displaced **2** after 10 min (data not shown) owing to the much stronger coordination of DPA with **1.Eu**$^{3+}$ than that of **2**, showing consistent results with those obtained on receptor surface. Thus, these results show that all aromatic carboxylic acids show different sensing properties to **2**-**1.Eu**$^{3+}$ complex, and especially DPA exhibited excellent selectivity and a quick response time (within 10 min). Thus, this multichannel sensing platform offers a common detection system for both aromatic carboxylic acids and phosphates.

To determine the detection limit of DPA sensing on the microchip platform, DPA detection was performed as a function of concentration. Initially, five different concentrations ranging from 1 mM down to 500 nM DPA were injected continuously from each inlet by a peristaltic pump and their sensing was evaluated

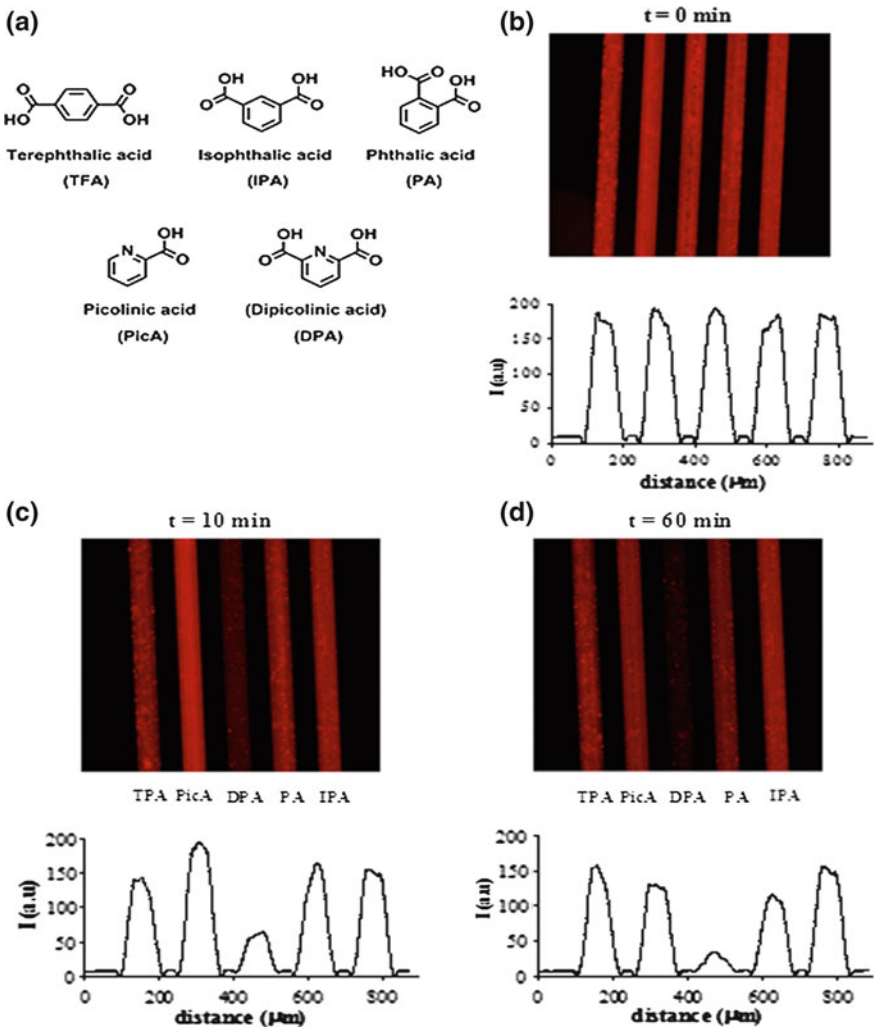

Fig. 5.5 The structure of aromatic carboxylic acids: *p*-phthalic acid (TPA), picolinic acid (PicA), dipicolinic acid (DPA), *o*-phthalic acid (PA), and *m*-phthalic acid (IPA) (**a**) Fluorescence microscopy images and intensity profiles of the multichannel surface upon carboxylic acid screening at t = 0 min (**b**) t = 10 min (**c**) and t = 60 min (**d**)

within 1 h. Lower concentrations down to 40 nM were also used to determine the detection limit of DPA. The intensity ratio (I/I_0) values of the sensor substrates were plotted as a function of the DPA concentration (0–1 μM) at t = 60 min in Fig. 5.7. Lower concentrations of DPA resulted in less quenching of the red emission showing that DPA sensing is concentration dependent. 1 μM DPA quenched red emission as effective as 1 mM DPA (around 70–80 %), and nM concentrations of DPA still showed significant response on the sensor surface

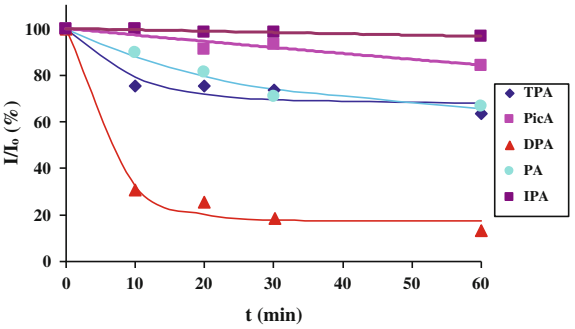

Fig. 5.6 Fluorescence Intensity versus time profiles of 1 mM aromatic carboxylic acids (*p*-phthalic acid, picolinic acid, DPA, *o*-phthalic acid, and *m*-phthalic acid) for selectivity and response time determination on the microchannel surface

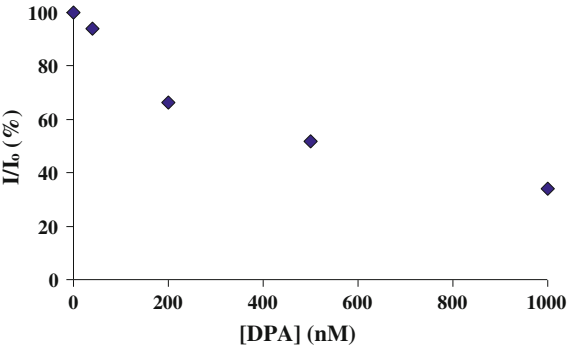

Fig. 5.7 The detection sensitivity profile of DPA at 60 min as a function of different DPA concentrations

(Fig. 5.7). Thus, DPA was sensed by the Eu^{3+}-based complex with <100 nM detection limit. Such a detection sensitivity range is consistent with the literature [24].

In a recent study, ratiometric detection of DPA was employed by us at molecular printboards using a lanthanide-based surface-receptor system [23]. DPA showed a very high selectivity over other potentially competitive aromatic ligands in water with nanomolar sensitivity, and the sensing response was complete within 10 min on glass substrate, showing consistent and similar results to those reported here. Our study demonstrates the development of a microfluidic device by using a different antenna **2** for the detection of bacterial spores and other anions such as biologically relevant phosphates at a high-throughput format.

5.3 Conclusion

In conclusion, we have developed a supramolecular sensing platform on a microchip surface that allows the detection of biologically relevant phosphate anions and aromatic carboxylic acids at a high-throughput format. ATP and pyrophosphate among various phosphate anions, and the anthrax biomarker DPA among various aromatic carboxylic acids showed a strong response to the sensitized Eu^{3+} luminescence-based microchip surface, exhibited by strong quenching

of red emission for the anions and DPA in a few to tens of minutes. ATP was sensed by **2-1.Eu^{3+}** and showed μM detection sensitivity. A higher detection sensitivity (∼100 nM) was achieved for DPA.

Therefore, as a first demonstration of phosphate and carboxylic acid sensing on the same lanthanide-based surface-receptor platform in a microfluidic chip at a high-throughput format, this study offers a general detection platform for phosphates and carboxylic acids in a single test run with high detection sensitivity and selectivity. From this point of view, this supramolecular surface assisted sensing system in multichannel opens new avenues to yield new classes of surface-based detection devices for biologically relevant ions and bacterial spores. Real-time imaging and continuous monitoring of analyte solutions with the power of microfluidics in combination with creating functional systems with the power of supramolecular chemistry offers new designs of miniaturized sensing systems for different kinds of small molecules which might have biological and diagnostic importance. Overall, this system exemplifies the significance of microfluidics and noncovalent strategies to create microscale sensing devices by fine-tuning different small building blocks which provide different functionalities when assembled onto such a sensor surface.

5.4 Experimental Section

General Procedures. All reactions involving air- or moisture-sensitive reagents or intermediates were performed under an inert atmosphere of argon in glassware. Unless otherwise noted, solvents and reagents were reagent grade and used without further purification. β-Cyclodextrin (βCD) heptamine, the Eu(III)-EDTA complex **1.Eu^{3+}** and the antenna naphthalene β-diketone **2** were synthesized as described before [64–66].

Microchip Fabrication Procedure. The silicon-glass microchip was fabricated by following standard microfabrication processes [67]. Microchannels were defined in a (100) silicon wafer (resistivity 5–10 Ω cm, diameter 100 mm) via standard UV-lithography using a mask of photoresist (Olin 907-17 photoresist) followed by deep reactive ion etching (BOSCH-type process). Inlet and outlet holes were fabricated by powderblasting [68]. The silicon wafer was bonded to Borofloat glass via anodic bonding (T = 400 °C, U_{max} = 1200 V, t = 10 min) and the silicon glass wafer was diced into separate chips (chips size: 15 mm × 20 mm). Channel dimensions were 50 μm × 50 μm (width × depth). The length of a single channel of interest was 6 mm and separation between the channels was 50 μm.

Surface Modification of the Microchips. The microchannel surface was functionalized with βCD SAMs by following a three-step reaction, as described by Ludden et al. [69]. Prior to surface modification, intense piranha cleaning was performed inside the microchip via vacuum and then followed by water cleaning. After drying the chip in a stream of N_2, approximately 500 μl freshly distilled toluene was flushed through the chip. Thereafter, a 5 mM solution of N-[3-

(trimethoxysilyl)propyl]ethylenediamine (TPEDA) in toluene was injected through the microchip by the syringe pump with a 0.1 μl/min flow rate for 4 h at room temperature. Distilled toluene was flushed through the chip for 30 min at a flow rate of 0.1 μl/min and then followed by flushing at 10 μl/min for 5 min to get rid of any possible aggregates from the channels. After this step, 10 mM 1,4-phenylene-diisothiocyanate (DITC) in toluene was flushed inside the microchip and incubated for 4 h at 60 °C followed by a rinse with toluene and then with ethanol. After drying the chip, the chip was washed with Millipore water for 5 min, and 10 mM βCD heptamine in Millipore water was injected and incubated in the chip for 2 h at 60 °C, followed by a rinse of the chip with Millipore water for 5 min.

Assembly of the Sensing Layer on the Microchip Surface. The Eu(III)-EDTA complex was assembled onto the βCD monolayers by incubation of the complex in the microchip for 30 min. This results in immobilization of the Eu(III)-EDTA complex onto the βCD monolayers via orthogonal supramolecular host—guest interactions. Thereafter, naphthalene β-diketone as an antenna in water was injected and incubated for 30 min in the microchip. The self-assembly of the Eu(III)-EDTA conjugate and naphthalene β-diketone resulted in the formation of a highly red luminescent lanthanide system on the microchannel surface via the energy transfer from the antenna to the surface-anchored Eu(III).

Microfluidic Fluorescent Sensing Experiments. Different analytes (phosphates such as ATP, ADP, AMP, pyrophosphate, hydrogen phosphate, and carboxylic acids such as *o/m/p*-phthalic acids, picolinic acid, and dipicolinic acid) in 50 mM HEPES buffer with 50 mM NaCl (pH 7.4) were injected from five inlets with a 1 μl/min flow rate at room temperature at a high-throughput format for turn-off sensing experiments. For high-throughput sensing experiments, all phosphates and carboxylic acids were used at 1 mM concentration. For detection sensitivity experiments, an ATP concentration down to 50 μM and a DPA concentration down to 40 nM was used. The decrease in red emission for each channel in the microchip upon sensing was quantified using a fluorescence microscope using filter R ($\lambda_{\mathrm{em}} = 615$ nm), and a narrow band excitation filter ($300 < \lambda_{exc} < 400$) was used to eliminate direct excitation of analytes such as DPA ($\lambda_{exc} = 270$ nm).

Acknowledgments The major part of the work presented in this chapter was performed in collaboration with Dr. Bilge Eker in the Mesoscale Chemical Systems group of the University of Twente.

References

1. B. Eker, M. Deniz Yilmaz, S. Schlautmann, J.G.E. Gardeniers, J. Huskens, Int. J. Mol. Sci. **12**(11), 7335–7351 (2011)
2. A.L. Jenkins, O.M. Uy, G.M. Murray, Anal. Chem. **71**, 373–378 (1999)
3. P.R. Puopolo, P. Chamberlin, J.G. Flood, Clin. Chem. **38**, 1838–1842 (1992)

4. W.H. van der Schalie, T.R. Shedd, M.W. Widder, L.M. Brennan, J. Appl. Toxicol. **24**, 387–394 (2004)
5. M.F. Rega, J.C. Reed, M. Pellecchia, Bioorg. Chem. **35**, 113–120 (2007)
6. P.J. Hajduk, T. Gerfin, J.M. Boehlen, M. Haberli, D. Marek, S.W. Fesik, J. Med. Chem. **42**, 2315–2317 (1999)
7. M.A. Huestis, M.L. Smith, Drug Discov. Today **3**, 49–57 (2006)
8. E. Fu, T. Chinowsky, K. Nelson, K. Johnston, T. Edwards, K. Helton, M. Grow, J.W. Miller, P. Yager, Ann. N. Y. Acad. Sci. **2007**, 335–344 (1098)
9. A.M. Smith, S. Dave, S. Nie, L. True, X. Gao, Expert Rev. Mol. Diagn. **6**, 232–244 (2006)
10. P. Haas, P. Then, A. Wild, W. Grange, S. Zorman, M. Hegner, M. Calame, U. Aebi, J. Flammer, B. Hecht, Anal. Chem. **82**, 6299–6302 (2010)
11. E. Lester, A. Ponce, IEEE Eng. Med. Biol. **21**, 38–42 (2002)
12. E. D. Lester, G. Bearman, A. Ponce, IEEE Eng. Med. Biol. **23**, 130–135 (2004)
13. J.R. Lakowicz, *Principles of Fluorescence Spectroscopy*, 2nd edn. (Kluwer Academic and Plenum Publishers, New York, 1999)
14. R. Narayanaswamy, O.S. Wolfbeis (eds.), *Optical Sensors: Industrial, Environmental and Diagnostic Applications*, vol. 1 (Springer Series on Chemical Sensors and Biosensors, Berlin, 2004)
15. R. Martinez-Manez, F. Sancenon, J. Fluoresc. **15**, 267–285 (2005)
16. R. Martinez-Manez, F. Sancenon, Chem. Rev. **103**, 4419–4476 (2003)
17. K. Niikura, A. Metzger, E.V. Anslyn, J. Am. Chem. Soc. **120**, 8533–8534 (1998)
18. A. Metzger, E.V. Anslyn, Angew. Chem. Int. Ed. **37**, 649–652 (1998)
19. N.S. Murray, S.P. Jarvis, T. Gunnlaugsson, Chem. Commun. **33**, 4959–4961 (2009)
20. J. Massue, S.J. Quinn, T. Gunnlaugsson, J. Am. Chem. Soc. **130**, 6900–6901 (2008)
21. M.L. Cable, J.P. Kirby, K. Sorasaenee, H.B. Gray, A. Ponce, J. Am. Chem. Soc. **129**, 1474–1475 (2007)
22. K. Ai, B. Zhang, L. Lu, Angew. Chem. Int. Ed. **48**, 304–308 (2009)
23. M.D. Yilmaz, S. Hsu, D.N. Reinhoudt, A.H. Velders, J. Huskens, Angew. Chem. Int. Ed. **49**, 5938–5941 (2010)
24. J.P. Leonard, C.B. Nolan, F. Stomeo, T. Gunnlaugsson, Top. Curr. Chem. **281**, 1 (2007)
25. J.P. Leonard, P. Jensen, T. McCabe, J.E. O'Brien, R.D. Peacock, P.E. Kruger, T. Gunnlaugsson, J. Am. Chem. Soc. **129**, 10986 (2007)
26. T. Gunnlaugsson, F. Stomeo, Org. Biomol. Chem. **2007**, 5 (1999)
27. K. Binnemans, Chem. Rev. **109**, 4283–4374 (2009)
28. R.M. Crooks, A.J. Ricco, Acc. Chem. Res. **31**, 219–227 (1998)
29. A.E. Kaifer, Israel J. Chem. **36**, 389–397 (1996)
30. R. Zimmerman, L. Basabe-Desmonts, F. van der Baan, D.N. Reinhoudt, M. Crego-Calama, J. Mater. Chem. **15**, 2772–2777 (2005)
31. Y.R. Kim, J.J. Kim, J.S. Kim, H. Kim, Adv. Mater. **20**, 4428–4432 (2008)
32. S. Flink, F.C.J.M. van Veggel, D.N. Reinhoudt, Adv. Mater. **12**, 1315–1328 (2000)
33. N.J. van der Veen, S. Flink, M.A. Deij, R.J.M. Egberink, F.C.J.M. van Veggel, D.N. Reinhoudt, J. Am. Chem. Soc. **122**, 6112–6113 (2000)
34. M. Crego-Calama, D.N. Reinhoudt, Adv. Mater. **13**, 1171–1174 (2001)
35. L. Basabe-Desmonts, J. Beld, R.S. Zimmerman, J. Hernando, P. Mela, M.F. Garcia Parajo, N.F. Van Hulst, A. van den Berg, D.N. Reinhoudt, M. Crego-Calama, J. Am. Chem. Soc. **126**, 7293–7299 (2004)
36. C.M. Rudzinski, A.M. Young, D.G. Nocera, J. Am. Chem. Soc. **124**, 1723–1727 (2002)
37. J.M. Berg, J.L. Tymoczko, L. Stryer, *Biochemistry*, 5th edn. (W.H. Freeman, New York, 2002)
38. A. Ojida, I. Takashima, T. Kohira, H. Nonaka, I. Hamachi, J. Am. Chem. Soc. **130**, 12095–12101 (2008)
39. P.D. Beer, P.A. Gale, Angew. Chem. Int. Ed. **40**, 486 (2001)
40. Q. Li, P.K. Dasgupta, H. Temkin, Environ. Sci. Technol. **42**, 2799–2804 (2008)
41. D.A. Henderson, Science **283**, 1279–1282 (1999)

42. M. Enserink, Science **294**, 1266–1267 (2001)
43. P.T. Yung, E.D. Lester, G. Bearman, A. Ponce, Biotechnol. Bioeng. **98**, 864–871 (2007)
44. G.F. Bailey, S. Karp, L.E. Sacks, J. Bacteriol. **89**, 984 (1965)
45. D.R. Walt, Anal. Chem. **72**, 738a–746a (2000)
46. L.J. Rode, J.W. Foster, Nature **188**, 1132–1134 (1960)
47. D.L. Rosen, Rev. Anal. Chem. **18**, 1–21 (1999)
48. P. Mela, S. Onclin, M.H. Goedbloed, S. Levi, M.F. Garcia-Parajo, N.F. van Hulst, B.J. Ravoo, D.N. Reinhoudt, A. van den Berg, Lab Chip **5**, 163–170 (2005)
49. T. Vilkner, D. Janasek, A. Manz, Anal. Chem. **7612**, 3373–3385 (2004)
50. H. Andersson, A. Van den Berg, Sens. Actuators B **92**, 315–325 (2003)
51. H.Y. Fan, F.Y. Lu, A. Stump, S.T. Reed, T. Baer, R. Schunk, V. Perez-Luna, G.P. Lopez, C.J. Brinker, Nature **405**, 56–60 (2000)
52. A. Mulder, J. Huskens, D.N. Reinhoudt, Org. Biomol. Chem. **2**, 3409 (2004)
53. M.J.W. Ludden, D.N. Reinhoudt, J. Huskens, Chem. Soc. Rev. **35**, 1122–1134 (2006)
54. A. Metzger, V.M. Lynch, E.V. Anslyn, Angew. Chem. Int. Ed. **36**, 862–865 (1997)
55. M.J. Berridge, Nature **361**, 315 (1993)
56. N. Shao, J. Jin, G. Wang, Y. Zhang, R. Yang, J. Yuan, Chem. Commun. 1127–1129 (2008)
57. L.J. Charbonniere, R. Schurhammer, S. Mameri, G. Wipff, R.F. Ziessel, Inorg. Chem. **44**, 7151–7160 (2005)
58. S.M. Shanbhag, G.R. Choppin, Inorg. Chim. Acta **139**, 119–120 (1987)
59. Y. Kanekiyo, R. Naganawa, H. Tao, Chem. Commun. 1006–1007 (2004)
60. C. Bazzicalupi, S. Biagini, A. Bencini, E. Faggi, C. Giorgi, I. Matera, B. Valtancoli, Chem. Commun. 4087–4089 (2006)
61. G.V. Zyryanov, M.A. Palacios, P. Anzenbacher Jr, Angew. Chem. Int. Ed. **46**, 7849–7852 (2007)
62. J.P. Kirby, M.L. Cable, D.J. Levine, H.B. Gray, A. Ponce, Anal. Chem. **80**, 5750–5754 (2008)
63. S.L. Wu, W.D. Horrocks Jr, Anal. Chem. **68**, 394–401 (1996)
64. P.R. Ashton, R. Königer, J.F. Stoddart, D. Alker, V.D. Harding, J. Org. Chem. **61**, 903–908 (1996)
65. S.H. Hsu, M.D. Yilmaz, C. Blum, V. Subramaniam, D.N. Reinhoudt, A.H. Velders, J. Huskens, J. Am. Chem. Soc. **131**, 12567–12569 (2009)
66. J. Yuan, K. Matsumoto, Anal. Sci. **12**, 31–36 (1996)
67. J.G.E Gardeniers, R.E. Oosterbroek, A. van den Berg**,** in *Lab-on-a-chip: Miniaturized systems for (bio)chemical analysis and synthesis* (Elsevier, Amsterdam, 2003), pp. 37–64
68. H. Wensink, M.C. Elwenspoek, Wear **253**, 1035–1043 (2002)
69. M.J.W. Ludden, X.Y. Ling, T. Gang, W.P. Bula, H.J.G.E. Gardeniers, D.N. Reinhoudt, J. Huskens, Chem. Eur. J. **14**, 136–142 (2008)

Chapter 6
Local Doping of Silicon Using Nanoimprint Lithography and Molecular Monolayers

Two fabrication schemes for the direct patterning of organic monolayers on oxide-free silicon are reported combining top-down nanoimprint lithography (NIL) and bottom-up monolayer formation. The first approach was designed to form monolayer patterns on the imprinted areas, while the second approach was designed for monolayer formation outside of the imprinted features. By both approaches, covalently bonded Si–C monolayer patterns with feature sizes ranging from 100 nm to 100 μm were created via a hydrosilylation procedure using diluted reagents. This novel patterning strategy was successfully applied for introducing dopant atoms using a phosphorus-containing molecular precursor on oxide-free silicon. The patterned sample was protected by a SiO_2 capping layer applied by e-beam evaporation and subjected to rapid thermal annealing (RTA) to diffuse the phosphorus dopant atoms into the bulk silicon locally. The doped sample was investigated by 3D time-of-flight secondary ion mass spectrometry (TOF–SIMS) and electrically characterized by Hall and Van der Pauw measurements.

6.1 Introduction

A vast amount of semiconductor technology is focused on downscaling electronic components according to Moore's Law [3]. Silicon's semiconducting properties largely depend on the concentration of dopant impurities [4]. Therefore, novel methodologies of selectively introducing dopants to semiconductor materials at the nanometer scale could be beneficiary for the development of smaller integrated circuit (IC) components.

Conventionally, introducing dopant impurities to silicon is achieved using ion implantation [5]. In this process, an ion beam is used to bombard the surface by

Parts of this chapter have been published in Ref. [1, 2]

M. D. Yilmaz, *Orthogonal Supramolecular Interaction Motifs for Functional Monolayer Architectures*, Springer Theses, DOI: 10.1007/978-3-642-30257-2_6,

highly energetic dopant ions, literally shooting the dopants in the top layers of the bulk silicon. True electrical activation is then achieved using a high-temperature annealing step. This fabrication step is required for repairing the—by bombardment inflicted—crystal damage followed by diffusion of (near) surface located dopant atoms.

Fabrication of ultra shallow, heavily doped junctions including well-defined insulating areas will be required for reliably manufacturing smaller scale devices [3, 6, 7]. In this respect, the ability for a true *deterministic* positioning i.e., control over the exact position of impurity atoms in semiconductor structures will become essential. A possible methodology would involve control over lateral (x–y) positioning, concomitant with considerate influence on the penetration depth of dopant diffusion in the z direction from the surface.

In 2008, the group of Javey published a novel method for introducing dopants using molecular monolayers on oxide-free silicon [8]. Using this method, the authors showed it was possible to obtain high level doping of silicon by application of hydrosilylation surface chemistry on Si–H terminated silicon [9, 10] with dopant atom containing organic monolayers. RTA ensures implantation of dopant atoms by diffusion. Using RTA, this method obviates the relatively long annealing steps required to repair damage to the silicon crystal structure. Therefore, a first requirement in *deterministic* positioning of dopant atoms is met, in the sense that, using RTA, dopant atoms mainly end up in the top 100 nm of the silicon substrate. Another benefit of the aforementioned strategy is the use of a limited source, such as a molecular monolayer, which allows specific tuning of the dopant surface dose [8]. Moreover, molecular (self-) assembly is a cheap bottom-up nanofabrication method [11].

Introducing dopants by molecular monolayers, therefore, in principle offers considerable advantages. However, actual device fabrication necessitates combination of the approach of Javey et al. with the ability to selectively pattern and therefore control over the lateral (x–y) positioning of molecular monolayer structures.

Although full, covalently bonded Si–C monolayers are relatively well developed and hold great promise for novel applications, procedures for the nano- or micro structuring of the oxide-free silicon surface remain limited to a few examples. The first report by Effenberger et al. [12] described the generation of patterns on the hydrogen-terminated silicon surface by use of a conventional photomask and UV light. Both neat aldehydes and diluted alkenes were used for monolayer formation, resulting in covalent Si–O–C and Si–C bonds, respectively. In a similar approach by Wojtyk et al. [13], fully hydrogen-terminated samples were partially oxidized in UV light, while pressing a gold raster against the hydrogen-passivated Si(111) surface to shield part of the substrate from the light. After oxidation of exposed features, the remaining hydrogen-terminated areas were further functionalized with a terminal alkene. Cathodic electrografting by STM using 1-alkynes was demonstrated by Hurley et al. [14]. Sub-100 nm patterning by use of catalytic stamp lithography was achieved by Mizuno et al. [15] using palladium nanoparticles. The feature sizes and lateral positioning attainable

with this method are directed by nucleation and growth of the nanoparticles, and sub-20 nm patterning was demonstrated. Recently, sub-80 nm patterns of SiO_2 were obtained by Klingebiel et al. by locally decomposing alkyl monolayers on silicon using photothermal laser processing [16].

These existing procedures suffer from one or more limitations regarding (1) the use of certain reagents (for example, contamination by metals, potentially used as catalysts, needs to be avoided for microelectronic applications), (2) the ability to fabricate well packed layers, (3) the patterning of nanometer-sized features, (4) the control over feature size and position by using arbitrary master structures, and (5) throughput or possibilities for assembly on full wafer scale. Here, we show that monolayer patterns from 100 nm to 100 μm can be successfully created using a combination of top-down and bottom-up fabrication methods: imprint lithography and molecular monolayer formation, respectively. We use thermal NIL [17], a hot embossing technique that is suitable for nanofabrication down to sub-10 nm structures [18] to generate patterns of molecular monolayers on oxide-free silicon. NIL is applicable in both regular lab and clean room conditions, allows relatively high-throughput, and is applicable on full wafer scale. A key characteristic of the thermal NIL process is the use of a thermoplastic polymer as a resist material. In the targeted combined process with monolayer formation on Si, such a resist needs to be resistant against wet fluoride etching, which is used to remove the native oxide, in order that a regular, catalyst-free hydrosilylation procedure can be used for the subsequent monolayer attachment. Two different fabrication schemes are reported by which, using the same imprint mold, monolayer patterns can be obtained, as well as the inverse of these patterns. This novel patterning strategy can be, furthermore, used for the doping of nearly intrinsic silicon using a phosphorus-containing organic precursor.

6.2 Results and Discussion

6.2.1 NIL-Patterned Monolayers on Silicon

Scheme 6.1 outlines two possible approaches toward the structuring of organic monolayers on oxide-free silicon. The first approach (Scheme 6.1a, direct method) typically starts from a clean Si/SiO_2 sample. In step a, the desired polymeric resist material is applied to the sample by spin coating. In steps b (NIL) and c (O_2 plasma etching), the pattern on the mold is transferred into the resist layer. In step d, the exposed SiO_2 areas are subjected to wet etching in aqueous NH_4F, which effectively generates an H-terminated Si surface. The remaining resist is removed (step e), and the monolayer is formed on the Si–H surface areas.

In the second approach (Scheme 6.1b, inverse method), the native oxide layer is completely stripped from the silicon sample by NH_4F (step a), which leaves a H-terminated surface, and a full monolayer is formed on the substrate (step b). The polymeric resist is applied on top of the monolayer by spin coating (step c).

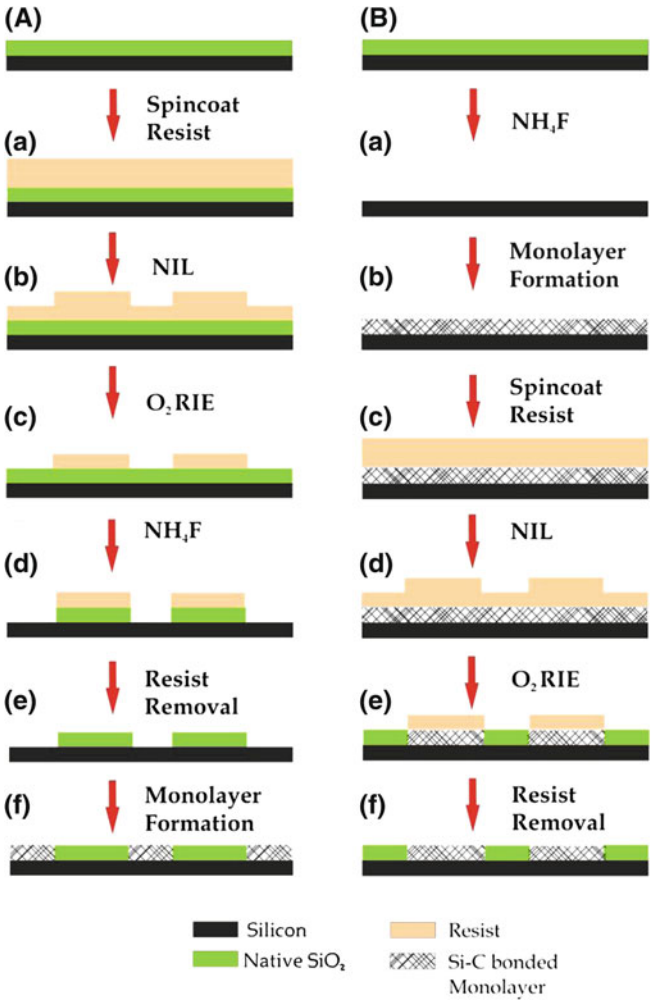

Scheme 6.1 Fabrication routes to the direct (**a**) and inverse (**b**) patterning of monolayers on the Si–H surface

After imprinting (step d), O_2 plasma etching (step e) ensures the removal of both the residual resist layer and the monolayer underneath, and allows for reoxidation of the exposed Si surface areas. Hence, after completion of the pattern transfer procedure by resist removal (step f), the inverse pattern is obtained.

The procedure reported by Sieval et al. [19] was used for all monolayer formation steps by the thermal method using mesitylene as the solvent. Initially, 1-hexadecene was employed as the molecular precursor, since it is known to give stable, well-packed monolayers with a high degree of order, and crystallinity [19–23]. Full monolayers showed, as expected, high advancing water contact

angles ($\theta_A > 111^o$), and their formation was further supported by X-ray photoelectron spectroscopy (XPS; data not shown).

Monolayer patterns with 100 μm features were fabricated using the procedure outlined in Scheme 6.1a (direct method). The feature size was selected to enable pattern characterization by XPS. A layer of resist (10 wt% solution of 350 kD poly(methyl methacrylate) (PMMA) in toluene) was applied by spin coating onto a freshly cleaned Si(111) sample (with the native oxide) and soft-baked in an oven (60 °C, 5 min), resulting in an ellipsometric thickness of around 1,080 nm. The sample was then imprinted (40 bar, 180 °C, 30 min) using a mold with 100 μm diameter pillars separated by 125 μm and with a feature height of 450 nm. Anisotropic reactive ion etching (RIE) with O_2 plasma was performed to remove the residual layer. In order to remove SiO_2 from the exposed surface areas, the sample was subjected for 15 min to a deoxygenated, argon-sparged, 40 wt% NH_4F solution, a procedure known to result in removal of SiO_2 and to yield an atomically flat hydrogen-terminated Si(111) surface [24]. After rinsing with water and drying in a stream of N_2, the remaining PMMA was removed in acetone. The sample was rinsed with deoxygenated water, dried in a stream of N_2, and immediately inserted into a reaction flask together with 1 mL of a deoxygenated solution of 25 % v/v 1-hexadecene in mesitylene. The monolayer was formed under reflux. After cooling and rinsing, physisorbed material was removed by ultrasonication in acetone for 15 min.

To visualize the patterns by XPS, scanning X-ray imaging (SXI) was performed, which provides a secondary electron image with darker and brighter areas corresponding to differences in the amounts of detected backscattered secondary electrons. Also, elemental mapping spectra were generated by scanning over the sample. Figure 6.1a, b shows O_{1s} and Si_{2p} spectra, respectively. Mapping of the high binding energy part of the averaged O_{1s} spectrum resulted in the appearance of a dot pattern (Fig. 6.1a) with the expected feature sizes and period. The bright areas indicate richness in oxygen, corresponding to the presence of SiO_2. Mapping of the Si_{2p} signal was done using the low binding energy part of the spectrum (Fig. 6.1b), which is known to correspond to less oxidized silicon [25], which, thus, signals the presence of silicon and Si–C. Therefore, the bright areas indicate the successful removal of SiO_2 in these areas.

In order to study the stability of the monolayer surface patterns against reoxidation, the sample was stored for 1 month under ambient conditions. The sample was reinspected by XPS. The SXI image (Fig. 6.1c) shows the excellent feature stability. Elemental information was obtained from line scans (Fig. 6.1d). Clear differences in atomic concentrations mark the edges of the dots. Outside of the dots, high signal intensities of Si_{2p} (high energy side, indicating oxygen-rich Si and thus signaling the presence of SiO_2) and an O_{1s} signal were observed, while the C_{1s} signal was higher in the dot areas. These data confirm that the patterned monolayers are still intact.

The direct patterning method (Scheme 6.1a) was subsequently used for the replication of nanoscale features of 150 nm diameter dots. To this purpose, a nickel-plated mold containing a square array of 150 nm pillars in diameter at a 500 nm period with a feature height of 100 nm was imprinted into a 200 nm layer

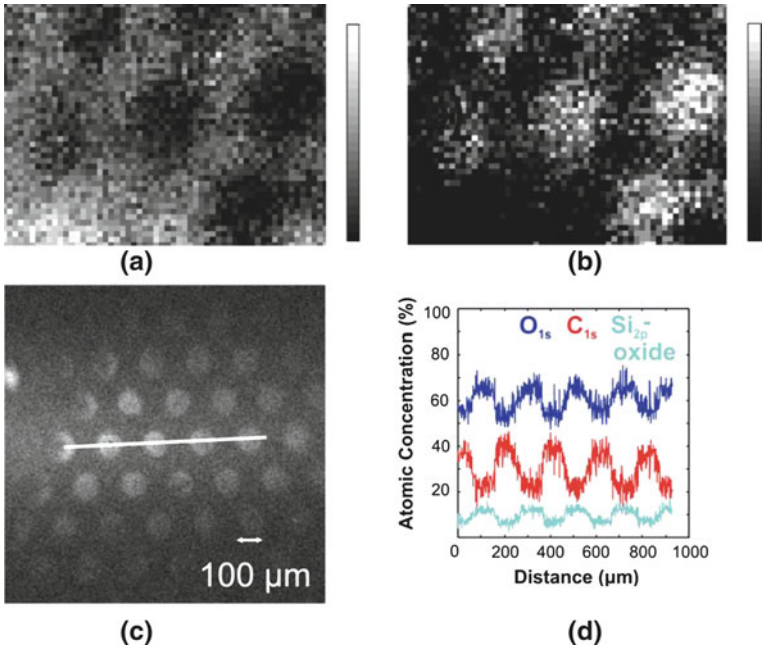

Fig. 6.1 XPS elemental mapping of (**a**) the O_{1s} signal of the high binding energy side and of (**b**) the Si_{2p} signal of the low binding energy side. SXI image (**c**) after 30 days of storage under ambient conditions. The *line* marks the *line* scans reported in panel **d**

of the commercially available resist mr-I 7020E, which was applied by spin coating followed by a short baking step. Residual layer removal was conducted for 90 s.

In an attempt to visualize the pattern and to accurately measure the height of the hexadecyl monolayer, the sample was subjected to an NH_4F etch to remove the residual SiO_2 between the dots. Because of the resistance of alkyl-patterned silicon surfaces against fluoride etching, this etching step should leave the monolayer intact [26, 27]. The pattern was visualized by contact-mode atomic force microscopy (AFM), and a clearly defined pattern was obtained (Fig. 6.2a). The extracted height profile (Fig. 6.2b), however, showed a measured feature height of $\sim$4 nm, while 1.8 nm is expected for a hexadecyl monolayer [23]. A contact-mode AFM height image of a 100 µm dot for which the residual SiO_2 layer was not removed by fluoride etching indicated a height difference of $\sim$2 nm (the SiO_2 area being the higher one), which would indicate a SiO_2 layer with a thickness of $\sim$6 nm. Despite the height difference not yet being fully understood, the pattern quality clearly shows that nanoscale patterning is also possible using this method.

Subsequently, hexadecyl monolayer patterns were fabricated according to the inverse procedure outlined in Scheme 6.1b. To this purpose, a clean Si/SiO_2 sample was fully stripped of its native SiO_2 in aqueous NH_4F (Scheme 6.1b, step a) followed by rinsing with water. Monolayers were formed under thermal conditions as described above (Scheme 6.1b, step b). After rinsing the sample with

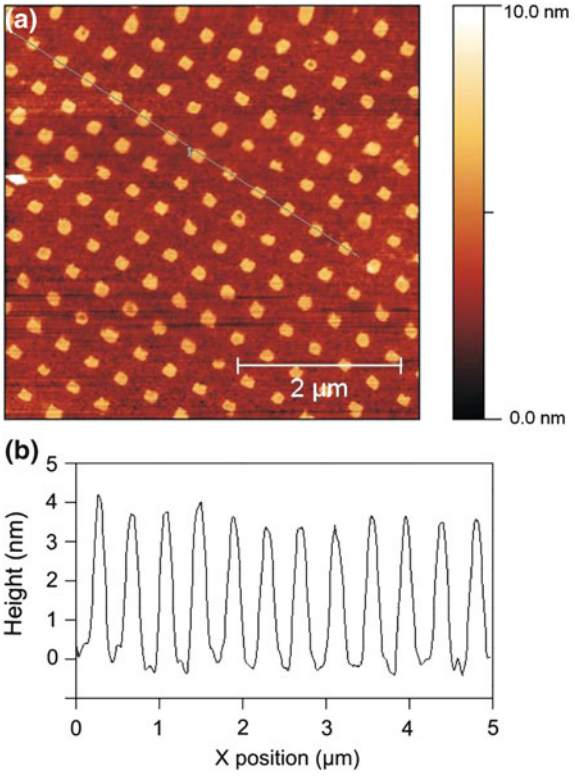

Fig. 6.2 Contact-mode AFM height image (**a**) and corresponding *line* profile (**b**) of a 150 nm diameter dot pattern with a 500 nm period of a hexadecyl monolayer patterned on oxide-free silicon (Scheme 6.1a). The sample was exposed to NH_4F to remove the SiO_2 between the monolayer areas

acetone, ethanol and water, and drying in a stream of N_2, water contact angle measurements indicated the formation of a hydrophobic surface ($\theta_a = 111-113^o$). A 760 nm layer of PMMA was deposited by spin coating and soft-baking for 5 min at 60 °C. The sample was imprinted using a mold containing 3 µm ridges with an 8 µm period with a feature height of 550 nm (40 bar, 180 °C, 15 min, Scheme 6.1b, step d). O_2 plasma etching (3 nm/s for 2 min) ensured removal of the residual layer and the monolayer parts underneath the imprinted features (Scheme 6.1b, step e). The oxygen plasma applied in this etching step is expected to cause immediate reoxidation of the exposed features. Lift-off by ultrasonication in acetone resulted in the final patterned sample (Scheme 6.1b, step f).

Before contact mode AFM imaging, we removed the SiO_2 on the parts not covered with a monolayer by aqueous NH_4F etching. The resulting height image is depicted in Fig. 6.3a. From the corresponding height profile (Fig. 6.3b), we obtained a pattern height of 1.7 nm. This height agrees excellently with the expected 1.8 nm [23].

The same procedure (Scheme 6.1b) was applied to nanometer-scale features. To this purpose, hexadecyl monolayers were prepared in a similar manner, now using a 130 nm resist layer and a master with 100 nm ridges separated by alternating spacings of 3 and 5 µm [28]. O_2 plasma etching and resist removal gave the

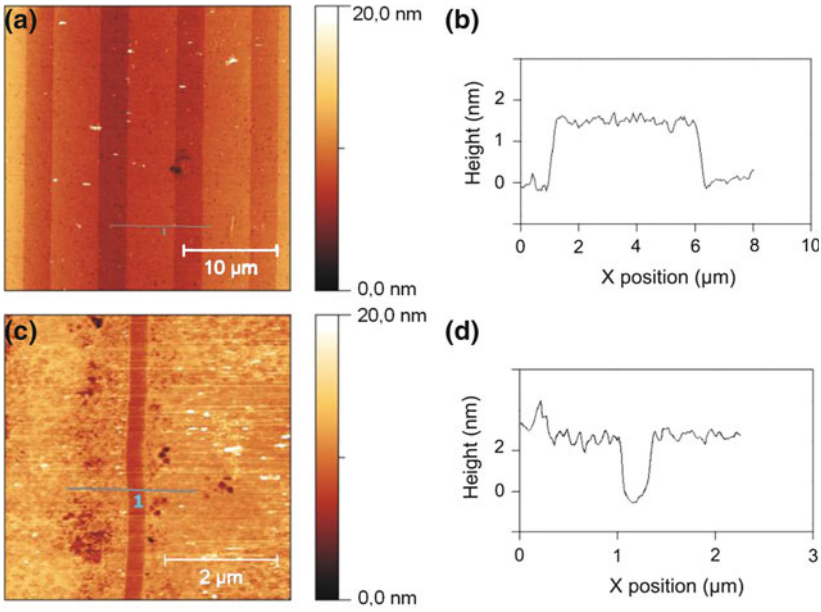

Fig. 6.3 Contact-mode AFM height images (**a**, **c**) and corresponding height profiles (**b**, **d**) of micro- (**a**, **b**) and nano- (**c**, **d**) patterned hexadecyl monolayers, created using the inverse method (Scheme 6.1b). The samples were exposed to aqueous NH_4F before imaging

resulting pattern. Before AFM imaging, the exposed SiO_2 was removed. Figure 6.3c shows the resulting image, and the corresponding line profile is found in Fig. 6.3d. The line width (approximately 200 nm) has increased somewhat compared to the original master, which is attributed to the roundness of the ridges of this particular master, leading to pattern widening upon prolonged etching [28].

The observed height (2 nm) again agrees well with the height of the hexadecyl monolayer. These results show that the inverse method can also be applied to create high-resolution monolayer features on Si. When looking at the heights of the features, the inverse method (Scheme 6.1b) demonstrates a higher degree of reproducibility compared to the direct method (Scheme 6.1a).

To demonstrate the applicability of functional molecules, patterns of a fluorescent dye were prepared. Because of quenching of fluorescence close to the silicon surface [29, 30], we chose a fluorophore based on a boron-dipyrrin (BODIPY) [31] structure known for its high quantum yield [32], and the alkene-terminated derivative *1* (Fig. 6.4a) was synthesized. A full monolayer of *1* was formed in refluxing mesitylene overnight. After monolayer formation, the sample was rinsed with acetone, ethanol, and water. After drying in a stream of N_2, water contact angle measurements ($\theta_a = 91^o$) indicated the formation of a more hydrophobic surface compared to a freshly hydrogen-terminated silicon surface ($\theta_a \sim 78^o$). Line patterns of 100 µm width at 200 µm period were fabricated subsequently, according to the inverse method (Scheme 6.1b).

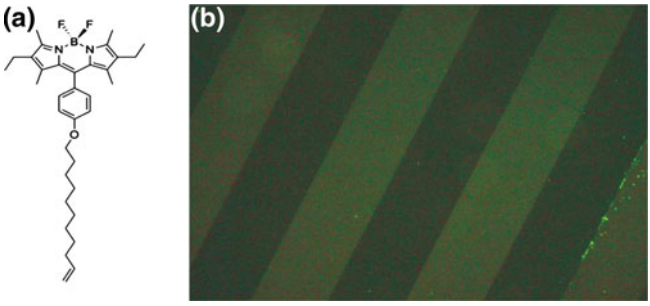

Fig. 6.4 Alkene-terminated BODIPY derivative **1** (**a**) and fluorescence microscopy image (**b**) of 100 μm wide *lines* of **1** fabricated using the inverse method (Scheme 6.1b)

The resulting pattern was imaged by fluorescence microscopy (Fig. 6.4a). The fluorophore is excited at 450–480 nm and emits in the visible green ($\lambda_{ex} \geq 515$ nm). A clear pattern definition is observed. The spacer length (11 carbon atoms, about 1.5 nm) used here is apparently sufficient to observe the pattern. A longer alkyl spacer will likely further reduce quenching by the substrate [29, 30]. These initial results confirm that functional molecules can also be patterned using the methods developed in this study.

6.2.2 *Local Doping of Silicon by NIL-Patterning, Monolayer Formation and RTA*

Using a phosphorus-containing organic precursor, highly doped and patterned (μm-scale) regions in nearly intrinsic silicon were successfully fabricated. These patterned regions were characterized by TOF–SIMS, and by Hal,l and sheet resistance measurements.

Our approach starts with the inverse NIL-patterning method as shown in Scheme 6.1b. In the first step (a) of the process (Scheme 6.2), the sample is fully stripped from its native oxide by NH_4F. In step (b), a full organic monolayer is formed containing dopant atoms. In the next step, imprint resist is spin coated on the preformed monolayer (c). The sample is patterned using NIL in step (d), creating micron size patterns suitable for inspection by SIMS imaging. At the same time, using NIL holds the promise for straightforward extension of the process to the sub-100 nm range by using high resolution molds [24]. RIE using O_2 plasma is used to remove the residual layer and the monolayer underneath in step (e). Resist removal by acetone in step (f) removes residual polymer, which results in pattern transfer. Further, sample processing [steps (g) and (h)] proceed according to the procedure reported by Javey et al. [8]. The specific route [24] in Scheme 6.2 was selected to exclude formation of monolayers on SiO_2-covered areas by reaction with the phosphonate capping group [27].

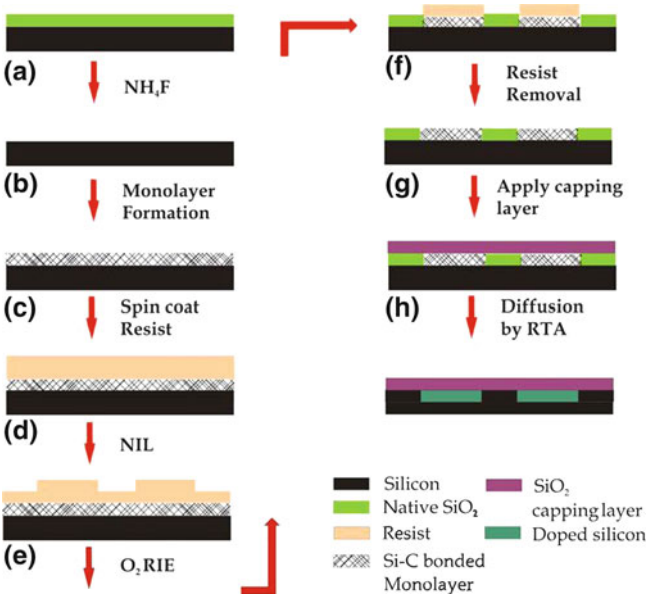

Scheme 6.2 Process scheme for the fabrication of locally doped silicon structures. (**a**) Native SiO_2 is fully stripped by NH_4F. (**b**) Monolayer formation using an organic-dopant atom-containing—molecular precursor. (**c**) Spin coating of the imprint resists. (**d**) NIL. (**e**) RIE of the residual layer and local removal of the monolayer using O_2 plasma, with concomitant oxidation of the exposed Si areas. (**f**) Resist removal by ultrasonication in acetone. (**g**) Deposition of a SiO_2 capping layer by e-beam evaporation. (**h**) RTA to distribute the dopant atoms

Diffusion of the dopant impurities was achieved by RTA for 5 min at 1000 °C (Scheme 6.2h). At this temperature the organic monolayer fully disintegrates and the phosphorus dopant atoms diffuse into the silicon. To analyze the distribution of P dopant atoms in our patterned sample, we used TOF–SIMS for imaging and depth profiling (3D). In Fig. 6.5, each image represents a 500 × 500 μm^2 area.

Integration of these images resulted in lateral line profiles, which are shown in Fig. 6.6. The modulation, calculated by the ratio of high versus low intensity of the signal, shows a value of ~2.5 in the top 0–10 nm which gradually increases up to ~4 from 40–100 nm depth. In Fig. 6.6, the upper (red) curve corresponds to integration of the top left image in Fig. 6.5. The dopant surface dose on a doped area measured $(2.3 \pm 0.1) \times 10^{19}$ P atoms.cm^{-3} corresponding to an areal dose on a doped area of $N_{0,line} = (5.6 \pm 0.1) \times 10^{13}$ P atoms.cm^{-2} (Fig. 6.7a). The exact location of the spot was determined by optical interferometry (Fig. 6.7b). In comparison, on an unpatterned sample that was doped by a full monolayer (RTA, 5 min at 1000 °C), the dopant surface dose after SIMS depth profiling measured $(5.4 \pm 0.1) \times 10^{19}$ P atoms.cm^{-3} which results in an areal dose $N_{0,full\ sample} = (1.1 \pm 0.1) \times 10^{14}$ P atoms.cm^{-2}.

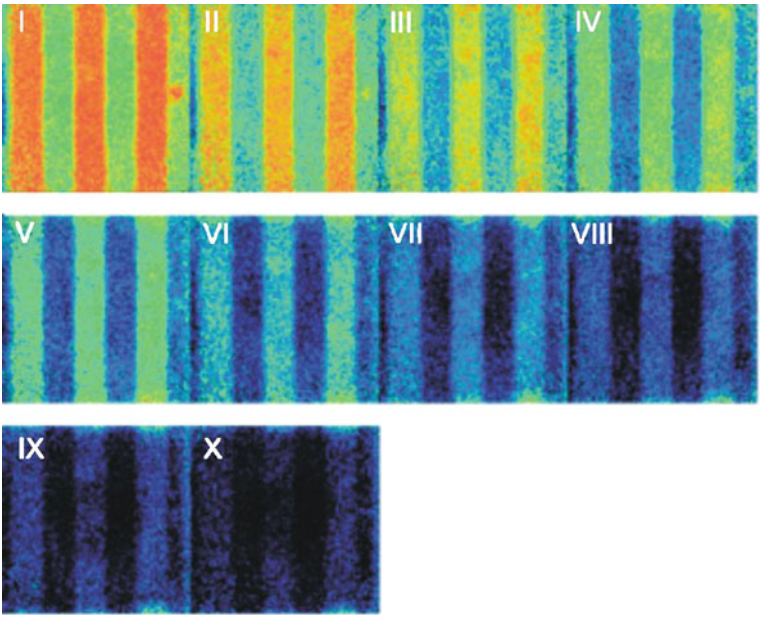

Fig. 6.5 Phosphor elemental images recorded with TOF–SIMS (normalized to Si, image size 500 × 500 μm^2) of a 1 × 1 cm^2 intrinsic Si(100) sample containing 100 μm-wide phosphorus-doped regions at 200 μm period (RTA, 5 min at 1000 °C) at successive depths: each image represents an interval of ∼10 nm (0–10 for image I, 10–20 for image II, etc.)

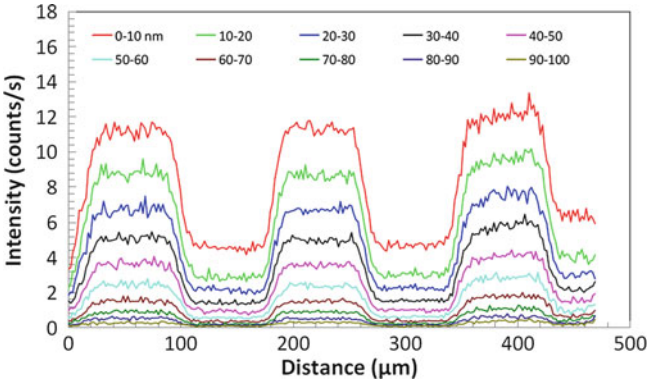

Fig. 6.6 Intensity profiles in *horizontal* direction over the 10 images depicted in Fig. 6.5 (integrated in *vertical* direction. Top 30 and bottom 30 pixels excluded)

A clear resistance difference is observed (Fig. 6.8) between the current measured perpendicular (black curve) and parallel (red curve) to the line orientation. As expected, the perpendicular orientation resulted in the lowest resistance, since the doped lines form a parallel resistor network in this case. With the

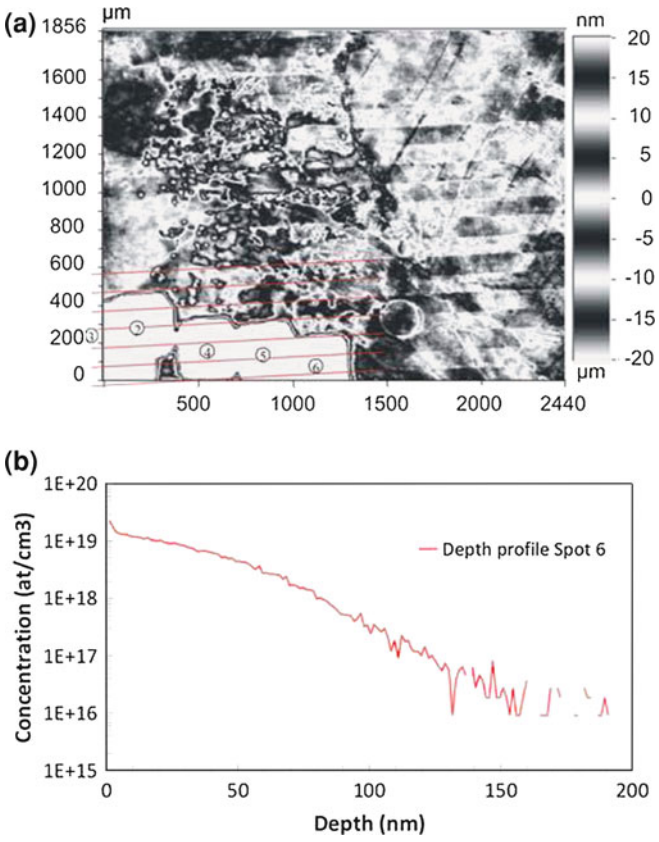

Fig. 6.7 (**a**) Optical profilometry of a sputtered region, (**b**) SIMS depth profile

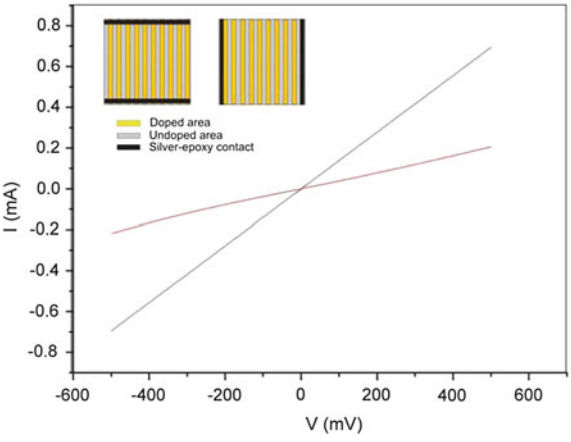

Fig. 6.8 *I–V* measurements on a 1 × 1 cm^2 intrinsic Si(100) sample containing phosphorus, n-doped *line*-shaped regions (width 100 µm, spacing 100 µm), using RTA, 5 min at 1000 °C. For electrical characterization, silver epoxy contact pads were applied perpendicular (*black curve*, inset (a)) or parallel (*red curve*, inset (b)) to the *line* orientation

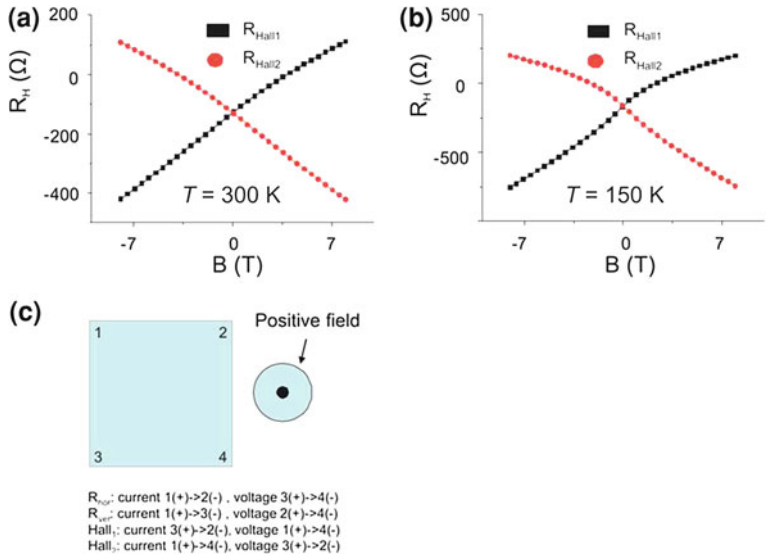

Fig. 6.9 (**a**) Hall resistance measurements at $T = 300$ K on a 1×1 cm^2 intrinsic Si(100) patterned sample phosphorus, n-doped (RTA, 5 min at 1000 °C) (**b**) Hall resistance measurements at alternating negative and positive field on a 1×1 cm^2 intrinsic Si(100) patterned phosphorus n-doped sample at $T = 150$ K (RTA, 5 min at 1000 °C) (**c**) Probe configurations used in Van der Pauw and Hall measurements

contacts oriented parallel to the lines we find a significantly larger resistance (resistors in series).

Hall measurements can provide useful information about the type (electrons or holes) and quantity of the (majority) charge carriers. Deduction of the charge carrier type (Fig. 6.9a, b) revealed electrons as the majority charge carriers, as expected for P implantation. In case of a patterned sample, an *average* sheet carrier density $n_{s,av} = (1.9 \pm 0.1) \times 10^{13}$ cm^{-2} was deduced from the Hall curve in Fig. 6.9a at $T = 300$ K. It must be noted that in the electrical determination of the majority carrier density is averaged over doped and undoped areas on the whole sample, while SIMS depth profiling can be performed on specific locations. As the ratio of doped to undoped areas is 1:1 an estimation for the sheet density on the doped areas of the sample can be obtained by multiplication of the average value by a factor 2 which results in $n_{s,full} = (3.8 \pm 0.1) \times 10^{13}$ cm^{-2}. At $T = 150$ K we determined an average sheet density $n_{s,av} = (9.4 \pm 0.1) \times 10^{12}$ cm^{-2} from the curve in Fig. 6.9b which results in $n_{s,full} = (1.9 \pm 0.1) \times 10^{13}$ cm^{-2}.

The 300 K value ($n_{s,full} = (3.8 \pm 0.1) \times 10^{13}$ cm^{-2}) agrees well with the *local* areal dose as determined by SIMS depth profiling ($N_{0,line} = (5.6 \pm 0.1) \times$P atoms.cm$^{-2}10^{13}$ P atoms/cm^{-2}).

Since the maximum amount of dopant atoms that can diffuse into the silicon is determined by the self-limiting character of organic monolayers, scaling is also expected in terms of sheet resistance *Rs*. For a fully monolayer doped, but

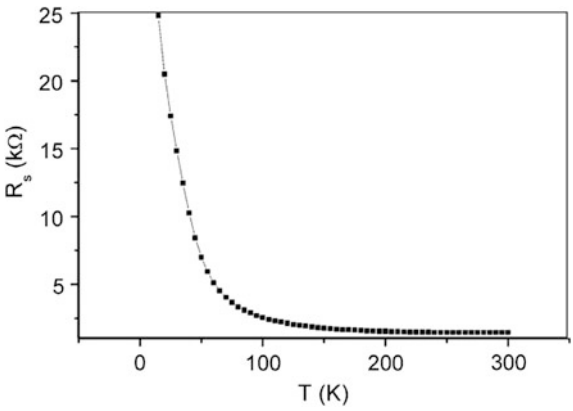

Fig. 6.10 Sheet resistance *Rs* versus *T* by Van der Pauw measurements of a patterned Si sample with 100 µm P-doped line patterns and 100 µm spacing

unpatterned sample we determined $R_s = (7.6 \pm 0.1) \times 10^2$ Ω/□. The average sheet resistance of our patterned sample should naturally be larger and we found $R_s = (1.5 \pm 0.1) \times 10^3$ Ω/□. Since the ratio of line width and spacing is 1:1, also the sheet resistances (by four-point probe measurements) are expected to scale accordingly. $(R_{s,\ unpatterned}/R_{s,\ patterned}) = 0.5$, which corresponds to the expected scaling using a limited source condition such as a molecular monolayer. For an estimated depth of 100 nm for the electrically conductive layer this results in a (bulk) resistivity $\rho = (1.5 \pm 0.1) \times 10^{-2}$ Ω cm for an unpatterned sample, and $\rho = (7.6 \pm 0.1) \times 10^{-3}$ Ω cm for our patterned sample.

The calculated mobility of the majority carrier (μ_m) at $T = 300$ K for our patterned sample was $(2.3 \pm 0.1) \times 10^2$ cm^2 V^{-1} s^{-1} and increased to (3.5 ± 0.1) cm^2 V^{-1} s^{-1} at $T = 150$ K. Figure 6.10 shows a plot of the sheet resistance R_s versus temperature for a patterned sample.

For an estimation of the doping efficiency we use the maximum attainable surface concentration of a full monolayer as determined in the Sect. 6.5 measurement part [$(2.2 \pm 0.1) \times 10^{14}$ P atoms cm^{-2}]. The ratio of the SIMS areal dose to surface concentration × 100 % is the doping efficiency. The areal doses determined by SIMS for a doped line $N_{0,\ line} = (5.6 \pm 0.1) \times 10^{13}$ P atoms cm^{-2} (Fig. 6.7a, b) and $N_{0,full} = (1.1 \pm 0.1) \times 10^{14}$ P atoms cm^{-2} measured on a fully monolayer doped, unpatterned sample were used in the calculation. This results in doping efficiencies of 26 % for a doped line and 50 % on a full sample.

6.3 Conclusions

We have developed two schemes for alkyl monolayer pattern fabrication on oxide free, hydrogen-terminated silicon. To this purpose, top-down NIL was combined with bottom-up formation of molecular monolayers via hydrosilylation. Patterns with feature sizes ranging from 100 nm to 100 µm have been faithfully reproduced. Feature sizes attainable using this method are, in principle, only limited by

the resolution of the NIL mold and by the faithful pattern transfer in the subsequent etching and functionalization steps.

Our work also shows it is possible to fabricate highly doped regions in silicon using a combination of NIL and organic molecular monolayers. By demonstrating proof-of-principle of lateral control over positioning of dopants using molecular monolayer formation we imagine our work can contribute to fabrication of electronic circuitry and devices such as diodes, FETs, or nanowires.

6.4 Experimental Section

Materials. All chemicals were purchased from commercial sources and used as received. Silicon (111) (p-type) was used for patterning experiments. Nearly intrinsic Si(100) (4″, thickness 380 μm, FZ, resistivity between 24.4 and 42.5 k Ω cm^{-1}) was purchased from University Wafer, Boston (MA), USA. Solvents for monolayer formation, rinsing, and SiO_2 etching were deoxygenated by five repetitive cycles of stirring the solution under vacuum followed by argon sparging. Milli-Q water (resistivity >18 M Ω cm) was used in all experiments. 1-Undecenyl-dimethylphosphonate was synthesized according to a literature procedure [33].

Synthesis of alkene-terminated BODIPY derivative 1, (4,4-Difluoro-8-(4-(10-undecenyloxy))phenyl-1,3,5,7-tetramethyl-2,6-diethyl-4-bora-3a,4a-diaza-s-indacene). The synthesis of 4-(10-undecenyloxy)benzaldehyde has been described previously [34]. 3-Ethyl-2,4-dimethyl pyrrole (5.26 mmol, 648 mg) and 4-(10 undecenyloxy)benzaldehyde (2.6 mmol, 713 mg) were dissolved in 200 mL of dry CH_2Cl_2 under argon atmosphere. One drop of trifluoroacetic acid (TFA) was added, and the solution was stirred at room temperature for 3–4 h. At this point, a solution of 2,3-dichloro-5,6 dicyanobenzoquinone (DDQ) (2.6 mmol, 640 mg) in 50 mL dry CH_2Cl_2 was added, and stirring was continued for 30 min followed by the addition of 3 mL Et_3N and 3 mL BF_3. OEt_2. After stirring for 30 min, the reaction mixture was washed three times with water and dried over Na_2SO_4. The solvent was evaporated, and the residue was purified by silica gel column chromatography (1:1 CH_2Cl_2:hexanes) to give a red solid (374 mg, 30 %).

^{1}H NMR (300 MHz, $CDCl_3$) δ 7.14 (d, J = 8.7 Hz, 2H), 6.98 (d, J = 8.7 Hz, 2H), 5.88-5.75 (m, 1H), 5.03-4.86 (m, 2H), 4.01 (t, J = 6.6 Hz, 3H), 2.52 (s, 6H), 2.30 (q, J = 7.5 Hz, 4H), 2.05 (q, J = 7.2 Hz, 2H), 1.83 (p, J = 6.9 Hz, 2H), 1.47-1.25 (m, 24H) ^{13}C NMR (75 MHz, $CDCl_3$) δ 159.7, 153.6, 140.6, 139.4, 138.7, 132.8, 131.4, 129.6, 127.8, 115.1, 114.3, 68.3, 34.0, 29.9, 29.7, 29.6, 29.5, 29.3, 29.1, 26.3, 17.3, 14.9, 12.7, 12.1 MS (ESI) calcd for $C_{34}H_{47}BF_2N_2O$ (M + H) 549.37; found 549.6.

Substrate and monolayer preparation. Si substrates were cleaned by immersion in Piranha solution (concentrated H_2SO_4: 33 % H_2O_2=3:1 v/v. CAUTION! Piranha solutions should be handled with great care in open containers in a fume hood. Piranha is highly corrosive and toxic and potentially explosive) for 30 min.

Cleaned substrates were rinsed with Milli-Q water and blown dry in a stream of nitrogen. A hydrogen-terminated silicon (111) surface was generated by immersion of the substrate in an argon-sparged 40 wt% aqueous NH_4F solution for 15 min followed by extensive rinsing with Milli-Q water and drying in a stream of nitrogen.

Monolayers were assembled on Si(111) using the literature procedure of Sieval et al. [19] with minor changes. Monolayers were formed in all experiments using diluted reagents as the molecular precursor in refluxing mesitylene (bp = 166 °C) as the solvent. Glassware was predried with a heat gun at 200 °C for 15 min. A small three-necked flask was equipped with a reflux cooler. The other inlets were sealed with a rubber septum. A long needle serving as the nitrogen inlet was inserted through the septum in one of the inlets. Under vigorous N_2-flow, freshly hydrogen-terminated samples were inserted. Deoxygenated reagents and solvents were taken up through a septum by a syringe and subsequently transferred to the reaction vessel, after which the needle was placed just above the solution. The nitrogen flow was reduced to a minimum to reduce evaporation of liquids. A metal bath at 180 °C was used to heat the flask containing the samples. After monolayer formation (2.5 h for the hexadecyl functionalized layers, and overnight for fluorescent molecule *1*), the samples were rinsed with ethanol, acetone and Milli-Q water, and ultrasonicated for 15 min in acetone to remove physisorbed material.

Nanoimprint Lithography. Silicon molds for NIL were prepared by e-beam writing or by using standard photolithographic methods followed by RIE using an Electrotech Twin system PF 340. Mold 1 consisted of a hexagonal pattern of 100 μm pillars in diameter with a height of 450 nm. Mold 2 consisted of 3 μm ridges at 8 μm period with a height of 550 nm. Mold 3 was purchased from NIL Technology, Denmark, which was a nickel-plated mold and consisted of a square array of 150 nm pillars in diameter at 500 nm period with a height of 100 nm. Mold 4 consisted of 100 nm wide ridges at alternating periods of 3 and 5 μm with a feature height of 110 nm made by edge lithography [28]. Mold 5 consisted of 100 μm wide trenches at 200 μm period with a height of 125 nm. Before use, molds 1, 2, 4, and 5 were coated with an antisticking layer by gas phase deposition of 1H,1H,2H,2H perfluorodecyltrichlorosilane (PFDTS) [35] overnight followed by a 30 min bake at 120 °C. Polymerized materials were removed from the silanized silicon molds by ultrasonication for 5 min in acetone.

A resist layer of PMMA (Mw = 350 kD) (molds 1, 2, 4 and 5) or commercially available resist (mr-I 7020E, micro resist technology, GmbH) (mold 3) was applied by spin coating on a cleaned Si/SiO_2 surface (Scheme 5.1a) or on a preformed monolayer on Si (Scheme 5.1b).

For imprinting, mold, and substrate were contacted at 40 bar pressure using a hand-press (Specac) at 180 °C (PMMA) or at 130 °C (mr-I 7020E). Residual layer removal was achieved by (anisotropic) RIE on a Electrotech Twin system PF 340 using O_2 plasma.

Doping of silicon by molecular monolayers was achieved as previously described [8]. A thin film of SiO_2 ($\sim$100 nm) was deposited by e-gun evaporation of SiO_2 pellets of 1–5 mm in diameter (Kurt Lesker) using a Balzers BAK 600

apparatus operating at a base pressure of 2e-6 bar. By RTA, the distribution of the dopant atoms was achieved using an Amtech Tempress Omega Junior 2-stack oven at 1000 °C for 5 min in a N_2- atmosphere. After cool down of the samples the template SiO_2 layer was stripped off using buffered HF.

Measurements

Water contact angles were determined using a Kruss Contact Angle Measurement System G 10, and the data were processed using the Drop Shape Analysis 1.51 program. Contact angle measurements were taken on three different points on the sample, and the results were averaged. Resist film thicknesses were measured using a Plasmos SD 2002 ellipsometer at $\lambda = 632.8$ nm. XPS was performed using a Physical Electronics Quantera SXM equipped with an Al Kα monochromatic excitation source (source energy = 1486.6 eV, take-off angle set at 45°). SXI images were collected using these settings or using an X-ray beam down to 4.5 W per 18 μm. The X-ray beam was set to 1 W per 9 μm for line scans (Fig. 6.1c) across 4.5 dots for 16 h (298 K, $<8 \times 10^{-9}$ Torr). SIMS measurements were performed using a Cameca ims6f magnetic-sector SIMS and an Ion-Tof TOF–SIMS IV instrument. The Cameca was operated in positive mode with 3 keV O_2^+ primary ions and additional O_2-flooding to enhance the P^+ secondary ion yield. The TOF–SIMS was also operated in positive mode and O_2- flooding; the primary ions were 2 keV O_2^+ for sputtering and 25 keV Bi^+ for analysis.

The samples have also been inspected using optical profilometry to measure crater depths for depth scale calibration and to visualize the line pattern.

Images in Fig. 6.5 were collected after sputtering of the top 2 nm to remove redeposited physisorbed materials. The utmost edges of the images should be ignored, since they are sputtered slower, resulting in erroneously higher *P* concentration.

Determination of the Hall-coefficient was done using a Quantum Design Physical Property Measurement System (PPMS) using PPMS Multivu software. The system was configured with an 8 T strength longitudinal magnet. Measurements were conducted at temperatures from 293 K down to 10 K. Samples were subjected to wafer bonding for attachment to the sample holder for measurements.

Introduction of impurities with a higher atomic valence than silicon in the crystal lattice is expected to result in a majority of charge carriers which is negative ($R_H < 0$). Figure 6.9c shows our used setup and configuration of measurement probes. For the black curve in Fig. 6.9(a, b) the configuration of the probes is as follows: 3(+), 2(−), 1(+), 4(−). The current flows from contact 3 to contact 2 because of the higher potential of contact 3. Application of the right-hand rule shows that the Lorentz force tends to accumulate electrons at contact 1 at positive field. This effect causes an increase in potential at contact 1. Measurement of the voltage difference between contacts 1 and 4 should therefore result in a positive Hall coefficient since the voltage difference (V1–V4) is also positive. This is exactly what is expected for electrons as the majority charge carrier.

For resistance measurements over parallel lines (Fig. 6.3, inset) contact pads were applied along a 1×1 cm^2 sample perpendicular to the pattern direction

using a silver epoxy paste. A thin line of paste of approximately 1 mm in width was applied along the edge of each side of the sample on the hydrogen-terminated silicon surface. The samples were shortly annealed at 120 °C for 30 min and stored overnight. Resistances over the samples were determined using a two-point probe IV-measurement using a Keithley 4,200 Semiconductor characterization system. In our case, using a 0.9 × 0.9 cm^2 mold for imprint approximately 45 parallel wires were measured of 100 μm in width separated by 100 μm spacings. As a control measurement, the contact pads were stripped by immersion of the samples for 30 min in fuming HNO_3 and reapplied parallel to the direction of our doped pattern after which the resistance over the sample in opposite direction was determined.

To determine the dopant surface dose, the maximum number of $=SiH_2$ sites available on the Si(100) surface based on the dimension of a unit cell (14.74 $Å^2$) [26]. Based on this value a molecular density of 6.7 × 10^{14} molecules cm^{-2} is calculated. However, only a maximum of 61 % surface coverage can be obtained due to sterical constraints of the alkyl chains. The maximum molecular density which can be obtained on Si(100) therefore is 4.1 × 10^{14} molecules cm^{-2}. Such an ideal coverage of the surface only proceeds when using long chain alkyl terminated monolayers and Faucheux et al. [36] determined for acid-terminated (−COOH) undecenyl moieties a surface coverage of 0.32 on Si(111). Therefore, it is expected that for monolayers prepared using 1-undecenyl-dimethylphosphonate, a compound with an even bulkier head group, the surface coverage will not extend 0.32. Therefore, based on this surface coverage factor we estimate a maximum molecular density of 2.2*10^{14} molecules cm^{-2}. With a ratio of one phosphorus atom per precursor molecule the molecular density can directly be compared to the areal doses extracted from SIMS measurements to obtain the doping efficiency.

Fluorescence microscopy

Fluorescence microscope images were taken using an Olympus inverted research microscope IX71 equipped with a mercury burner U-RFL-T as light source and a digital Olympus DR70 camera for image acquisition. Blue excitation (450 nm $\leq \lambda_{ex} \leq$ 480 nm) and green emission ($\lambda_{em} \geq$ 515 nm) was filtered using a Dapi Olympus filter cube. All fluorescence microscopy images were acquired in air.

Atomic force microscopy

AFM imaging was performed using an AFM Nanoscope III, (Veeco Digital Instruments, U.S.A.) in contact mode equipped with a Si_3N_4 tip with a J-scanner at a scan rate of 1.5 Hz.

Acknowledgments The major part of the work presented in this chapter was performed in collaboration with W. Pim Voorthuijzen. Alberto Gomez-Casado is acknowledged for performing the AFM measurements. Y. Zhao is acknowledged for preparation of the 100 nm ridge mold. Dr. J.G.M. van Berkum (MiPlaza Materials Analysis, Eindhoven, and the Netherlands) is acknowledged for SIMS characterization.

References

1. W. Pim Voorthuijzen, M. Deniz Yilmaz, G.-C. Alberto, J. Pascal, Wilfred G. van der Wiel, J. Huskens, Langmuir **26**, 14210–14215 (2010)
2. W. Pim Voorthuijzen, M. Deniz Yilmaz, J.B. Wouter Naber, H. Jurriaan, Wilfred G. van der Wiel, Adv. Mater. **3**, 1346–1350 (2011)
3. P.S. Peercy, Nature **406**, 1023–1026 (2000)
4. M. Lundstrom, Science **299**, 210–211 (2003)
5. H.J. Queisser, E.E. Haller, Science **281**, 945–950 (1998)
6. D.H. Lee, J.W. Mayer, Proc. IEEE **62**, 1241–1255 (1974)
7. A. Renau, Nucl. Instr. Meth. Phys. Res. B **237**, 284–289 (2005)
8. J.C. Ho, R. Yerushalmi, Z.A. Jacobson, Z. Fan, R.L. Alley, A. Javey, Nat. Mater. **7**, 62–67 (2008)
9. J.M. Buriak, Chem. Commun., 1051–1060 (1999)
10. J.M. Buriak, Chem. Rev. **102**, 1271–1308 (2002)
11. R.T. Lee, R.I. Carey, H.A. Biebuyck, G.M. Whitesides, Langmuir **10**, 741–749 (1994)
12. F. Effenberger, G. Gotz, B. Bidlingmaier, M. Wezstein, Angew. Chem. Int. Ed. **37**, 2462–2464 (1998)
13. J.T.C. Wojtyk, M. Tomietto, R. Boukherroub, D.D.M. Wayner, J. Am. Chem. Soc. **123**, 1535–1536 (2001)
14. P.T. Hurley, A.E. Ribbe, J.M. Buriak, J. Am. Chem. Soc. **125**, 11334–11339 (2003)
15. H. Mizuno, J.M. Buriak, J. Am. Chem. Soc. **130**, 17656–17657 (2008)
16. B. Klingebiel, L. Scheres, S. Franzka, H. Zuilhof, N. Hartmann, Langmuir **26**, 6826–6831 (2010)
17. L.J. Guo, J. Phys. D Appl. Phys. **37**, R123–R141 (2004)
18. S.Y. Chou, P.R. Krauss, P.J. Renstrom, Science **272**, 85–87 (1996)
19. A.B. Sieval, V. Vleeming, H. Zuilhof, E.J.R. Sudholter, Langmuir **15**, 8288–8291 (1999)
20. A. Ulman, Chem. Rev. **96**, 1533–1554 (1996)
21. F. Schreiber, Prog. Surf. Sci. **65**, 151–256 (2000)
22. X.-M. Li, J. Huskens, D.N. Reinhoudt, J. Mater. Chem. **14**, 2954–2971 (2004)
23. M.R. Linford, P. Fenter, P.M. Eisenberger, C.E.D. Chidsey, J. Am. Chem. Soc. **117**, 3145–3155 (1995)
24. W.P. Voorthuijzen, M.D. Yilmaz, A. Gomez-Casado, P. Jonkheijm, W.G. Van der Wiel, J. Huskens, Langmuir **26**, 14210 (2010)
25. A.B. Sieval, A.L. Demirel, J.W.M. Nissink, M.R. Linford, J.H. van der Maas, W.H. de Jeu, H. Zuilhof, E.J.R. Sudholter, Langmuir **14**, 1759–1768 (1998)
26. A.B. Sieval, R. Linke, H. Zuilhof, E.J.R. Sudholter, Adv. Mater. **12**, 1457–1460 (2000)
27. R. Yerushalmi, J.C. Ho, Z. Fan, A. Javey, Angew. Chem. Int. Ed. **47**, 4440 (2008)
28. Y. Zhao, E. Berenschot, M. de Boer, H. Jansen, N. Tas, J. Huskens, M. Elwenspoek, J. Micromech. Microeng. **18**, 064013 (2008)
29. A. Lambacher, P. Fromherz, Appl. Phys. A Mater. Sci. Process. **63**, 207–216 (1996)
30. T. Lasseter, B.H. Clare, B.M. Nichols, N.L. Abbott, R.J. Hamers, Langmuir **21**, 6344–6355 (2005)
31. BODIPY is a registered trademark of Molecular Probes, Inc
32. M.D. Yilmaz, O.A. Bozdemir, E.U. Akkaya, Org. Lett. **8**, 2871–2873 (2006)
33. R.T. Lee, R.I. Carey, H.A. Biebuyck, G.M. Whitesides, Langmuir **10**, 741 (1994)
34. G.S. Lee, Y.-J. Lee, S.Y. Choi, Y.S. Park, K.B. Yoon, J. Am. Chem. Soc. **122**, 12151–12157 (2000)
35. G.S. Ferguson, M.K. Chaudhury, H.A. Biebuyck, G.M. Whitesides, Macromolecules **26**, 5870–5875 (1993)
36. A. Faucheux, A.C. Gouget-Laemmel, C.H. de Villeneuve, R. Boukherroub, F. Ozanam, P. Allongue, J.-N. Chazalviel, Langmuir **22**, 153–162 (2006)

Chapter 7
Fabrication of Two-Dimensional Organic Spin Systems on Gold

In this chapter, fabrication of monolayers of organic molecules with unpaired spins on a thin gold film is described. XPS and cyclic voltammetry (CV) measurements showed the existence of unpaired spins on gold surface. In a number of systems with diluted monolayers, electrical transport measurements showed an increase of the gold film sheet resistance for temperatures below $\sim$20 K for some examples, possibly implying Kondo physics.

7.1 Introduction

The electronic interaction of magnetic impurities with their environment can lead to a spin phenomenon. This is a physical phenomenon and widely studied in condensed matter physics. The effect arises from the interactions between a single magnetic atom, such as cobalt, and the many electrons in an otherwise nonmagnetic metal such as copper. Such an impurity, typically has an intrinsic angular momentum or spin that interacts with all the surrounding electrons in the metal. The Kondo effect is named after the Japanese physicist Jun Kondo, who in 1964 gave an explanation for this physical phenomenon [2–10]. This phenomenon is characterized by an anomalous temperature dependence of the resistivity. Usually, the electrical resistivity of a pure metal decreases as its temperature drops. This is because the lattice vibrations (phonons) diminish, and conduction electrons can travel more easily through the crystal. This decrease usually saturates at a certain temperature due to (static) impurities in the material, which cause scattering of the conduction electrons, even at the lowest attainable temperatures. A higher amount of impurities results in a higher saturation resistivity. However, De Haas et al. observed a resistivity increase of gold samples with decreasing temperature below

Part of this chapter has been published in Ref. [1]

M. D. Yilmaz, *Orthogonal Supramolecular Interaction Motifs for Functional Monolayer Architectures*, Springer Theses, DOI: 10.1007/978-3-642-30257-2_7,

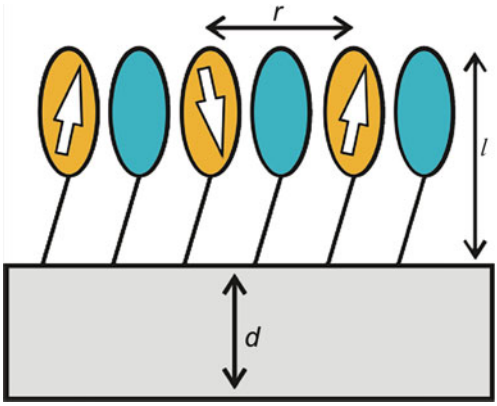

Fig. 7.1 Schematic representation of a 2D spin system used in this project to investigate spin phenomena. It consists of a metal substrate with a monolayer of organic molecules with (*orange*) or without (*blue*) an unpaired spin

4 K. This discovery was followed by many observations of increasing metal resistivity below a certain temperature. It was proven that this observed resistivity minimum was caused by the presence of diluted magnetic impurities, which are impurities with a local magnetic moment caused by the spin of unpaired electrons [11].

In this chapter, we propose and investigate a possible Kondo system which consists of a thin gold layer, with on top a self-assembled monolayer (SAM) of molecules having an unpaired spin, which are the magnetic impurities in the system. Because of this unpaired spin, these molecules have a net magnetic moment and therefore behave as magnetic impurities on top of the metal substrate. The 2D spin systems theoretically offer the opportunity to investigate the interaction between the magnetic molecules on top of the substrate and the conduction electrons inside the metal film. This interaction leads to Kondo effect which can be macroscopically observable (typically through resistance change at liquid helium temperatures). In order to observe the Kondo effect, electrons must be able to tunnel on and off the magnetic impurity molecules. A schematic representation of a 2D spin system is given in Fig. 7.1. It shows a thin metal film covered with a monolayer of organic molecules with unpaired spins. By varying the concentration of these molecules, the average distance between the unpaired spins may be varied. In this way, the interaction between the unpaired spins (RKKY mechanism, the interaction of the spin of two magnetic ions) can be influenced [12–14]. When the unpaired electrons are separated further from each other, the RKKY coupling will decrease. Since a strong RKKY coupling locks the spins of the electrons, spin-flip scattering cannot occur anymore and the Kondo effect will be suppressed. This means that the 2D spin systems offer a method for studying the transition between the Kondo effect and the RKKY interaction by varying the concentration of the molecules with an unpaired spin. Another variable that can be investigated is the length over which the unpaired spin can interact with the conduction electrons. This can be done by varying the length of the molecules l and therefore the distance of the unpaired spins from the surface. The final variable that can be changed is the thickness of the substrate. The thinner the substrate becomes, the larger the ratio of conduction electrons that contribute to the Kondo effect becomes.

Therefore, the focus will be on the characterization of the 2D hybrid spin systems on gold substrate. Using molecules carrying unpaired spins as elements of computer circuits, electronic and optical switches, sensors, and for charge storage is a powerful new direction in the science and technology of nanometer scale complex systems.

7.2 Result and Discussion

7.2.1 Monolayer Fabrication and Characterization

Terpyridine ligands and their metal complexes used in this study were synthesized according to the literature procedure [15]. As the use of thiols for SAMs on gold is well known, all compounds were used for direct functionalization on gold. The monolayers were formed by simple dipping of the gold substrate in a typically 1 mM of compounds in acetonitrile solution overnight at room temperature. The molecules that we have investigated are depicted in Fig. 7.2.

The monolayer formation was initially characterized by X-ray photoelectron spectroscopy (XPS). XPS measurements identified the cobalt ion in the monolayer as Co^{2+} oxidation state (Fig. 7.3). The two main peaks at 781.3 and 796.3 eV, corresponding to the $Co2p_{3/2}$ and $Co2p_{1/2}$ state, respectively, are representative for a system with a Co^{2+} ion in an octahedral structure [16]. The satellite peaks are associated with outer-shell excitations parallel to the photoionization of an inner-shell electron, which disturbs the central potential. In XPS spectrum, the satellite peaks of $Co2p_{3/2}$ and $2p_{1/2}$ are 787.3 and 802.3 eV, respectively, which are in perfect agreement with the literature values (octahedrally coordinated Co^{2+} ions have about 6.2 eV satellite splittings of both $Co2p_{3/2}$ and $Co2p_{1/2}$ levels) [17]. For a full monolayer of zinc complex, only one peak was observed at 1022 eV as shown in Fig. 7.4.

To confirm the oxidation state of the terpyridinyl-cobalt complex SAM in the monolayer, CV measurements were performed on gold substrate. Figure 7.5 illustrates the CVs of terpyridinyl-Co complex in CH_3CN with 0.1 M $NaClO_4$ on gold as a function of scan rate. The voltammetric waves with the symmetric shape anticipated for a surface-confined redox process. Monolayer showed a typical reversible electrochemical reaction, with an oxidation peak at 0.22 V corresponding to the $Co^{3+/2+}$ process, which is in perfect agreement with literature values [15, 16]. The electron transfer kinetics could be determined by plotting the peak current, I_p versus the scan rate, v (Fig. 7.6). A linear correlation was obtained, with a slope of $\sim$1.0. It indicates that the nature of redox process is controlled in a diffusionless manner (surface-confined process) [18].

7.2.2 Electrical Characterization

This part of the chapter describes the resistance measurements of gold thin films covered with monolayers of terpyridinyl-metal complexes. Measurements were

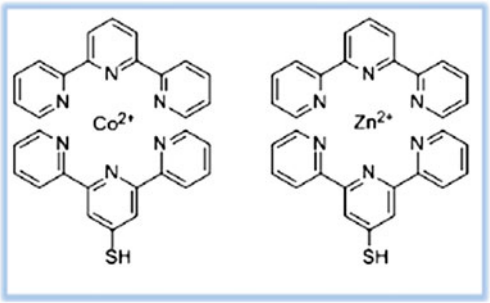

Fig. 7.2 Chemical structures of complexes used in this study

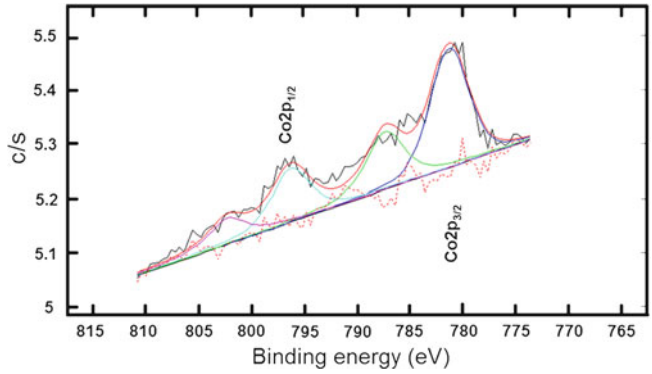

Fig. 7.3 XPS spectrum (intensity *c/s* vs. binding energy) of terpyridinyl-Co complex. The two peaks at 781.3 and 796.3 eV correspond to $Co2p_{3/2}$ and $Co2p_{1/2}$ states

carried out with the cryogenic measurement equipment by Wouter Naber in Nanoelectronics group of University of Twente.

Van der Pauw measurement technique was used to determine the sheet resistance Rs of gold samples. After self-assembly of the monolayer, the substrate is wire-bonded at the four corners and measured with a physical properties measurements system (PMMS) of Quantum Design [19]. With these four contacts, Hall measurements can also be performed, to determine the charge carrier density in samples to see whether this is influenced by the SAM formation. Hall measurements in all samples give a carrier density in the Au of $\sim 5.2 \times 10^{28}$ m^3, close to the value of bulk Au ($\sim 5.9 \times 10^{28}$ m^3), showing the quality of Au layers and the fact the Au is unaffected by the self-assembly process.

The measurements described in this section have been performed on Si/SiO_2 (~ 1 nm) substrates covered with a 10 nm thick Au layer. The Au layers were cleaned with acetone and 2-propanol, and then with piranha solution before SAM formation. Different samples with different ratios of terpyridinyl-Co complex and terpyridinyl-Zn complex are measured. Although it was not expected that this

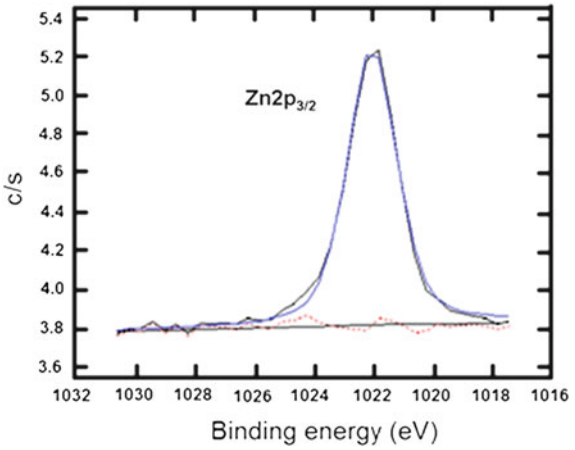

Fig. 7.4 XPS spectrum (intensity *c/s* vs. binding energy) of terpyridinyl-Zn complex. The peak at 1022 eV corresponds to $Zn2p_{3/2}$ state

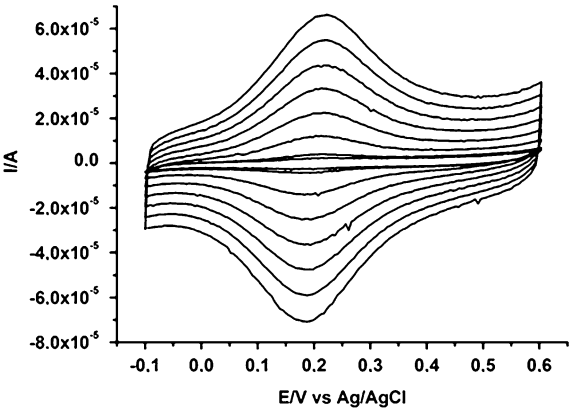

Fig. 7.5 Cyclic voltammogram of SAM prepared from terpyridinyl-Co complex in 0.1 M $NaClO_4/CH_3CN$ at scan rates varying from 0.075 to 0.7 V/s

would give absolute control over the concentration of the complexes in the monolayer, it would at least result in a smaller concentration of Co-complex on the gold surface and hence a lower interaction among the terpyridinyl-Co complexes (e.g., a reduced RKKY interaction). We fabricated samples with only Co-complex, only Zn-complex, and both Co- complex and Zn-complex in the ratios 1:1000, 1:5000, and 1:10000. The given ratios are the ratios used in the solutions prior to the self-assembly. Temperature-dependent measurements of the sheet resistance R_s of 10 nm Au layers covered with SAMs are shown in Fig. 7.7. It clearly shows that in case of only Co-complex, Zn-complex, and Co:Zn ratio of 1:10000, the resistance saturated with decreasing temperature below 10 K, which was expected because of the lack of paramagnetic molecule for only Zn, strong RKKY interaction between spins for only Co-complex, and very low concentration of Co-complex for 1:10000 diluted sample. However, the samples with Co:Zn ratios of 1:1000 and 1:5000, this time, showed a relative resistance rise of several percent (compared to the minimum sheet resistance) and for approximately 40 % of the

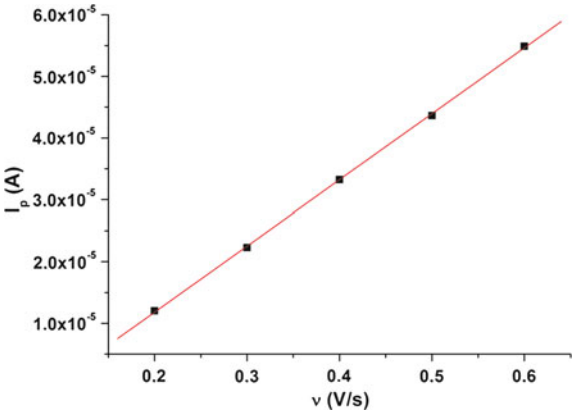

Fig. 7.6 Plot of the oxidation peak current, I_p, versus scan rate, v

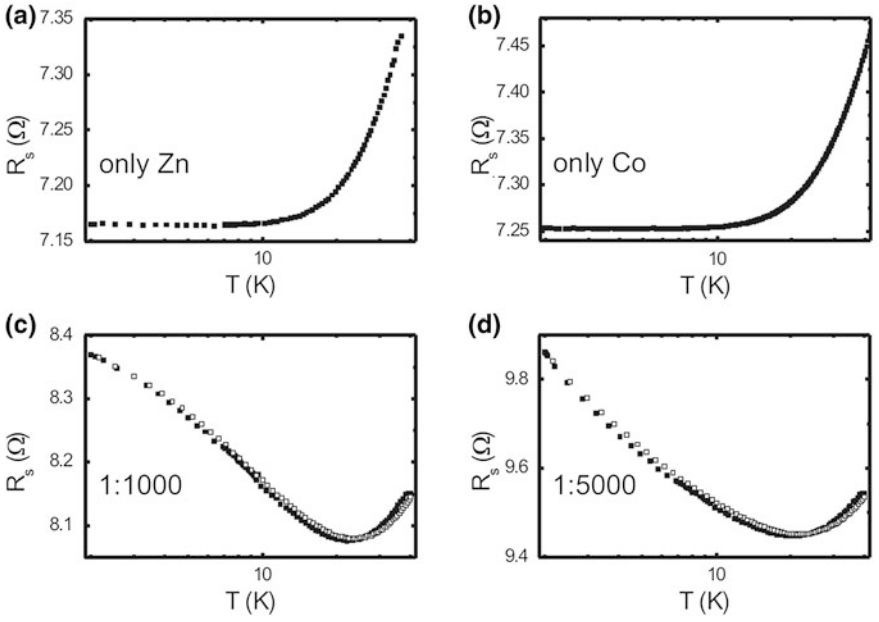

Fig. 7.7 Sheet resistance R_s versus temperature T for samples with a 10 nm Au layer covered with a SAM consisting of **a** only Zn-complex, **b** only Co-complex and Co- and Zn-complexes in the ratio, **c** 1:1000, **d** 1:5000, showing a resistance increase, without (*filled squares*) and with (*open circles*) a magnetic field

measured samples. One of the samples with a ratio of 1:5000 was measured at lower temperatures, down to ~0.27 K, as shown in Fig. 7.8. Temperature is plotted on a logarithmic scale, which clearly shows the logarithmic increase between 0.5 and 5 K.

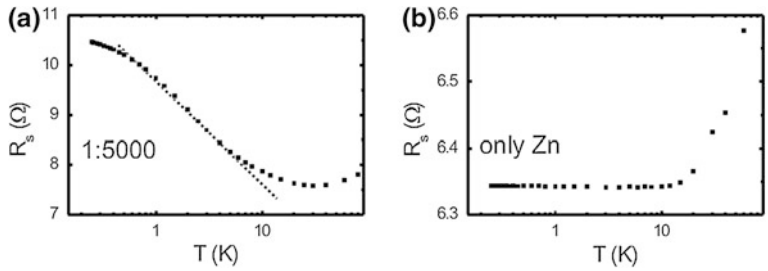

Fig. 7.8 Sheet resistance R_s versus temperature T of a 10 nm Au layer covered with a SAM of **a** Co- and Zn-complexes in the ratio 1:5000 and **b** only Zn complexes

This is another clear indication that Kondo physics is occurring in these samples, but it is still present in the presence of a large magnetic field, which is not expected for the Kondo effect. To test whether the upturn in resistance could be due to the Kondo effect, measurements in the presence of a magnetic field were also performed at 2 K and swept the field from −8 T to 8 T. Only a very small change in resistance was observed, as seen in Fig. 7.9a and b. If the resistance lowering is due to the weakening of the Kondo effect, it is much smaller than expected. There could be several explanations for these observations such as thermal energy changes, unusual magnetic properties of terpyridinyl-Co complex on surface, or different phenomena than Kondo effect.

To investigate the influence by the magnetic field in more detail, a magnetic field was applied from −1 T to 8 T at different temperatures, 0.27, 0.5, and 1 K (Fig. 7.10). For all temperatures, a drop in the resistance is seen for increasing fields. The magnetoresistance MR was defined in this sample as $MR(H) = [R_s(H) - R_s(0)]/R_s(0)$. The MR for different temperatures, including the MR at 2 K extracted from Fig. 7.9, is given in Fig. 1.10b. It is clear that the negative MR increases for decreasing temperature. This could be due to the decreasing thermal energy and might be a further explanation for the small magnetic field dependence observed at 2 K. At this point, however, we are not absolutely sure that the observed resistance increase is due to the Kondo effect, but this observation could give a further clue pointing toward this explanation. Another big problem of the measured samples is the irreproducibility of the observed results, indicating the lack of control over the self-assembly process. More experiments are needed to get a clear picture of the behavior of the observed effect.

7.3 Conclusion

In conclusion, we have developed two-dimensional organic spin systems to investigate a possible Kondo system on gold surfaces. For this purpose, terpyridinyl-Co and terpyridinyl-Zn complexes were synthesized. The formation of SAMs of metal

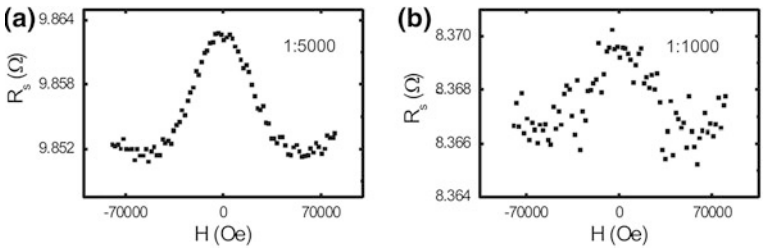

Fig. 7.9 Sheet resistance R_s versus magnetic field H for a sample with ratio **a** 1:1000 and **b** 1:5000, which showed an increase in sheet resistance when the temperature is lowered

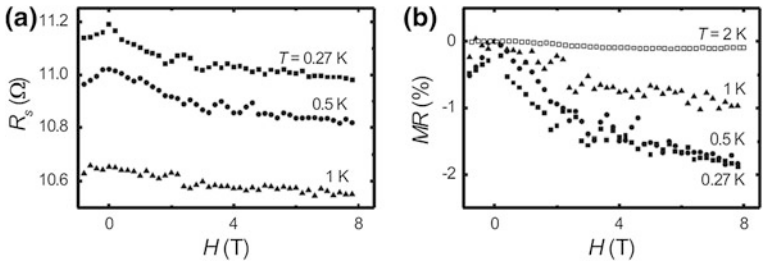

Fig. 7.10 Magnetic field dependence for the sample of Fig. 7.8 **a** Sheet resistance R_s versus magnetic field H for different temperatures, as denoted in the figure and **b** magnetoresistance $MR(H) = [R_s(H) - R_s(0)]/R_s(0)$ versus H for different temperatures, as denoted in the figure. *Symbols* correspond to the temperatures in (**a**)

complexes on gold was characterized by XPS and CV measurements. The electrical measurements showed an increase in the sheet resistance when the temperature is decreased for 10 nm Au layers, covered with a mix SAM of magnetic and non-magnetic molecules. This effect is only observed for specific ratio of the two different molecules. This effect has been reproduced in different samples and different measurement setups. Although the resistance increase is not always measured in similar prepared samples, it is never observed for samples without any magnetic ions, making it very likely to be a magnetic effect. The observed effect might indicate the presence of Kondo screening, but it is still present in the presence of a large magnetic field, which is not expected for the Kondo effect. A big problem of the measured samples is the irreproducibility of the observed results, indicating the lack of control over the self-assembly process. Hence, more efforts are needed to widely understand observed effects as mentioned in this chapter.

7.4 Experimental Section

Substrate and monolayer preparation. Si/SiO_2 ($\sim$1 nm) substrates covered with a 10 nm thick Au layer have been provided by Nanoelectronics group. The substrates were cleaned with piranha solution for 15 s (concentrated H_2SO_4 and 33 %

aqueous H_2O_2 in a 3:1 ratio; Caution: piranha should be handled carefully) and rinsed with MilliQ and EtOH. After drying in a nitrogen stream, the substrates were used immediately for monolayer formation. The monolayers were formed by simple dipping of the gold substrate in typically 1 mM of compounds in acetonitrile solution overnight at room temperature. After overnight incubation, the slides were rinsed with acetonitrile to remove any excess of compounds and subsequently dried in a nitrogen stream.

XPS. XPS was performed on a PHI Quantera SXM, using a monochromated Al K alfa X-ray source with an energy of 1486.6 eV. An X-ray beam with a diameter of 100 μm and a power of 25 W was used.

Electrochemistry. Electrochemical measurements were performed with an AUTOLAB PGSTAT10 in a custom-built three-electrode setup with bare gold substrates as the working electrode, an Ag/AgCl reference electrode, and a platinum wire as counter electrode.

Acknowledgments The work presented in this chapter was performed in collaboration with the Nanoelectronics group in the University of Twente. Professor Dr. Wilfred van der Wiel conceived the project and Dr. Wouter Naber carried out electrical measurements. Aldrik Velders and Michael de Jong are acknowledged for fruitful discussions and help. Gerard Kip is acknowledged for XPS measurements.

References

1. T. Gang, M. Deniz Yilmaz, D. Atac, S.K. Bose, E. Strambini, A.H. Velders, M.P. de Jong, J. Huskens, W.G. van der Wiel, Nat. Nanotechnol. **7**, 232–236 (2012). doi:10.1038/nnano.2012.1
2. W.J. de Haas, J.H. de Boer, G.J. van den Berg, Physica **1**, 1115–1124 (1934)
3. J. Kondo, Prog. Theor. Phys. **32**, 37–49 (1964)
4. A.C. Hewson, *The Kondo Problem to Heavy Fermions* (Cambridge University Press, Cambridge, 1997)
5. L.P. Kouwenhoven, L.I. Glazman, Phys. World **14**, 33–38 (2001)
6. D. Goldhaber-Gordon, H. Shtrikman, D. Mahalu, D. Abusch-Magder, U. Meirav, M.A. Kastner, Nature **391**, 156–159 (1998)
7. S. Sasaki, S. De Franceschi, J.M. Elzerman, W.G. van der Wiel, M. Eto, S. Tarucha, L.P. Kouwenhoven, Nature **405**, 764–767 (2000)
8. W.G. van der Wiel, S. De Franceschi, T. Fujisawa, J.M. Elzerman, S. Taruch, L.P. Kouwenhoven, Science **289**, 2105–2108 (2000)
9. I. Affleck, P. Simon, Phys. Rev. Lett. **86**, 2854–2857 (2001)
10. G. Bergmann, Phys. Rev. B **77**, 104401 (2008)
11. M. Sarachik, E. Corenzwit, L.D. longinotti, Phys. Rev. **135**, 1–3 (1964)
12. J.J. Prejean, E. Lhotel, A. Sulpice, F. Hippert, Phys. Rev. B **73**, 214205 (2006)
13. K. Yosida, Phys. Rev. **106**, 893–898 (1957)
14. M.A. Ruderman, C. Kittel, Phys. Rev. **96**, 99 (1954)
15. M. Maskus, H.D. Abruna, Langmuir **12**, 4455–4462 (1996)
16. J. Park, A.N. Pasupathy, J.I. Goldsmith, C. Chang, Y. Yaish, J.R. Petta, M. Rinkoski, J.P. Sethna, H.D. Abruna, P.L. McEuen, D.C. Ralph, Nature **417**, 722–725 (2002)
17. M. Oku, K. Hirokawa, J. Electron. Spectrosc. **8**, 475–481 (1976)

18. D.V. Gosser Jr, *Cyclic Voltammetry: Simulation and Analysis of Reaction Mechanisms* (VCH, New York, 1993)
19. W.J.M. Naber, Electron transport and spin phenomena in hybrid organic/inorganic systems, Ph.D thesis, University of Twente, 2010

About the Author

M. Deniz Yilmaz was born on 14th April 1979 in Ankara, Turkey. He obtained his Bachelor degree of Chemistry, 1st Class Honors from Ankara University, Turkey in the year 2003. He received his Master degree of Chemistry in 2006, with research project entitled "Light Harvesting and Efficient Energy Transfer in Boron Dipyrrin (BODIPY) Functionalized Perylenediimide Dyads" under the supervision of Prof. Dr. Engin U. Akkaya in Middle East Technical University. From June 2007, he was a Ph.D. candidate under the supervision of Prof. Dr. Jurriaan Huskens in the Molecular Nanofabrication (MnF) group at the University of Twente, The Netherlands, on the project of the preparation of hybrid, multilayered materials with a complex architecture. The results of this research are described in this thesis.

M. D. Yilmaz, *Orthogonal Supramolecular Interaction Motifs for Functional Monolayer Architectures*, Springer Theses, DOI: 10.1007/978-3-642-30257-2,